Confocal angle resolved linear dichroism microscopy for structural fluorescence imaging

Xiao Wang

To cite this version:

Xiao Wang. Confocal angle resolved linear dichroism microscopy for structural fluorescence imaging. Optics / Photonic. Centrale Marseille, 2013. English. NNT : . tel-00871010

HAL Id: tel-00871010
https://theses.hal.science/tel-00871010
Submitted on 8 Oct 2013

Centrale Marseille

THÈSE

pour obtenir le grade de **Docteur en Sciences**
de Centrale Marseille

Discipline : Optique, photonique et traitement d'image

Confocal angle resolved linear dichroism microscopy for structural fluorescence imaging

soutenue publiquement le **25 Septembre 2013** par

Xiao WANG

École Doctorale : Physique & Sciences de la Matière

Rapporteurs :	Prof. Markus Sauer
	Dr. Gilles Tessier
Examinateur :	Prof. Colin Sheppard, président de jury
Directeurs de thèse :	Dr. Sophie Brasselet
	Dr. Patrick Ferrand

Institut Fresnel, Aix Marseille Université, CNRS UMR 7249, Centrale Marseille

Abstract

Based on the fact that the absorption of light is a molecular-orientation sensitive process, fluorescence microscopy has been recently completed by a technique called angle-resolved linear dichroism. By analyzing the fluorescence emission response with respect to the polarization orientation of the exciting light, this technique allows retrieving orientation information of an ensemble of fluorescent molecules, namely the average orientation angle and the amplitude of the angular fluctuations around this average. In this PhD thesis, we implement new methods and instrumentation tools able to improve the robustness and speed of the polarization resolved data analysis, the rate of the data acquisition, and at last to explore the possibility to record molecular 3D orientation information. A scheme able to monitor the real-time orientation properties of fluorescent lipid probes is proposed using a high-speed spinning disk coupled to camera imaging, combined with fast switching of the polarization state by an electro optical modulator. A new data processing method is developed which considerably improves the speed and the precision of the retrieved information by investigating the sources of bias and uncertainty due to noise and instrumentation factors. The technique has been successfully tested on giant unilamellar vesicles and on living cells labeled with different fluorescent lipid probes, DiIC_{18} and di-8-ANEPPQ. It was able to acquire precise molecular orientation images at full frame rates in the range of one frame per second. At last in order to probe unambiguously the 3D orientation information of an ensemble of molecules, a new method is proposed and supported by simulations, based on the out-of-plane tuning of the excitation polarization realized in the focusing volume by coherently summing linearly and radially polarized fields.

Keywords : fluorescence, polarization, confocal microscopy, spinning disk, orientation distribution, linear dichroism

Résumé

La microscopie de fluorescence a récemment été complétée par une technique appelée dichroisme linéaire résolu angulairement, basé sur le fait que l'absorption de la lumière est un processus sensible à l'orientation moléculaire. En analysant la réponse d'émission de fluorescence en fonction de l'orientation de la polarisation de la lumière excitatrice, cette technique permet de remonter à l'information d'orientation sur un ensemble de molécules fluorescentes, plus précisément son angle d'orientation moyenne et l'amplitude de ses fluctuations angulaires autour de cette moyenne. Dans cette thèse, nous mettons en œuvre de nouvelle méthodes et instrumentations capables d'améliorer la robustesse et la rapidité de l'analyse de données de réponses résolues en polarisation, la vitesse de l'acquisition de données, et d'explorer la possibilité de mesurer l'orientation 3D de molécules. Nous proposons une méthode capable de mesurer les propriétés d'orientation de sondes lipidiques fluorescentes par l'utilisation d'un disque de Nipkow couplé à une imagerie par caméra, et combiné avec la modulation rapide de la polarisation par modulateur électro-optique. Une nouvelle méthode de traitement de données est développée pour considérablement améliorer la rapidité et la précision de l'information par une étude des sources de bruit et d'incertitude, dues au bruit et aux facteurs instrumentaux. Cette technique a été testée avec succés sur des vésicules géantes uni-lamellaires et sur cellules vivantes, marquées par les sondes lipidiques DiIC$_{18}$ et di-8-ANEPPQ. Cette méthode est capable d'acquérir une information précise sur l'orientation moléculaire à une cadence d'une image par seconde. Enfin, afin de sonder de manière non ambiguë l'orientation 3D d'un ensemble de molécules, une nouvelle méthode est proposée, supportée par des simulations numériques, basée sur la variation hors plan de la polarisation d'excitation dans le volume focal par une somme cohérente de champs polarisés linéairement et radialement.

Mots clefs : fluorescence, polarisation, microscopie confocale, disque de Nipkow, distribution d'orientation, dichroisme linéaire

Acknowledgements

The work would not have been possible without the help of many people, it is my pleasure to thank them.
To the members of the jury: Prof. Markus Sauer, Prof. Colin Sheppard, Dr. Gilles Tessier for their interest in this thesis, the careful reading of the manuscript, having made the journey to Marseille and helpful suggestions.

A special acknowledgement to my supervisor Prof. Sophie Brasselet for warm welcome on my study in MOSAIC group and her excellent supervision of this project. Through out this project, she always offered her patience to explain optics and biological problem, encouraged me for our results and inspired me to do open-mind thinking. Moreover, she exhibited her enthusiasm, intuition and efforts to science, which definitely will influence me in my research career.

With my special appreciation too, to my co-superviser Dr. Patrick Ferrand for his intelligence and patience. He is a genius in setup implementation and programming. During these three years, he gave me a lot of inspiring ideas for setup building and endless helps in detail for Matlab, LabVIEW programming and this project. I am very happy to have been working with him.
To Prof. Hervé Rigneault for his great support and helps to my study in the MOSAIC group.
To my good partner Alla Kress for her hard works in biology, she made a lot of measurements in biological samples, which makes this technique useful.
To my good partner Wei He for her implementation test of 3D polarization control setup.
To Julien Savatier for his helps in biological problems.
To Julien Duboisset for cooperations and discussion on applications of amyloid fibrils.
To Cyril Favard for sharing his knowledge of Giant unilamellar vesicles .
To Cesar and Fatma-Zohra for their friendly helps to this work and my life, we have spent a lot of nice moments during these three years.
To Pascal, Xueqin Chen, Haitham, Sara, Sherazade, Deep, Satish, and all other members of the MOSAIC group for making the nice office atmosphere.
At last, I would like to thank my wife for her family supports during these three years.

Contents

Introduction i

1 Fluorescence is an orientation sensitive process 1
- 1.1 One-photon fluorescence . . . 1
  - 1.1.1 Absorption and emission spectra properties . . . 2
  - 1.1.2 Life time . . . 4
  - 1.1.3 Absorption and emission transition dipoles . . . 4
- 1.2 Fluorescence anisotropy . . . 7
  - 1.2.1 Fluorescence anisotropy in solution . . . 7
  - 1.2.2 Fluorescence anisotropy in ordered samples . . . 10
- 1.3 Linear Dichroism . . . 13
- 1.4 Angle resolved linear dichroism . . . 14
- 1.5 Conclusion . . . 16

2 Angle-resolved Linear dichroism (ARLD) 17
- 2.1 Fluorescence emitted by an ensemble of dipoles . . . 17
  - 2.1.1 Microscopic and macroscopic frame . . . 18
  - 2.1.2 Distribution function . . . 20
  - 2.1.3 Emitted fluorescence . . . 21
- 2.2 Setup . . . 22
  - 2.2.1 Optical setup . . . 22
  - 2.2.2 Polarization distortions . . . 24
- 2.3 Data processing . . . 26
  - 2.3.1 Retrieval of the distribution parameters . . . 26
  - 2.3.2 Precision analysis . . . 30
  - 2.3.3 Sources of bias and error criteria . . . 30

2.4 Example of measurements . . . 33
2.4.1 Giant unilamellar vesicles labeled by DiIC$_{18}$ . . . 33
2.4.2 Giant unilamellar vesicles labeled by di-8-ANEPPQ . . . 34
2.4.3 An application in Cos-7 Cells . . . 34
2.5 The limitations . . . 35
2.5.1 Out-of-plane orientation η . . . 35
2.5.2 Measurement speed . . . 36
2.6 Conclusion . . . 37

3 High frame rate confocal ARLD 43
3.1 Experiment setup . . . 44
3.1.1 Parallel confocal imaging . . . 44
3.1.2 Optical setup . . . 47
3.1.3 Polarization control . . . 48
3.1.4 Hardware . . . 50
3.2 Calibrations . . . 51
3.2.1 Polarization Calibration . . . 51
3.2.2 Camera calibration . . . 54
3.2.3 Data processing . . . 56
3.2.4 Precision analysis . . . 58
3.3 Examples of measurements . . . 59
3.3.1 Giant unilamellar vesicles labeled with DiIC$_{18}$ . . . 59
3.3.2 Cos-7 cells . . . 63
3.4 Acquisition rate . . . 65
3.5 Conclusion . . . 65

4 Determining 3D orientation distribution 67
4.1 Measuring of 3D orientation: the case of a single dipole . . . 67
4.2 3D excitation and detection for a distribution of dipoles . . . 72
4.2.1 About the need of a full calculation . . . 72
4.2.2 The electric field in the focus volume of a high NA objective . . . 74
4.2.3 Emission field by an excited dipole . . . 79
4.2.4 Image of a dipole and detection efficiency . . . 82
4.3 Proposed method to probe the order in 3D . . . 87
4.3.1 Scanning scheme of the polarization of the exciting field . . . 87

4.3.2 Unambiguous retrieval of (η, ψ) 90
4.3.3 The membrane geometry 93
4.3.4 Practical setup 96
4.4 Conclusion 97

Conclusion and outlooks 98

A The effect of Homo-FRET on polarization resolved measurements 101
A.1 Modeling the fluorescence response of molecule in a cone with Homo-FRET 102
A.1.1 Definition of the coupled dipoles 102
A.1.2 Absorption probability of the donor 104
A.1.3 Detection probability of the acceptor 104
A.1.4 Coupling factor 105
A.1.5 The emitted fluorescence 105
A.2 Results 106
A.2.1 Cones distributed in the whole focal volume 106
A.2.2 Analysis for cones models distributed in membranes 108
A.3 Brief analysis for FRET 110

B Measurement of a polarization state and analysis of polarization distortions 113
B.1 Measurement of a polarization state 113
B.1.1 Characterization of a polarization state 113
B.1.2 The quarter waveplate method 113
B.1.3 Parameters retrieval 116
B.2 Analysis of polarization distortions induced by an optical path 117

C Preparation of samples 119
C.1 Preparation of Giant Unilamellar Vesicles (GUVs) 119
C.2 Preparation of cells 119

Bibliography 121

Introduction

Molecular structural organization is a crucial factor in biological processes where functions can be closely related to the orientation distribution of molecules. For instance, in cell biology the structural organization of proteins and lipids are the direct signature of molecular interaction mechanisms which play a determining role in biological functions such as cell shape maintenance and motility [1], vesicular trafficking [2], and signaling [3]. Polarization as one of the property of light has been exploited for studying the orientation related information of molecules. In 1920, F. Weigert firstly discovered that the fluorescence from solutions of dyes is polarized [4]. Based on this property, a method called fluorescence anisotropy was proposed by comparing the fluorescence signals recorded along analysis directions parallel and perpendicular to the incident polarization. Because of the sensitivity to depolarization process, it has been primarily used for decades in studies of solution in order to address issues such as rotational diffusion and energy transfer between neighbor molecules. Later, this technique has been introduced to investigate the organization of biomolecular assemblies in ordered media such as lipid membranes [5, 6]. Another technique, called linear dichroism (LD) was also proposed based on the fact that the absorption probability is determined by the relative orientation between the absorbing dipole and exciting electric field. This method is now widely used to retrieve molecules orientation information, by comparing the fluorescence response recorded for two orthogonal directions of polarization of excitation. Compared to fluorescence anisotropy, the LD is not affected by depolarization processes such as fast rotational diffusion or energy transfer [7, 8]. During the past ten years, an increasing number of research groups have dedicated their studies to LD techniques to explore biological samples such as amyloids [8, 9], septins [6], membranes [7], actin [10].

In ordered assemblies however, which can be characterized by a more complex set of parameters, these two methods that utilize two orthogonal directions of measurements, suffer from some limitations. Indeed the ratio between two measurements supplies only one parameter, which is not sufficient to characterize the orientational distribution of an ensemble of molecules in the observation volume. Moreover, these two methods impose preferential directions of excitation and/or detection, which are not necessarily adapted to the investigated distributions. In order to circumvent these limitations, our group has introduced a more refined mode of operation of LD, which is named angle-resolved linear dichroism, implemented it in confocal microscopy using several excitation polarization angles. This technique, first implemented for two-photon fluorescence [11], has been exploited for one-photon fluorescence for the study of the orientational order of lipid probes and membrane proteins [12, 13]. At this stage the technique was limited to time scales of few minutes and to molecules oriented in the sample plane.

In this thesis, we propose to push this method to its limits so that it can address efficiently issues of cell biology and structural imaging in tissues. The optimization will be made on three main issues:

- Providing a powerful data analyzing procedure, in order to obtain a comprehensive picture of the measured molecular order in a fast and robust way. This includes the improvement on the data analysis (previously relying on time-consuming fitting procedure), the inclusion of sources of bias (polarization distortions) and the quantification of the precision of the method.

- Improving data acquisition speed by a parallel confocal configuration to monitor the molecular order in dynamic samples with time scales below seconds.

- Exploring new excitation strategies in order to address out-of-plane dipoles orientation, and potentially reach a full 3D orientational characterization.

This manuscript is organized as follows:

Chapter 1 reviews briefly the one-photon fluorescence process and involved important properties, including polarization sensitivity in the absorption and emission processes. Several techniques using the polarization property of light are analyzed with detailed principle, advantages, limitations and applications.

In Chapter 2, we detail the experimental setup, and propose an efficient method for data processing. The precision of this setup is analyzed. Some examples of validation measurements in artificial lipid membrane and applications in the structural analysis of cell membranes are given.

Chapter 3 describes a new parallel confocal scheme dedicated to faster data acquisition. Measurements of lipid order are compared with that measured in the previous setup.

In Chapter 4, the proposed method to probe 3D order information is detailed, and numerical simulations are presented. An experimental setup is proposed.

Chapter 1

Fluorescence is an orientation sensitive process

1.1 One-photon fluorescence

Fluorescence is the emission of light by a substance that has absorbed light at a different wavelength. One of the early experiments showing fluorescence was reported by Sir J.F.W. Herschel in 1845 [14]. When the sunlight illuminated a solution of quinine in water, at some special angle with respect to the direction of sunlight, a blue light emission could be observed. In 1852, Sir G.G. Stokes published his work about the emission of light from the same solution of quinine [15]. Based on this historical experiments as presented in Fig. 1.1, he reported that the emitted light exhibits a longer wavelength than the exciting light. In his experiment, the exciting light below 400 nm (blue light) is absorbed by the quinine solution, and the emitted light is shifted to a longer wavelength (450 nm) that can be observed by eyes after passing a yellow filter (wine glass) which blocks the incident exciting light.

This photophysical process was later explained well by A. Jablonski in 1935 [18]. In the so-called "Jablonski diagram", the fluorophore or fluorescent dye lies on the ground state S_0. When this molecule absorbs light, the energy possessed by a photon is transferred to the molecule and the molecule is transferred into a higher electronic excited state S_1. Finally after several decay events, the molecule returns to its ground state S_0 with the emission of a photon. This process involves several important parameters with characteristic absorption and emission spectra, life time and absorption and emission transition

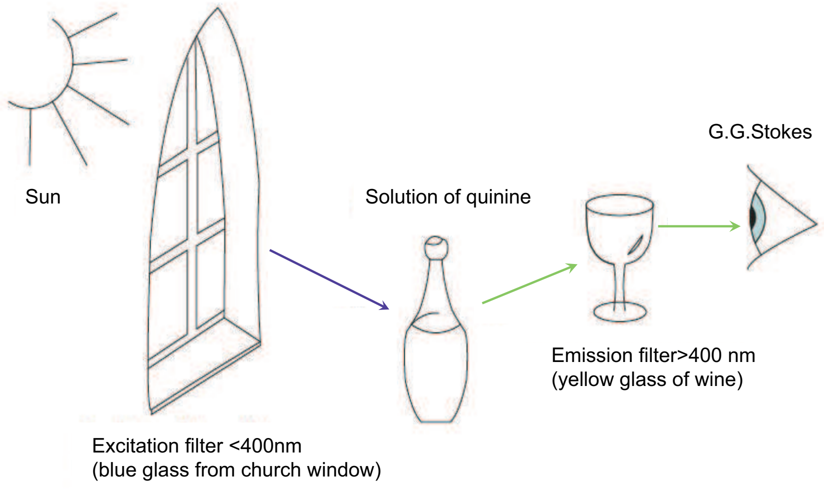

Figure 1.1: Experimental set-up used by G.G. Stokes from [16].

dipoles, which are widely explored and used in a large range of applications.

1.1.1 Absorption and emission spectra properties

When the molecule absorbs light, all the energy possessed by a photon is transferred to the molecule (the energy of photon is inversely related to the photon's wavelength $E = h \times c/\lambda$, where h is Plank's constant and c and λ are the speed and wavelength of light in vacuum, respectively) [19]. The minimum energy required for absorption is the amount that can cause the transition of an electron from ground state S_0 into the lowest excited state (that is S_0 to S_1), which corresponds to the longest wavelength defined as the cut-off-wavelength. If the wavelength is shorter than the cut-off wavelength, the molecule will reach vibration or rotation states of level S_1, or a transition into an even higher excited state S_2. Therefore there is a range of wavelengths that could be absorbed to excite a molecule, forming the absorption spectrum (Fig. 1.2(a)). The time needed for a transition from the ground state to an excited state is extremely short, on the order of femtoseconds [20, 21].

The molecule that is transferred into higher energy levels (for example S_2) then undergoes internal conversion and vibrational relaxation (Fig. 1.2(b)). During internal conversion, the electron transits from the lowest vibrational level of S_2 to an excited vibrational level of S_1. A vibrational relaxation occurs then, the electron coming down to the lowest

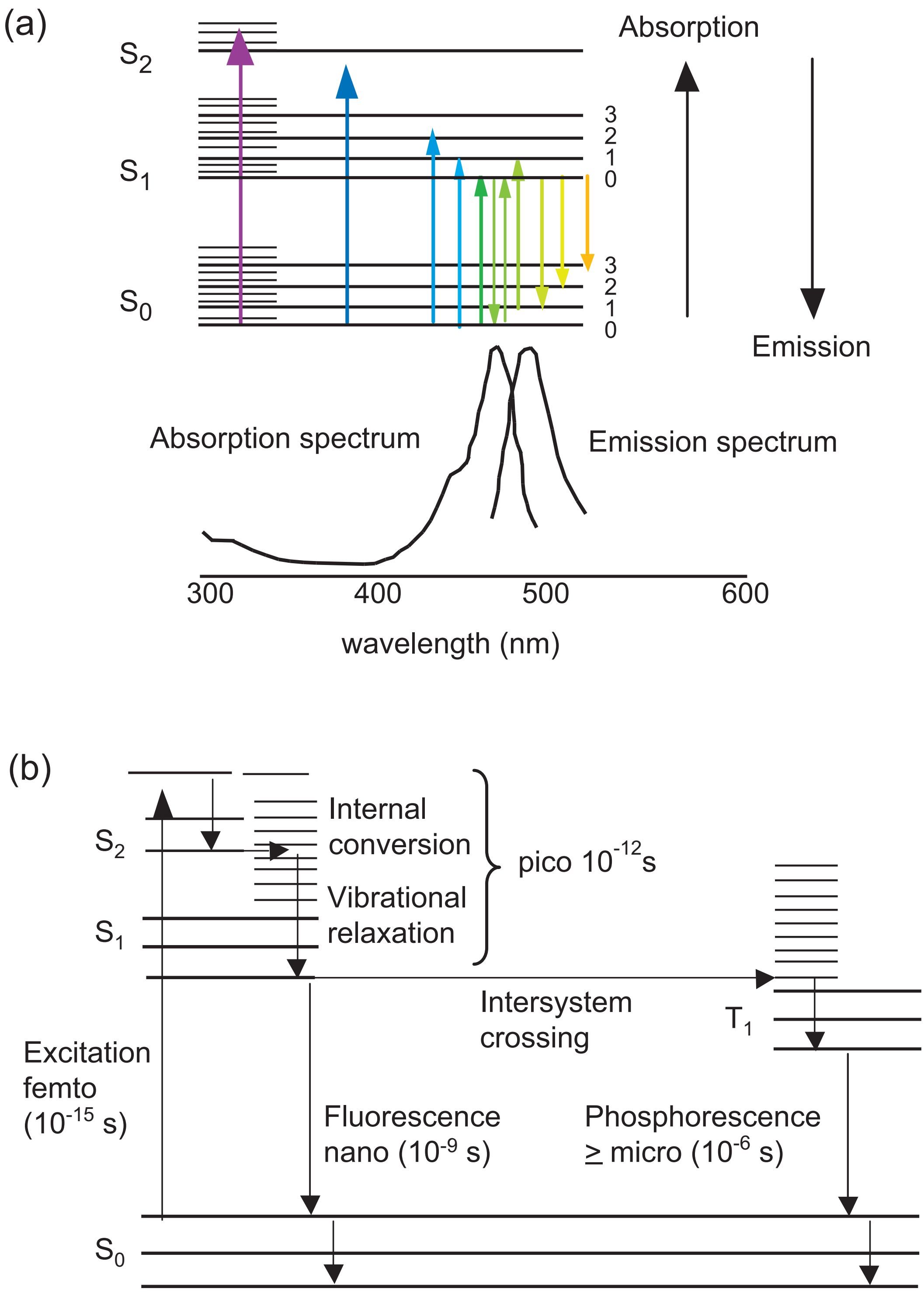

Figure 1.2: (a) The resulting absorption and emission spectra due to transitions between different electronic (S_0, S_1 and S_2) and vibrational states. (b) Involved energy states of a fluorescence process with their average lifetimes: S_0, S_1 and S_2 are the electronic states and T_1 is the triplet state. Adapted from [17].

vibrational level of S_1. Finally, the emission of the photon brings the molecule to its ground electronic state S_0. In the most common organic fluorophores, internal conversion and vibrational relaxation occurs within the range of picoseconds, and the emission process occurs after few nanoseconds.

The energy loss caused by vibrational relaxation causes that the emission spectrum shifts to higher wavelengths, which is called the Stockes shift. But not all fluorescent emission events occur at longer wavelength than the exciting light, there is also some degree of spectra overlap. That is explained by the fact that a fraction of molecules is in the excited vibrational state of S_0 and could be transited to the excited state S_1 with a smaller energy than the emission energy. Thanks to the Stoke's shift, the excitation and emission light can easily be separated by an emission filter, which makes the fluorescence technique very powerful to visualize or measure molecule without any background from the incident light.

1.1.2 Life time

In fluorescence there is one additional important parameter: the fluorescence lifetime τ which defines the average time the fluorophore spends in the excited state. The emission is indeed a random process taking place within the order of nanoseconds for usual organic fluorophores. Not all the molecules initially excited by absorption return to the ground state S_0 by fluorescence emission, a fraction of them in the excited state come down to the ground state S_0 following non-radiative relaxation processes (i.e. energy transfer, collisional quenching or intersystem crossing). Therefore, the lifetime τ is determined by both the radiative and the non-radiative processes [19]:

$$\tau = \frac{1}{k_r + k_{nr}} \tag{1.1}$$

where k_r and k_{nr} are respectively the radiative and non-radiative decay rates. The fluorescence life time is an important quantity to consider when measuring rotational properties of molecules such as in fluorescence anisotropy as described in Section 1.2.

1.1.3 Absorption and emission transition dipoles

The processes of a single photon absorption and emission are characterized by a transition dipole moment (TDM) [19]. The TDM is a vector created by the overlap between the fluorophore molecular orbitals in the ground and excited states, and the dipole vector $\vec{\mu}$. It is easily understood by considering that for a fluorophore the TDM describes the direction in which the electrons shift within the molecule during excitation through absorption of a photon (or during emission of a photon of fluorescence). The TDM is an intrinsic property of a fluorophore. Therefore, the fluorophore could be considered as a fluorescence dipole when it interacts with light (absorption) and emits light (emission), denoted by $\vec{\mu}_{abs}$ and $\vec{\mu}_{em}$.

As detailed in [22, 10] with quantum mechanics perturbation theory, the probability P_{abs} of one-photon absorption by a molecule is proportional to the square of the product between the exciting field $\vec{E}$ and absorption transition dipole $\vec{\mu}_{abs}$:

$$P_{abs} \propto |\vec{E} \cdot \vec{\mu}_{abs}|^2 \tag{1.2}$$

According to this expression, the absorption probability is sensitive to the polarization state of the excitation light. The polar plot illustrated in Fig. 1.3 represents the dependence of the absorption probability P_{abs} as a function of the angle δ between $\vec{E}$ and $\vec{\mu}_{abs}$. When the polarization of the exciting field is parallel to the dipole orientation, the absorption gets maximum. On the contrary the light can not be absorbed with a polarization perpendicular to the dipole orientation.

In the emission process, the fluorophore is also considered as an emission transition dipole $\vec{\mu}_{em}$, the radiation field in the far field is expressed as [23]:

$$\vec{E}_{em} \propto \vec{K} \times (\vec{K} \times \vec{\mu}_{em}) \tag{1.3}$$

where $\vec{K}$ indicates the propagation direction. According to the eq. 1.3, the emitted intensity $|\vec{E}_{em}|^2$ is proportional to $\sin^2 \zeta$, where ζ is the angle between the emission dipole and the propagation direction $\vec{K}$. The emission pattern exhibits a cylindrical symmetry around the dipole $\vec{\mu}_{em}$. Fig. 1.4 presents the emission intensity pattern in a section plane containing the dipole. For a given direction, the emission field is linearly polarized and the polarization angle is governed by the directions of the observation and the emission dipole.

In fluorescence microscopy, the emission field from a fluorescence dipole is collected by an objective and from Fig. 1.4 it can be easily understood that its emission polarization will be changed depending on the collection aperture (see Appendix A.1.3). In particular for a dipole positioned at the focusing center and oriented in the XY plane perpendicular to optical axis, the emission field on the back aperture of an objective is nearly linearly polarized across the beam, keeping the same orientation as the dipole. If the dipole lies

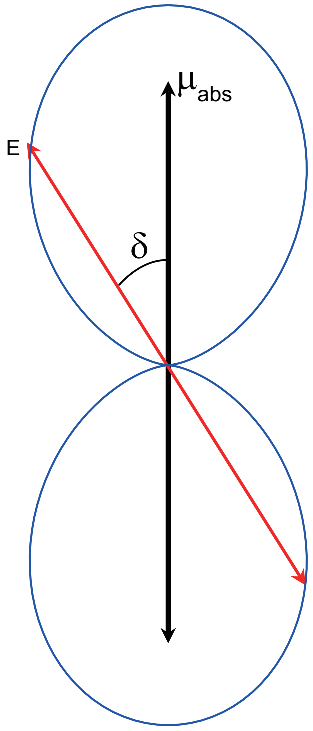

Figure 1.3: Dependence of absorption probability on the angle δ between the dipole and electric field of the exciting light.

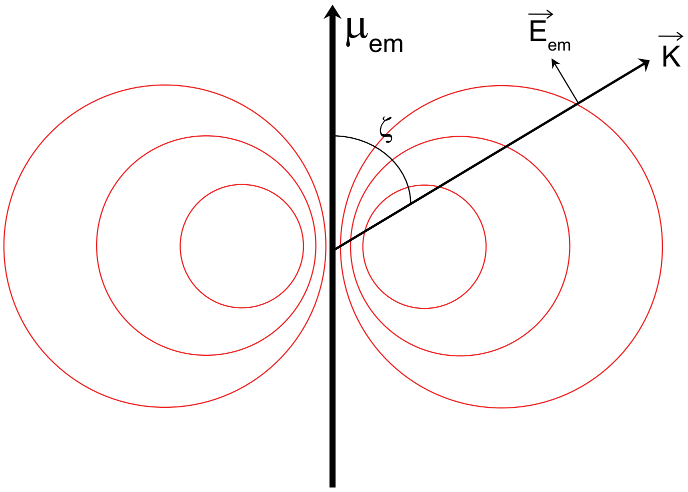

Figure 1.4: The emission intensity pattern of a fluorescence dipole.

along the optical axis of the objective, the polarization direction across the back aperture is radially distributed see Section 4.1. With respect to the analysis direction of the light polarization, the global emission efficiency in fluorescence is defined by a detection probability P_{em}. Along an analyzing direction i, P_{em} is calculated as:

$$P_{em} = |\vec{E}_{em} \cdot \vec{u}_i|^2 \tag{1.4}$$

where $\vec{u}_i$ is a normalized vector along direction i.

Finally the absorption efficiency is sensitive to the polarization of the exciting light and the emitting light is polarized according to the direction of its emitting dipole. The polarization as an important property of light is widely used in fluorescence detection technique. These techniques are summarized into two main classes. First, the fluorescence anisotropy method is based on analyzing the polarized emitted fluorescence light under a given polarization for excitation see Section 1.2. A second class of techniques exploits the change of absorption efficiency for different polarization conditions, namely the linear dichroism (LD), see Section 1.3.

1.2 Fluorescence anisotropy

1.2.1 Fluorescence anisotropy in solution

Fluorescence anisotropy is a widely-used technique that was first developed to study molecules in solution (and more generally extended to isotropic biological samples) [24]. For a solution excited by an linear polarized light, and emitting light is detected respectively in perpendicular and parallel direction with respect to the polarization orientation of the exciting light. A conventional scheme is illustrated in Fig. 1.5. The vertical polarized light (along Z direction) excites a cuvette containing a fluorescent solution. The measured emitting light along Y and Z polarization direction are called $I_\perp$ and $I_\parallel$. The fluorescence anisotropy a is calculated as:

$$a = \frac{I_\parallel - I_\perp}{I_T} \tag{1.5}$$

where, $I_T = I_X + I_Y + I_Z$ is the total intensity. Because the component polarized in the X and Y directions have the same intensity $I_\perp$, only the intensities polarized along Y and

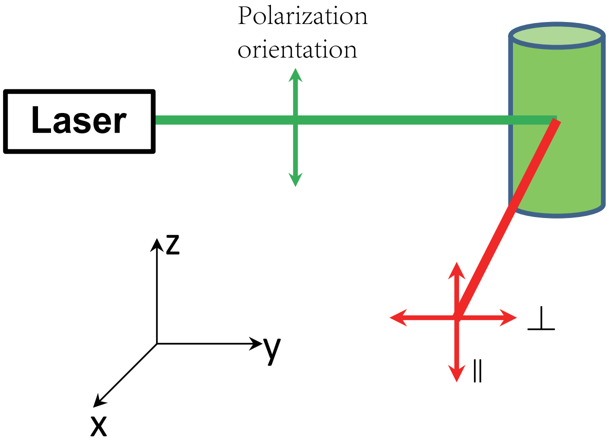

Figure 1.5: Conventional experimental scheme for measuring fluorescence anisotropy in solution. Green arrow indicates the polarization of exciting light and red arrows indicate the emission polarization orientation.

Z directions is recorded in the given geometry. So the anisotropy a can be expressed as:

$$a = \frac{I_{\parallel} - I_{\perp}}{I_{\parallel} + 2I_{\perp}} \tag{1.6}$$

This ratiometric method makes this technique insensitive to fluctuations of the incident intensity. In this expression, $I_{\perp}$ and $I_{\parallel}$ are calculated by summing up the corresponding emitting light from each single dipoles, following eqs. 1.2 and 1.4.

In a first case, it is assumed that the absorption transition dipoles μ_{abs} and the emission transition dipoles μ_{em} are parallel to each other, and we suppose that the molecules rotate so slowly that after excitation the photon is emitted before the molecule rotates (for example in a viscous solution). After calculation, the anisotropy is equal to 0.4 for this basic case in an isotropic sample [25].

The anisotropy above is calculated with assumption of the same orientation for absorption transition dipole μ_{abs} and emission transition dipole μ_{em}. Different orientations between μ_{abs} and μ_{em} (which is generally the case when the molecule the molecule conformation differs from the ground to the excited state) will induce depolarization, which decreases the anisotropy. For an orientation difference β, the corresponding anisotropy is expressed as [25]

$$a_0 = \frac{2}{5}\left(\frac{3\cos^2\beta - 1}{2}\right) \tag{1.7}$$

The fundamental anisotropy a_0 is calculated without any other depolarization processes such as rotational diffusion and energy transfer. Under this assumption, the orientation deviation β can be retrieved from the fundamental anisotropy a_0. $a_0 = 0$ corresponds $\beta = 54.7°$, and when β exceeds 54.7° the anisotropy reaches a negative value.

The measurement of the angle β presented above is one of the possible applications that utilize the anisotropy method. Moreover, due to the sensitivity of anisotropy to depolarization, anisotropy measurements are widely used in a range of applications that involve depolarization processes, in particular rotational diffusion which will be detailed here.

When the fluorescence life time τ is longer than the molecular rotational correlation time ϑ, the excited molecule rotates to another orientation before it emits its photon. Therefore, the emission dipole μ_{em} deviates from the orientation of the absorption dipole μ_{abs}, and depolarization occurs in a similar way as for the angle β. Reversely if the life time τ is shorter than the rotational correlation time ϑ, emission happens before the dipole rotates. The emission dipole μ_{em} then stays parallel to the absorption dipole μ_{abs} (or related to it by a fixed angle β). In view of this, the anisotropy method is an interesting tool to investigate the relationship between ϑ and τ, which is expressed in the Perrin equation [25]:

$$\frac{1}{a} = \frac{1}{a_0}(1 + \frac{\tau}{\vartheta}) \tag{1.8}$$

where a_0 is the fundamental anisotropy and a is the measured anisotropy in a non-rigid medium. The rotational correlation time ϑ of a fluorophore is given by:

$$\vartheta = \frac{\eta V}{RT} \tag{1.9}$$

where η is the viscosity of the solvent, V is the hydrodynamic volume of the rotating fluorophore, R is the gas constant and T is the temperature.

When the rotational correlation time is much longer than the life time ($\vartheta \gg \tau$), as discussed above, no depolarization occurs then the measured anisotropy a equals to the fundamental anisotropy a_0. If $\vartheta \ll \tau$, the emission light is completely depolarized then the measured anisotropy is zero. Therefore for a given fluorescence molecule, the life time can be retrieved from anisotropy with a known rotational correlation time. Reversely, with known lifetime, anisotropy can reveal the rotational correlation time which depends on many factors like the viscosity of the solvent, the size and the shape of fluorophores as presented in eq. 1.9. Therefore, this technique is widely used in a range of researches studying the denaturation of proteins (which induces conformational changes leading to modifications of the rotational behavior) or their association with other macromolecules [19].

Fluorescence resonance energy transfer (coming from a Förster energy transfer) (FRET) [26] as one of depolarization process definitely affects the polarization detection. Indeed this FRET occurs when molecules are close to each other (at distances less than 10nm), inducing non-radiative transfer between an absorption dipole and an emission dipole which orientation is decorrelated from the acceptor. This effect is detailed in Appendix A

1.2.2 Fluorescence anisotropy in ordered samples

Besides applications in solutions presented above, anisotropy is also used to probe the orientation of biomolecular assemblies [5, 6, 10, 9]. To characterize the orientation information of an ensemble of molecules, obviously a single orientation parameter is not enough. For this reason, a geometrical model is introduced to describe the angular distribution function experienced by the excited molecules. In order to take into account the angular freedom, the simplest model is a cone shape used to describe the average orientation ρ of the distribution and the width of the orientation distribution ψ, which is illustrated in Fig. 1.6(a). This model has been largely used to model lipid probes in cell membranes [5, 27].

In this cone model, the orientation of the molecules is defined by a set of (θ, ϕ) angles in the local frame where the z axis is the mean orientation ρ of the cone. As presented in Fig. 1.6(b), θ denotes the tilt angle respect to z axis and ϕ is the azimuthal angle in the (x,y) plane. Considering the cone model and its cylindrical symmetry, the orientation distribution function can be calculated by as:

$$f(\theta,\phi) = \begin{cases} \frac{1}{\int_0^{\psi/2} \mathrm{d}\theta \int_0^{2\pi} \sin\theta \mathrm{d}\phi} = \frac{1}{4\pi \sin^2(\psi/4)} & \text{if } \theta \leq \psi/2 \\ 0 & \text{else} \end{cases}$$

where $f(\theta,\phi)$ denotes the probability to find a molecule in the excited volume, processing the orientation (θ,ϕ), and the ψ is the full width of orientation distribution. Fig. 1.6(c) presents the cone model distribution, within which the orientation of the molecules is distributed homogeneously and ends up with a sharp edge.

To access to information about the cone formed by an ensemble of molecules, it is necessary to retrieve polarized fluorescence signals.

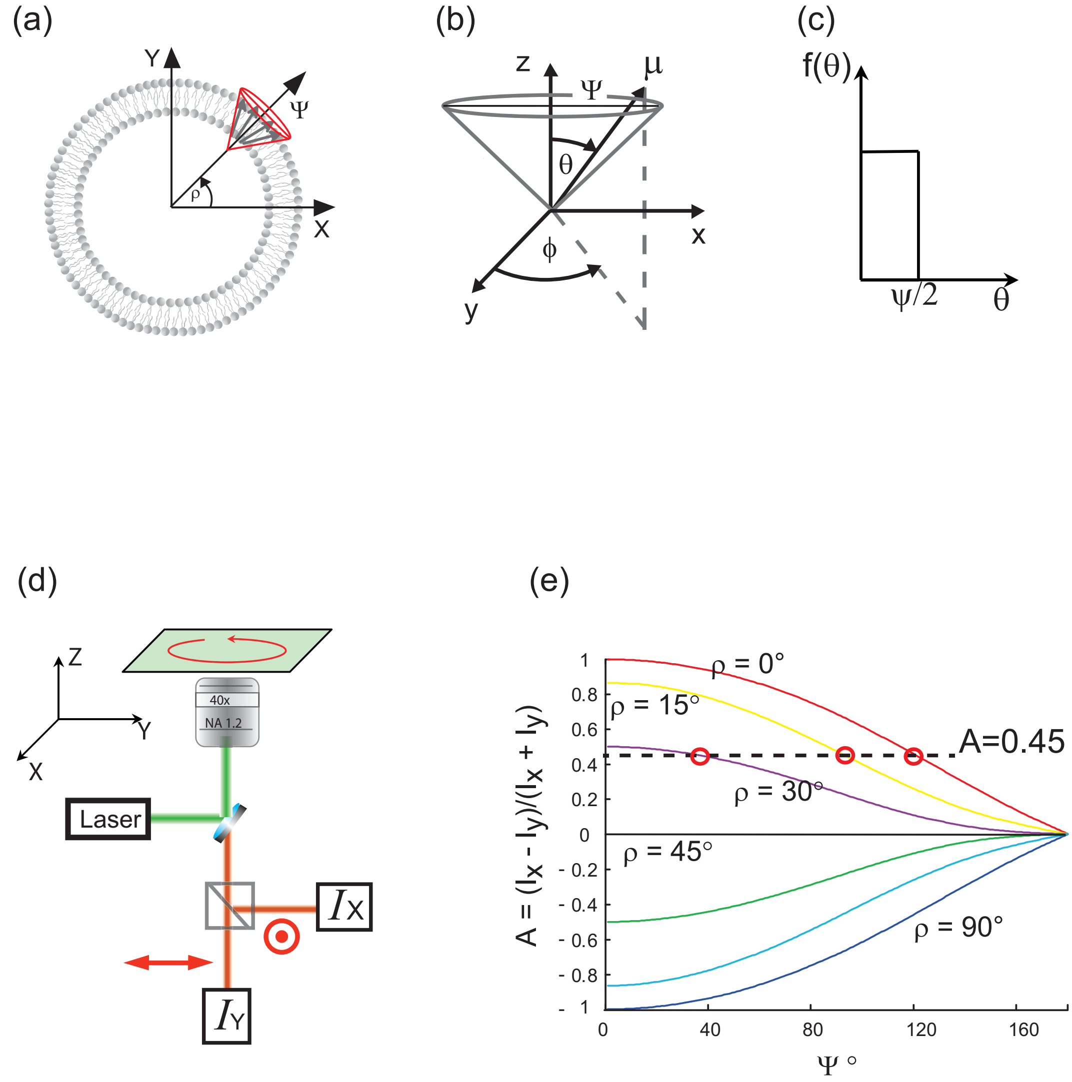

Figure 1.6: (a) Characterizing an ensemble of molecules in the focus volume as a cone, with mean orientation ρ and distribution width ψ. (b) Representation of the absorption/emission transition dipole moment $\vec{\mu}_{abs}/\vec{\mu}_{em}$ (denoted as a single vector $\vec{\mu}$) within a cone-shaped orientational distribution in spherical coordinates. θ indicates the tilt angle of $\vec{\mu}$ with respect to the mean orientation z axis and ϕ is the azimuthal angle with respect to x axis. (c) Two dimensional representation of a cone model. Due to cylindrical symmetry of the orientation distribution the ϕ dependence is omitted. (d) Conventional experiment setup for measuring anisotropy of an ensemble of molecules. The exciting light at the sample plane is a circular polarized light, and the emission is measured along two orthogonal polarization detections X and Y. (e) The calculated anisotropy A for cone model with different mean orientation ρ and ψ. The black dashed line denotes the $A = 0.45$ value as an example, and three red circles indicate three possible sets of (ρ, ψ) values leading to $A = 0.45$.

The anisotropy method usually implemented in microscopy is based on an illumination by a circular polarized light, as presented in Fig. 1.6(d), and the emission light is detected along two orthogonal polarized directions: I_X and I_Y. Due to the excitation with circular polarized light, there is no privileged photoselection direction and thus the anisotropy is expressed as :

$$A = \frac{I_X - I_Y}{I_X + I_Y} \tag{1.10}$$

where the total intensity considers here only in-plane response.

In a highly ordered sample (i.e. $\psi = 0$) without depolarization, the anisotropy A would be 1 when the molecules lie along the X direction and -1 when the molecules lie along the Y direction. When the molecules distribute within a cone or the emission process is affected by a depolarization process, the anisotropy A gets an intermediate value between 1 and -1. For a given cone with fixed ρ and ψ, the anisotropy value is unique. However, for a measured A there are several solutions of sets of (ρ, ψ). That is because only one quantity measurement (A) can not allow the retrieval of two unknown parameters. For instance, Fig. 1.6(e) presents the calculated anisotropy values for cones with various sets of (ρ, ψ): a given anisotropy $A = 0.45$ corresponds to several probable solutions of (ρ, ψ) as illustrated with small red circles. This really illustrates the limitations of this method. For this reason this technique is usually applied to samples with a priori known mean orientation, such as in red blood cells [5], giant unilamellar vesicles [27] and cell blebs [28], which possess a round-shape geometry along which the molecules orient in the radial distribution [9, 10].

Moreover, this anisotropy method loses its power at a special angle ($\rho = 45°$) where the ratio between I_X and I_Y is independent on the cone aperture ψ due to the symmetry. As presented in Fig. 1.6(e), with $\rho = 45°$ the calculated anisotropy A is equal to zero for an arbitrary ψ, which is illustrated by a flat line.

At last anisotropy is based on the analysis of the polarization response of the emission light, that can easily be affected by depolarization process, such as fast moleculear rotation and energy transfer as discussed in Section. 1.2.1. Therefore this method requires appropriate selection of dyes (shorter life time than rotational diffusion time is better) and preparation of molecular concentration (low concentration prevents from energy transfer between molecules).

1.3 Linear Dichroism

In the section above, we have presented that orientation information of an ensemble of molecules can be probed by anisotropy, which however suffers from several limitations, in particular can be affected by the depolarization. To overcome the limitations of anisotropy, another method has been invented to probe the orientation information of fluorescence dipoles based on the absorption sensitivity to the polarization of the exciting light, which is called linear dichroism (LD). As presented in eq. 1.2, for one-photon fluorescence process, the rate of light absorbed by a molecule is proportional to the squared cosine of the angle between the electric field of the excitation beam and the transition dipole moment.

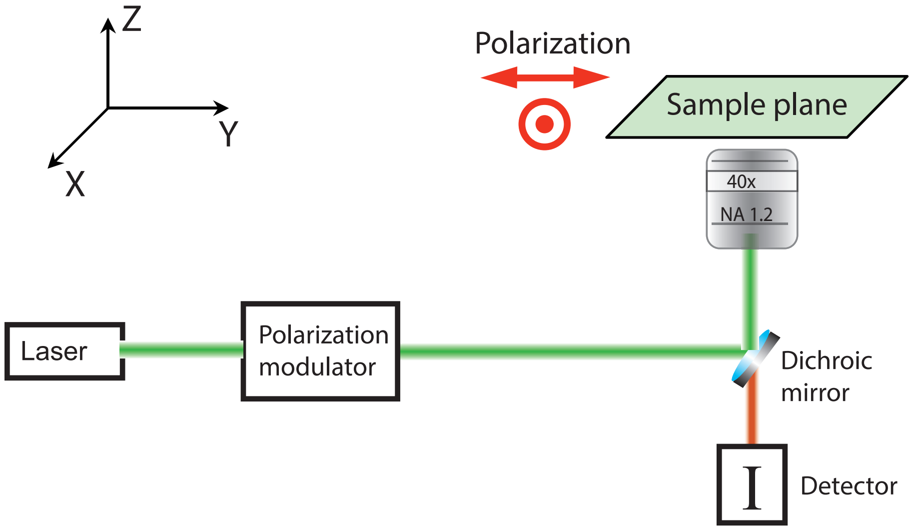

Figure 1.7: The conventional linear dichroism measurement setup. The sample is sequentially excited by two orthogonal polarization light and emission light is recorded by a detector without polarization analyzer.

Fig. 1.7 presents a scheme of this method. In order to create two orthogonal polarization orientations in the sample plane, the polarization of the excitation light is set by a polarization modulator such as by rotation of half waveplate or by a tunable waveplate combined with a quarter wave plate. The emission light is recorded by only one detector without polarization separation in the collection path, which makes this method weakly affected by depolarization processes [7, 8] (see Appendix A). Therefore this method has been widely used to probe the orientation behavior of molecules in complex media where the local geometry of the biomolecular assemblies is not a priori known. It has permitted to address address a vast variety of issues in in structural imaging of cell membranes, among them : the effect of cholesterol depletion on the local lipid order [7], orientational distributions of lipid in model membranes [29], and conformational changes of receptor proteins [30].

LD involves a comparison of the fluorescence response recorded for two orthogonal directions of the polarization of the excitation light. There is no fixed definition and expression of LD and the data processing methods are selected to suit the analysis of the samples. One of the common definition for LD is the ratio of the fluorescence intensity between two different polarization orientation of the exciting light [30], which is expressed as:

$$r = \frac{I_h}{I_v} \tag{1.11}$$

where I_h and I_v are the fluorescence intensity respectively recorded for horizontal and vertical polarization directions of the exciting light. However other definitions exist that use similar approaches as for anisotropy [7].

Linear dichroism is based on two orthogonal directions of measurements, therefore this method suffers from the same limitation as for the anisotropy method, because it can not address simultaneously two parameters which are used to characterize an ensemble of molecules in the focus volume of a microscopy objective. The usual approach used to circumvent this limitation has been to simplify the problem by restricting it to areas of samples where the mean orientation is a priori known and appropriate [5, 6, 30, 31], or to study specific samples of perfectly controlled geometry [29, 27, 28], so that various orientations can be addressed in a controlled fashion. Another possibility is to repeat the same measurement on a rotated sample [8], which is not convenient in practice in microscopy.

Finally in this method there is also a blind angle('magic angle'). When the mean orientation of the molecules is at this angle, the linear dichroism has the same value for any molecular distribution [30].

1.4 Angle resolved linear dichroism

In order to circumvent the limitations of LD mentioned above, a more refined mode of operation of LD measurement has been proposed by exploiting the full potential of polarized fluorescence imaging, based on the tuning of the excitation polarization [11, 32,

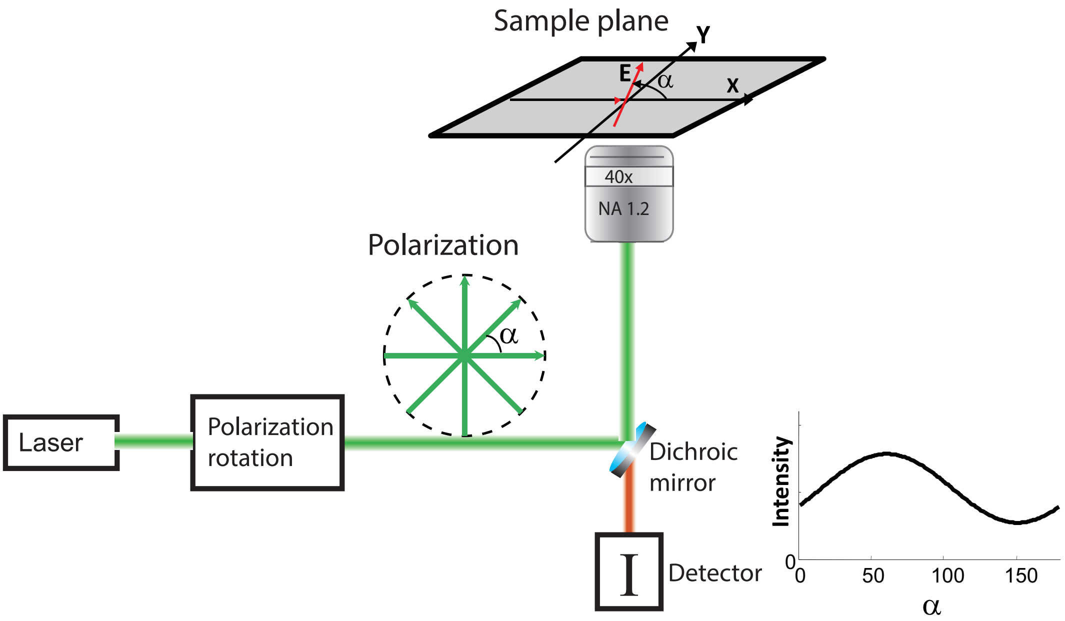

Figure 1.8: The scheme of angle-resolved linear dichroism. The excitation light is modulated by a polarization modulator so that the sample is excited sequentially by several excitation polarization angle denoted by α and the emission response on polarization angle α is recorded by detector without polarization analyzer.

33, 34]. In this method, that we call "angle resolved linear dichroism" (ARLD) (also called "polarization resolved fluorescence microscopy" below), the sample is sequentially probed using several excitation polarization angles denoted α, as illustrated in Fig. 1.8, and the corresponding emission response as a function of α is recorded by a detector without any polarization analyzer. Compared to LD which uses the emission responses of only two orthogonal polarization orientations, the α response curve allows the retrieval of the complete information on both molecular orientational order (ψ) and average orientation (ρ) in a non-ambiguous manner in a whole image. This information can be obtained without the need to rotate the sample and is not restricted to particular regions.

This method was firstly implemented in two-photon excitation polarization resolved microcopy allowing sample sectioning [11], however a polarization detection was used which happens to be potentially sensitive to depolarization mechanisms. It also suffers from a low level of signals.

Recently, DeMay have reported [32] that four sequentially recorded fluorescence images excited respectively with 0°, 45°, 90° and 135° polarized light allow to quantify rapidly

(0.3 fps) both orientation and anisotropy of septin proteins in live yeast, without any a priori orientational knowledge, a clear improvement as compared to conventional LD. However, in order to avoid polarization distortion induced by a dichroic mirror, the reported work used a wide field trans-illumination configuration, which does not provide axial sectioning and then restricts the technique to thin samples, and causes photo-bleaching.

An epi-fluorescence scheme, still based on wide field geometry, has been proposed by Lesoine [34]. In this work, however, experimental data recorded on controlled samples do not show the expected results yet and still require, according to the authors, further investigations. The reason was probably photo-bleaching problems and instabilities in the liquid crystal device used to switch polarizations. In these two wide field schemes, four fluorescence images are recorded and processed as a defined anisotropy presented in eq. 1.12:

$$\text{anisotropy} = \frac{\sqrt{A^2 + B^2}}{C} \tag{1.12}$$

with

$$A = (I_0 - I_{90}), B = (I_{45} - I_{135}), C = (I_0 + I_{45} + I_{90} + I_{135}) \tag{1.13}$$

where, I_0, I_{45}, I_{90} and I_{135} are the fluorescence intensities corresponding to different polarization orientations of the excitation light (0°, 45°, 90°, 135°).

1.5 Conclusion

In this chapter we have briefly presented the one-photon fluorescence process and important properties related to this work, including spectrum property, lifetime and polarization property. We have reviewed several polarization resolved fluorescence techniques about their principles, advantages, limitations and applications. We have introduced the principle of ARLD, which will be detailed in the next chapter.

Chapter 2

Angle-resolved Linear dichroism (ARLD)

Angle resolved linear dichroism as discussed in the previous chapter relies on the analysis of the dependence of fluorescence intensity on the polarization orientation of the exciting light. By rotating the polarization orientation of the exciting light, several fluorescence images of a sample are recorded. It allows retrieving the orientation information of an ensemble of fluorescence molecules without a priori knowledge of orientation. In this chapter we will detail the theoretical model and the implementation on a traditional confocal system. We will discuss the data monitoring conditions (signal levels, quality of excitation polarization state, data analysis), as well as the limitations of the technique.

2.1 Fluorescence emitted by an ensemble of dipoles

The polarization resolved steady state fluorescence intensity is modeled using a similar formalism as previously developed for two-photon fluorescence polarization microscopy [11]. It is based on the expression of the polarization dependence of the excitation photoselection of an ensemble of molecules. Due to the incoherent nature of fluorescence emission there is no phase relationship between the field emitted by all dipoles in the focal volume, therefore the fluorescence intensity emitted by an ensemble of dipoles is the sum of the emission intensity emitted by every single molecule weighted by their angular distribution function. The sum over all molecules intensities should be rigorously performed in time (over the integration time) and in space (over the focal volume). In this work we calculate steady states responses and we will therefore express the averaging processes as an average over only the orientation angles of molecules, which encompasses both time and space fluctuations.

2.1.1 Microscopic and macroscopic frame

For a single transition dipole excited by one photon, the emission intensity is proportional to absorption probability P_{abs} which represents the interaction between the dipole and the exciting field. The absorption probability has been detailed in eq. 1.2 and is written:

$$P_{abs} \propto |\vec{\mu}_{abs} \cdot \vec{E}(\alpha)|^2 \tag{2.1}$$

In this equation, the $\vec{\mu}_{abs}$ is the absorption transient dipole moment of the molecule and $\vec{E}(\alpha)$ describes the exciting field, following a polarization direction oriented by an angle angle α with respect to the X axis. In what follows, (X, Y) is the sample plane which is also the transverse plane, Z is the propagation direction. X is along the horizontal direction and Y is vertical.

In order to calculate the total emitting fluorescence intensity from the ensemble, the angular distribution is sampled with different oriented dipoles. A microscopic frame is introduced to describe the angular distribution of the dipole. In what follows we suppose that the dipoles $\vec{\mu}_{abs}$ and $\vec{\mu}_{em}$ lie along the same direction $\vec{\mu}$. This hypothesis has been discussed previously and is known to be valid for the molecular systems studed in this work [11].

In the microscopic frame shown in Fig. 2.1(a), the fluorescence dipole $\vec{\mu}$ is oriented with an angle θ with respect to the z axis (mean orientation of the ensemble), and its (x, y) projection with an angle ϕ with respect to the axis x. Therefore, the fluorescence dipole in the microscopic frame is given by:

$$\begin{bmatrix} \mu_x(\theta,\phi) \\ \mu_y(\theta,\phi) \\ \mu_z(\theta,\phi) \end{bmatrix} = \begin{bmatrix} \sin\theta\cos\phi \\ \sin\theta\sin\phi \\ \cos\theta \end{bmatrix} \tag{2.2}$$

The orientation of the microscopic frame in the macroscopic frame is characterized by its in-plane orientation ρ respect to the X axis and its out-of-plane orientation η respect to the (X, Y) plane, as shown in Fig. 2.1(b). Therefore, the orientation of a fluorescence

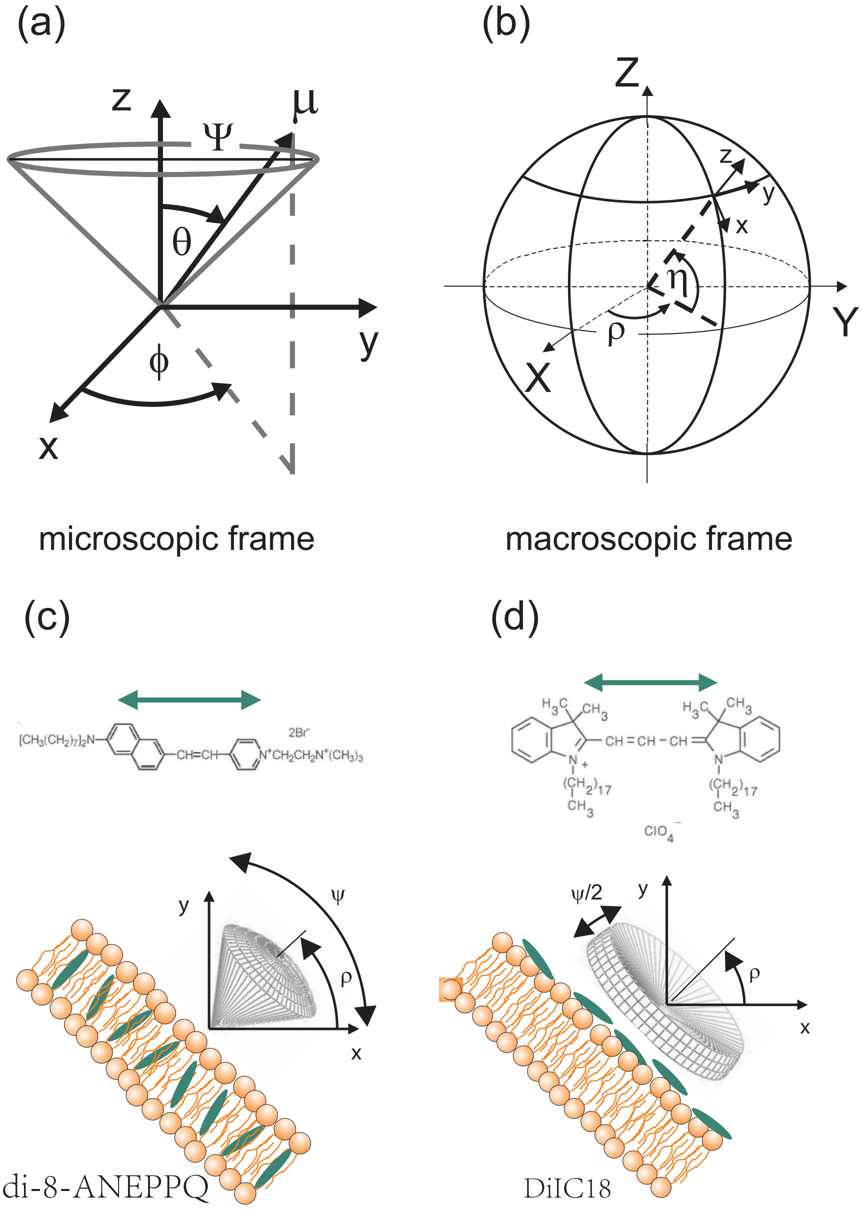

Figure 2.1: (a)A single dipole in the microscopic frame, the transition dipole μ is tilted an angle θ respect to the z axis(the mean orientation of the cone) and the projection on XY plane is rotated an angle ϕ respect to X axis, the cone aperture is ψ. (b) The orientation of the microscopic frame with respect to the macroscopic, the mean orientation has an out-of-plane angle η respect to XY plane and its projection on XY is presented by an angle ρ respect to X axis. (c) di-8-ANEPPQ lipid probe orientation distributed perpendicular to the membrane contour and described by a cone model. (d) DiIC$_{18}$ orientation distributed along the membrane contour and described by a pancake model.

dipole in the macroscopic frame can be obtained by applying the transformation matrix M:

$$\mathbf{M} = \begin{bmatrix} \sin\eta\cos\rho & -\sin\rho & \cos\eta\cos\rho \\ \sin\eta\sin\rho & \cos\rho & \cos\eta\sin\rho \\ -\cos\eta & 0 & \sin\eta \end{bmatrix}$$

The orientation of the transition dipole μ in macroscopic frame is thus expressed as:

$$\begin{aligned} \begin{bmatrix} \mu_X(\theta,\phi,\rho,\eta) \\ \mu_Y(\theta,\phi,\rho,\eta) \\ \mu_Z(\theta,\phi,\rho,\eta) \end{bmatrix} &= M \times \begin{bmatrix} \mu_x(\theta,\phi) \\ \mu_y(\theta,\phi) \\ \mu_z(\theta,\phi) \end{bmatrix} \\ &= \begin{bmatrix} -\sin\rho\sin\theta\cos\phi - \cos\rho\sin\eta\sin\theta\sin\phi + \cos\rho\cos\eta\cos\theta \\ \cos\rho\sin\theta\cos\phi - \sin\rho\sin\eta\sin\theta\sin\phi + \sin\rho\cos\eta\cos\theta \\ \cos\eta\cos\theta + \sin\eta\cos\theta \end{bmatrix} \end{aligned}$$

2.1.2 Distribution function

A normalized distribution function $f_\psi(\theta,\phi)$ is introduced to describe the dipole orientation distribution. In the most general case of a statistical distribution exhibiting a cylindrical symmetry along a main axis z, this distribution is defined by an angle ρ between its symmetry axis z and the X axis, and an out-of-plane angle η between z and its projection in the (X, Y) plane. The angular width of the distribution is defined by an angle ψ. Depending on the lipid probe structure, the function $f_\psi(\theta,\phi)$ can take different forms once they are embedded in a lipid membrane. We will consider here that the angle distribution probed by the molecules is sharp, which supposes that their interaction potential with surrounding molecules is abrupt. Other models have introduced a Gaussian distribution, however since this technique can not differentiate a sharp from a smooth distribution [35], we choose here simplest function. In the case of a lipid probe which dipoles lye parallel to the membrane lipid molecules (such as di-8-ANEPPQ) shown in Fig. 2.1(c), the angular distribution in the frame of the membrane is written as:

$$f_\psi(\theta,\phi) = \begin{cases} \frac{1}{4\pi\sin^2(\psi/4)} & \text{if } \theta \le \psi/2 \\ 0 & \text{else} \end{cases}$$

This distribution will be refered as the "cone" model.

In the case of a lipid probe which dipoles lie perpendicularly to the membrane lipid molecules (such as DiIC18, 1,1'-dioctadecyl-3,3,3',3'-tetramethyl indocarbocyanine perchlorate) shown in Fig. 2.1(d), the angular distribution in the frame of the membrane is written as:

$$f_\psi(\theta,\phi) = \begin{cases} \frac{1}{4\pi\sin^2(\psi/4)} & \text{if } (\pi-\psi)/2 \leq \theta \leq (\pi+\psi)/2 \\ 0 & \text{else} \end{cases}$$

This distribution will be refered as the "pancake-like" model.

2.1.3 Emitted fluorescence

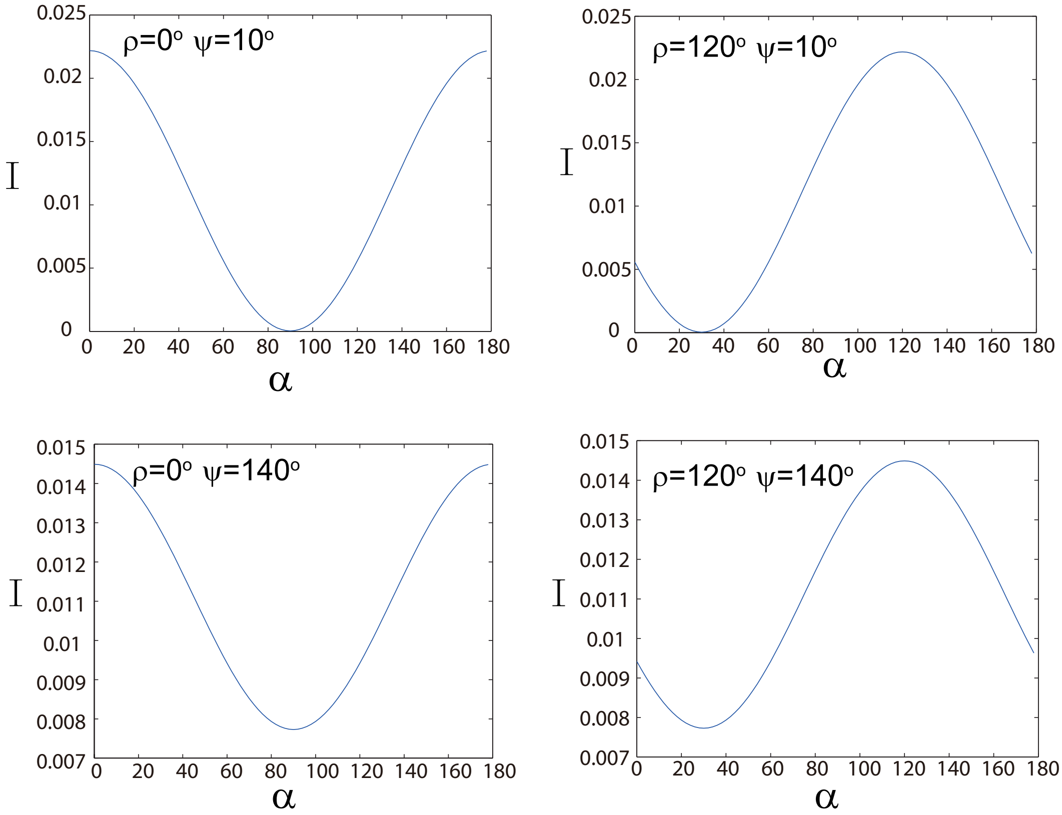

Figure 2.2: Theoretical polarization resolved intensity for different cone models.

Finally, the steady state fluorescence intensity from an ensemble of dipoles excited by linearly polarized light can be expressed as:

$$I_{\rho,\psi,\eta}(\alpha) = \int_0^{2\pi} \mathrm{d}\phi \int_0^{\pi} |\vec{\mu}(\theta,\phi,\rho,\eta)\cdot\vec{E}(\alpha)|^2 f_\psi(\theta,\phi) J(\theta,\phi,\rho,\eta)\sin\theta \mathrm{d}\theta \tag{2.3}$$

where, a function J is introduced to account for the detection probability of fluorescence [5] (see Appendix A)

Note that here we suppose that the incident field comes from a planewave this has been shown to be a reasonable assumption when exciting molecules that are mainly in the sample plane. [11].

According to the eq. 2.3, we have calculated the polarization resolved intensities (total intensity is normalized to 1) for different "cone" models as shown in Fig. 2.2. It appears clearly that the polarization resolved intensity I has a sinus dependence to the polarization angle α. Moreover the ρ value can be visualized as the position of the maximum intensity and the contrast of the intensity change depends on the ψ value (indeed as expected, the more disordered the molecular distribution is, the less contrasted is the polarization response). Although not shown here, the same observation were made for all combinations of ρ and ψ.

2.2 Setup

The experimental setup is designed in order to record this dependence $I(\alpha)$ at any pixel of a fluorescence image. Considering that we investigate single cells and artificial membranes, we use the epi-confocal configuration to supply optical sectioning.

2.2.1 Optical setup

Measurements are carried out on a custom confocal microscope system, adapted to allow a full control of the polarization state of the excitation beam as shown in Fig. 2.3. The excitation is provided by a polarized continuous wave laser (Calypso, Cobolt) emitting at 491 nm that delivers linearly polarized light whose angle of polarization α is sequentially rotated by a half-wave plate (WPH05M-488, Thorlabs) mounted on a motorized rotation stage (PR50CC, Newport). After reflection on a dichroic mirror (XF2037-500DRLP, Omega Optical), the excitation light is focused onto the sample by a water immersion objective lens (C-Apochromat 40x UV-VIS-NIR, NA=1.2, Carl Zeiss). The typical excitation power at the entrance of the objective lens is 10 μW, which is controlled by

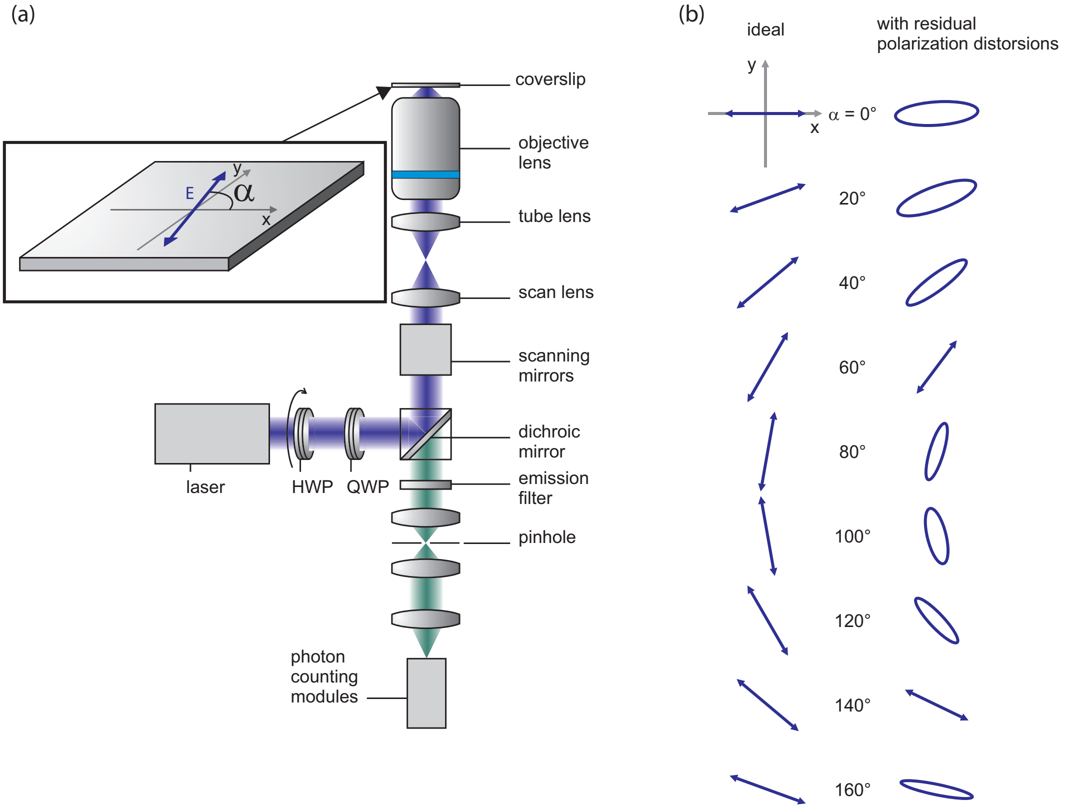

Figure 2.3: Angle resolved LD set-up. (a) Scheme of the experimental setup. HWP: motorized half-wave plate. The quarter wave plate (QWP) is used to compensate the large amount of elliptical distortion brought by the dichroic mirror in the excitation path. (b) Polarization state at the focus spot. Left, ideal linearly polarized field. Right, state of polarization as measured after compensation by the QWP

another half-wave plate combined with a polarizer (not shown) before polarization rotation. Emitted fluorescence is collected by the same lens in an epi-geometry, passes through the dichroic mirror, an emission filter (HQ540/80M-2P, Chroma) and a 75 μm diameter (1.25 Airy unit) confocal pinhole. The fluorescence is detected by a single photon counting module (SPCM-AQR-14, PerkinElmer Optoelectronics). Imaging is performed by scanning the excitation/observation volume in the sample using a set of two galvanometric mirrors placed between the dichroic mirror and the objective lens.

2.2.2 Polarization distortions

Dealing with polarization-resolved fluorescence studies requires an exact knowledge of the polarization state of the incident light at the focal spot of the excitation objective. Optical component are known to distort polarization state, in particular reflective optics which induce a phase shift between the s and p components of the incident polarization. Therefore even through the incident polarization is linear, the final one at the sample planes is likely to be elliptical. Using a polarization diagnostic tool based on the rotating quarter wave plate method described in Appendix B, the polarization state of light was measured at different places of the excitation path, for different incident polarization angles α between 0° and 180°. We noticed that, the reflection on the dichroic mirror introduces a notable retardance close to $\pi/2$ that could be partially compensated by inserting a quarter waveplate (WPQ05M-488, Thorlabs) in the excitation path as shown in Fig. 2.3(a). After compensation, the remaining polarization distortions were completely characterized and modeled by two polarizing element (with the parameters: fast-axis orientation θ, diattenuation γ and retardance δ summarized in Table 2.1) using the method described in Appendix B.2. The final polarization state at the sample plane without the objective was measured and is shown in Fig. 2.3(b).

We also dealt in the same way with the collection path by illuminating the sample plane, without the objective, by a lamp with a wavelength of 550 nm (set by an optical filter) to mimick fluorescent light. Weak polarization distortions could be observed and the distortion is modeled by three polarizing elements with parameters presented in Table 2.1.

Note that here the objective is not taken into account in these characterizations: we however measured it separately and found no significant distortion introduced by it.

The measured polarization distortions both in excitation and collection paths have been introduced in the theoretical model developed for polarization resolved analysis, which is detailed in the following.

To account for the distortions undergone by the excitation field $\vec{E}$, we replace the non distorted field (expressed here in the laboratory frame)

$$E(\alpha) = E_0 \begin{pmatrix} \cos\alpha \\ \sin\alpha \\ 0 \end{pmatrix} \tag{2.4}$$

where E_0 is the field amplitude, by:

$$E(\alpha) = E_0 M_{exc} \cdot \begin{pmatrix} \cos\alpha \\ \sin\alpha \\ 0 \end{pmatrix} \tag{2.5}$$

where M is the matrix product $M_{exc} = M_1(\gamma_1, \delta_1, \theta_1) \cdot M_2(\gamma_2, \delta_2, \theta_2)$, which accounts for the distortion parameters $(\gamma_i, \delta_i, \theta_i)$ summarized in Table 2.1 (see also Appendix B) for the equivalent optical elements i=1,2 acting as polarization distortion sources (phase plates) in the excitation path, with:

$$M_i(\gamma_i, \delta_i, \theta_i) = \begin{pmatrix} \cos\theta_i & -\sin\theta_i & 0 \\ \sin\theta_i & \cos\theta_i & 0 \\ 0 & 0 & 1 \end{pmatrix} \cdot \begin{pmatrix} 1 & 0 & 0 \\ 0 & (1-\gamma_i)e^{i\delta_i} & 0 \\ 0 & 0 & 1 \end{pmatrix} \cdot \begin{pmatrix} \cos\theta_i & \sin\theta_i & 0 \\ -\sin\theta_i & \cos\theta_i & 0 \\ 0 & 0 & 1 \end{pmatrix} \tag{2.6}$$

Table 2.1: Summary of the characteristics of polarization distortions in the optical setup.

Optical path	Element No	Orientation $\theta(°)$	Diattenuation γ	Retardance $\delta(°)$
Excitation	1	-16	0.28	22
	2	39	0.24	-20.5
Collection	3	79	0.20	140
	4	80	0	12
	5	127	0.2	12

In the detection path, the function $J(\theta, \phi, \rho, \eta)$ is the quantity affected by polarization distortions since it contains the information on how the radiation of emission dipoles is modified by optical elements acting as phase plates. Following the same methodology and notations introduced in [5], this function is re-calculated to account for the polarization distortions occurring in the detection path of the microscope. After calculating how emission dipoles' radiation fields are affected by the equivalent phase plates summarized in Table 2.1, it is found that $J(\theta, \phi, \rho, \eta) = J_X(\theta, \phi, \rho, \eta) + J_Y(\theta, \phi, \rho, \eta)$ is the sum of two polarized analysis X (horizontal) and Y (vertical) fluorescence emission components, which can be expressed as follows:

$$\begin{aligned} J_X(\theta, \phi, \rho, \eta) &= (|M_{11}|^2 K_1 + |M_{12}|^2 K_2)\mu_X^2 + (|M_{11}|^2 K_2 + |M_{12}|^2 K_1)\mu_Y^2 && (2.7) \\ & (|M_{11}|^2 + |M_{12}|^2) K_3 \mu_Z^2 + K(M_{11}M_{12}^* + M_{11}^* M_{12})\mu_X \mu_Y && (2.8) \end{aligned}$$

$$J_Y(\theta,\phi,\rho,\eta) = (|M_{21}|^2K_1 + |M_{22}|^2K_2)\mu_X^2 + (|M_{21}|^2K_2 + |M_{22}|^2K_1)\mu_Y^2 \tag{2.9}$$

$$(|M_{21}|^2 + |M_{22}|^2)K_3\mu_Z^2 + K(M_{21}M_{22}^* + M_{21}^*M_{22})\mu_X\mu_Y \tag{2.10}$$

where(K_1, K_2, K_3) are polarization coupling factors which depend on the numerical aperture of the objective ($n \cdot \sin$
$sigma_0$) as defined in [5], and K an additional parameter representative of an additional emission polarization cross talk due to collection path distorions: $K = -\frac{1}{6}(\cos^3\delta_0 + 3\cos^2\delta_0 + 3\cos\delta_0 - 7)$. M_{mn} are the matrix elements of the product $M = M_3(\gamma_3,\delta_3,\theta_3) \cdot M_4(\gamma_4,\delta_4,\theta_4) \cdot M_5(\gamma_5,\delta_5,\theta_5)$, which depends on the distortion parameters $(\gamma_i,\delta_i,\theta_i)$ summarized in Table 2.1 for all optical elements $i = 3, 4, 5$ acting as polarization distortion sources in the detection path.

Note that for collection path, historically we used two detectors which are respectively sensitive to the X and Y polarization direction. The collection distortion was finely modeled with three virtual distorting elements. However in the angle resolved LD where we measure the total fluorescence intensity so only the diattenuation affects the measurement.

2.3 Data processing

In this section it is presented how to process the measured data and retrieve the mean orientation ρ and cone aperture ψ. The precision of this technique is analyzed by Monte Carlo simulations. and the instrumental source of error such as sample drift, membrane local motion, photo-bleaching, etc. are analyzed. All the programs are written in Matlab.

2.3.1 Retrieval of the distribution parameters

After calculating the fluorescence response to a varying polarization angle α for molecular ensembles by equation 2.3, it is visible that $I_{\rho,\psi,\eta}$ exhibits a sine dependence relative to polarization angle α with a period of 180°. The signal can therefore be decomposed as a finite Fourier series:

$$I_{\rho,\psi,\eta}(\alpha) = I_0[1 + A(\rho,\psi,\eta)\cos(2\alpha) + B(\rho,\psi,\eta)\sin(2\alpha)], \tag{2.11}$$

with

$$A(\rho,\psi,\eta) = \frac{2}{I_0\pi}\int_0^{\pi} \mathrm{d}\alpha\, I_{\rho,\psi,\eta}(\alpha)\cos(2\alpha), \quad (2.12)$$

$$B(\rho,\psi,\eta) = \frac{2}{I_0\pi}\int_0^{\pi} \mathrm{d}\alpha\, I_{\rho,\psi,\eta}(\alpha)\sin(2\alpha), \quad (2.13)$$

and $I_0 = \frac{1}{\pi}\int_0^{\pi} I_{\rho,\psi,\eta}(\alpha)\mathrm{d}(\alpha)$

In practice, the fluorescence image is recorded at the equatorial plane of the cell, therefore we assume $\eta = 0$. The deviation from this condition is discussed in Section 2.5.1. The goal is therefore to determine the (ρ,ψ) parameters from the (A,B) coefficients. Using eq. 2.3, 2.12, the value $A(\rho,\psi)$ and $B(\rho,\psi)$ have be calculated for all values of ρ and ψ. Then the reverse relationship $\rho(A,B)$ and $\psi(A,B)$ were obtained numerically. Fig. 2.4 illustrates the unique relationships between (A,B) and (ρ,ψ) respectively for cone model and pancake-like model described in Fig. 2.1. The calculation has been performed without distortion and with the polarization distortion described in Section. 2.2.2. Clearly in both case a set of values (A,B) leads to a unique set of parameters (ρ,ψ) which shows the interest of this technique as compared with anisotropy (see Secttion 1.2.2). Compared to the maps of (ρ,ψ) versus (A,B) which show a disk-shape in the ideal case without polarization distortion, the maps are distorted when taking into account polarization distortions both in excitation and collection paths.

In practice, as shown in Fig. 2.5(a), a stack of fluorescence images are recorded with different angle α of the linearly polarized exciting light. From this stack, for every pixel the signal $I(\alpha_k)$ also is expanded as a finite Fourier series by calculating A and B using:

$$A = \frac{2}{I_0 N}\sum_{k=1}^{N} I(\alpha_k)\cos(2\alpha_k), \quad (2.14)$$

$$B = \frac{2}{I_0 N}\sum_{k=1}^{N} I(\alpha_k)\sin(2\alpha_k), \quad (2.15)$$

where $I_0 = \frac{1}{N}\sum_{k=1}^{N} I(\alpha_k)$ and N is the total number of images recorded. Theoretically, to retrieve the values of (ρ, ψ), at least 3 polarization images with polarization angle α uniformly spaced steps (for instance 0°, 60°, 120°) are required.

According to the calculated A and B values, the corresponding values of ρ and ψ can be independently retrieved from the calculated relationships shown in Fig. 2.4. The maps of $\rho(A,B)$ and $\psi(A,B)$ are sampled from -1 to 1 with a sampling of 0.02 along A and

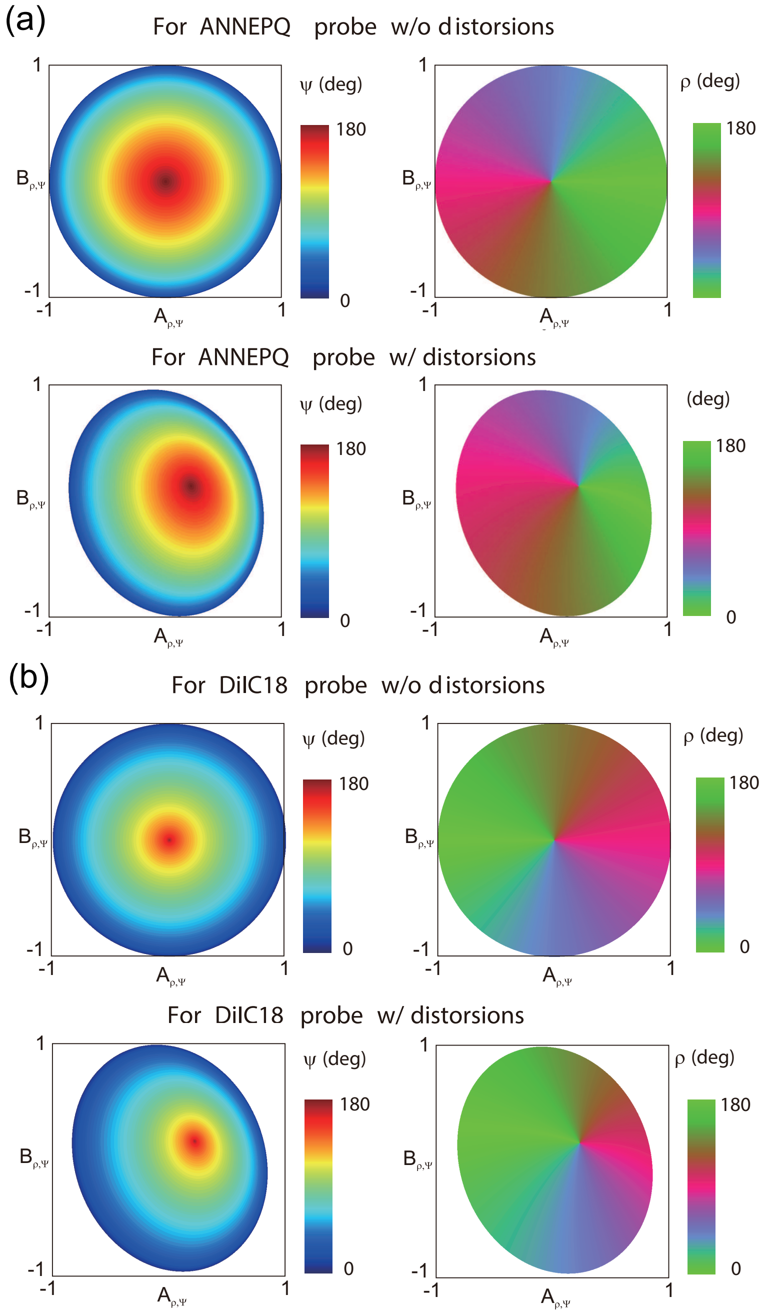

Figure 2.4: Reference maps for data processing. Simulated colormaps illustrating the unambiguous relationship between the coefficients (A, B) (coordinates) and the set(ρ, ψ) (color scale, angles are in degrees). (a) for the di-8-ANEPPQ lipid probe, cone model; (b) for the DiIC18 lipid probe, pancake-like model. Top: ideal optical system with no polarization distortions; bottom: with the polarization distortions of the system used in this work.

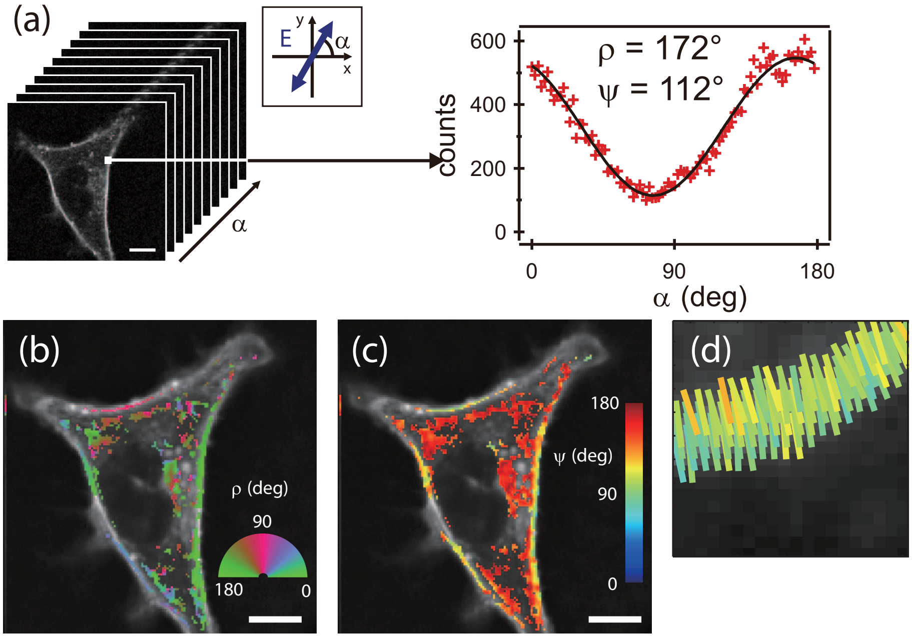

Figure 2.5: (a) Example of measured data. (b) The retrieved image of ρ. (c) The retrieved image of ψ. (d) Another possible representation allows to combine the ρ and ψ values: each stick is oriented with the retrieved angle ρ, while its color gives the value of ψ. In(b), (c) and (d), the gray scale image represent the total fluorescence. The cell is a living COS-7 cell measured at 37°C after labeling by ANEPPQ (1 μM). A higher orientational order appears clearly in the plasma membrane compared to a more isotropic distribution of internalized lipid probes.

B. In processing values of ρ and ψ can be obtained in their own sampled maps from the indices of A and B (the integer values closest to $(1+0.02\times(A+1))$ and $(1+0.02\times(B+1))$). The data processing of all the effective pixels is done in parallel, which leads finally to images of ρ and ψ, as shown in Fig. 2.5 (b) and (c) (the interpretation of these data will be detailed in Section 2.4). A combined representation of ρ and ψ (Fig. 2.5(d)) is also introduced where the image pixel is replaced by a small stick which orientation is given by rho and color is given by the psi aperture angle. These images are obtained within a processing time of about 100 milliseconds in a standard personal computer. Note that this processing method is a considerable improvement comparing to previous works relating on a fit of the retrieved polarization responses [11] or on anisotropy measurements along a membrane contour [7].

2.3.2 Precision analysis

The precision of this method was assessed by Monte Carlo simulations. For a given set of (ρ, ψ) values, the theoretical dependence on polarization response $I(\alpha)$ is calculated using eq. 2.3 for a total intensity I_0. Using a Poisson random number generator (function "poissrnd" in Matlab, which adds Poisson noise to a theoretical value), 1000 different polarization responses were generated, and processed by the method described above to generate the corresponding ρ and ψ values, allowing to quantify the average values and standard deviations for ρ and ψ.

We performed these simulations for several sets of (ρ, ψ) and summarized in Fig. 2.6(a) and (d) respectively for the total intensities of 5000 counts and 1000 counts, where the cross denotes the average value for the set of (ρ, ψ) and the full width (height) of the rectangle corresponds to twice the standard deviation on $\rho(\psi$, respectively). For the ψ that values that are covered by this work, namely between 60° and 160°, the uncertainty on ψ is usually smaller than 5° for a total intensity of 5000 counts. This uncertainty decreases to about 15° for a total intensity of about 1000 counts. Actually the uncertainty of ψ and ρ is seen to be reversely proportional to the square root of the total number of photons ($\delta_\rho, \delta_\psi \propto \frac{1}{\sqrt{I_0}}$), therefore this precision is getting better for higher intensities. This result shows that the total number of photons ia a determining number to gain a high precision in the parameters determination: reaching a high I_0 value can be done by increasing the number of polarization angles α (N in eq. 2.15), increasing the integration time per pixel, or increasing the incident intensities of excitation light. This last solution is the least favored due to possible photo-bleaching, which can also occur with a longer integration time. Note that total intensity of 2000 to 5000 is quite typical in membranes labeled with reasonable labeling conditions.

2.3.3 Sources of bias and error criteria

During the data processing, with the method presented above, any experimental polarization response dataset will result in corresponding values of A and B. However, there are some datasets that are very distorted due to experimental reasons such as sample drift, membrane local motion, photobleaching. There is therefore a need for a criteria to discard these distorted measurements. In our data processing, the validity of the retrieved set

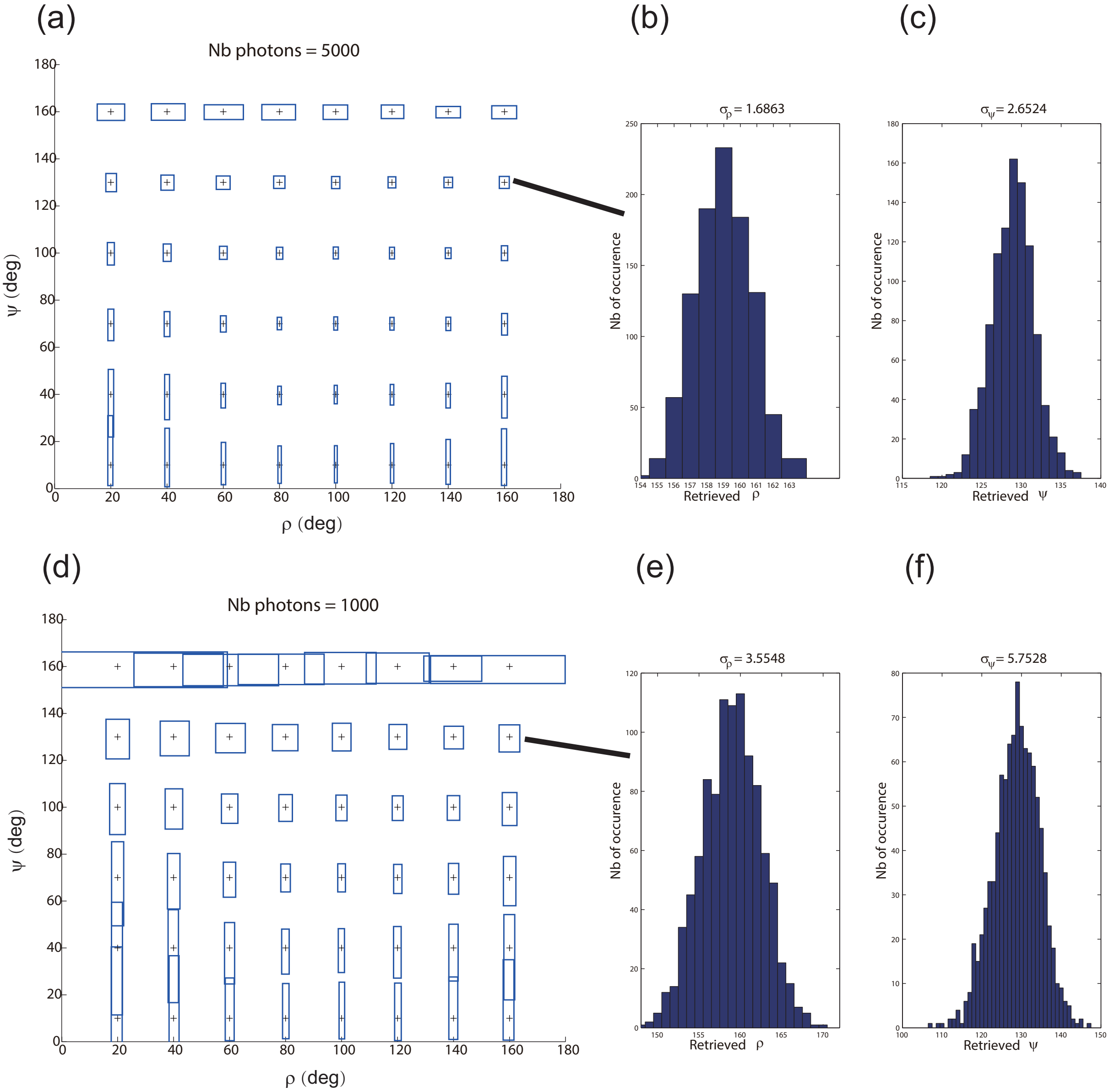

Figure 2.6: The precision of this method for measuring ρ and ψ assessed by means of Monte Carlo simulations. Histograms illustrate the retrieved values (ρ, ψ) for the case $\rho = 160°$, $\psi = 130°$, with the corresponding standard deviations. (a), (b) and (c) are for the total intensity of 5000 counts and (d), (e) and (f) are for the total intensity of 1000 counts.

(ρ, ψ) is assessed by calculating the normalized chi-square value [36]

$$\chi^2 = \frac{1}{N}\sum_{k=1}^{N} \frac{[I_{\text{exp}}(\alpha_k) - I_{\text{theory}}(\alpha_k)]^2}{\sigma_I^2(\alpha_k)} \tag{2.16}$$

where $I_{\text{theory}}(\alpha_k) = I_0[1 + A_{\rho,\psi}\cos(2\alpha_k) + B_{\rho,\psi}\sin(2\alpha_k)]$, with the $A_{\rho,\psi}$ and $B_{\rho,\psi}$ values calculated from the experiment data $I_{\text{exp}}(\alpha_k)$. The variance $\sigma_I^2(\alpha_k)$ is assumed to be equal to the photon counts $I_{\text{theory}}(\alpha_k)$ because of the Poisson statistics used in this work. By calculating χ^2, the distorted measurements caused by instabilities can be identified because they differ from theory by more than what is expected from photon shot noise and could be rejected automatically in data processing. By testing a large range of lipid membranes samples, we found an experiential rejection threshold χ_f^2 that is related to total fluorescence intensity and given by:

$$\chi_f^2 = \chi_0^2 + \frac{\chi_{max}^2 - \chi_0^2}{I_{max}} I_0 \tag{2.17}$$

with $\chi_0^2 = 2$, $\chi_{max}^2 = 15$, $I_{max} = 1 \times 10^5$ Note that this equation is deduced from an empirical check of the data, behaving with typical fluctuation behaviors and typical ranges of signal.

When the calculated χ^2 is greater than χ_f^2, the data is discarded. Fig. 2.7 presents examples of filtering out of distorted measurements from experiment the data by calculating χ^2. For the reasonable measurement with $\chi^2 < \chi_f^2$, the residuals $I_{\text{exp}} - I_{\text{theory}}$ are almost located in the range of $\pm\delta$ (δ standard deviation : $\sqrt{I_{theory}}$). Oppositely for the distorted measurements with $\chi^2 > \chi_f^2$, the residuals surpass this range, which means that the data have to be discarded. Finally the data processing and analysis consists in two steps:

1. setting a total intensity threshold value I_0 below which the pixels are discarded. This first step ensures a good determination precision for the parameters (ρ, ψ).

2. calculating χ^2 to discard these distorted measurements.

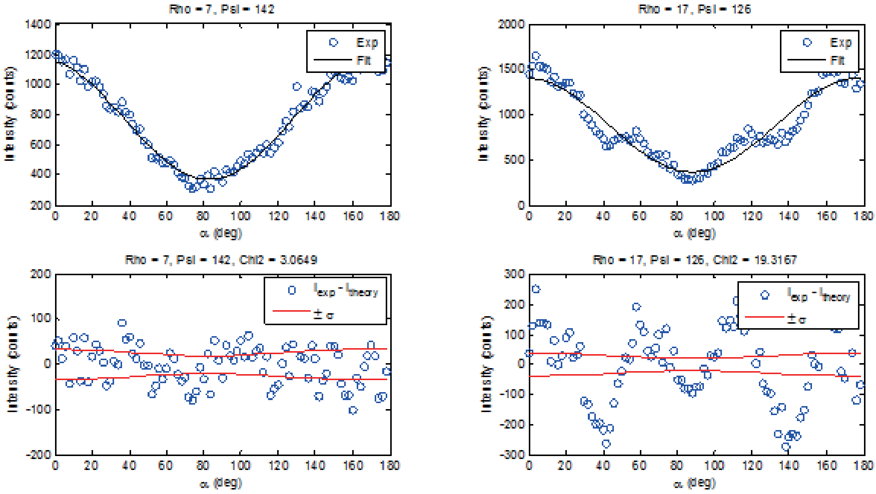

Figure 2.7: Illustration of the data filtering procedure. Raw data are plotted with blue circles. The fitting theoretical curve is displayed in black. Below: corresponding plot of the residuals $I_{\text{exp}} - I_{\text{theory}}$. The range $\pm\delta$ is represented by red curves. Left: $\chi^2 = 3.1$ below the rejection threshold. Right: $\chi^2 = 19$ above the rejection threshold.

2.4 Example of measurements

2.4.1 Giant unilamellar vesicles labeled by DiIC$_{18}$

To validate this technique, a preliminary analysis was performed on giant unilamellar vesicles (GUVs), which constitute spherical model membranes. The GUVs were fabricated by electroformation [37] using a mixture of DOPC (1,2-dioleoyl-sn-glycero-3-phosphocholine) and the staining dye (see Section C.1). The dyes that is used was DiIC$_{18}$(3) (Invitrogen), a lipophilic membrane stain that lies on the membrane surface, and whose angular distribution can be described using the pancake-like model (see Fig. 2.1 (d)). And the molecular ratio of dye to DOPC lipids is typical 1 : 1000. In this sample, the molecule angular distribution is supposed to be homogeneous over the whole membrane contour.

Fig. 2.8 exhibits an example of measurement. Fig. 2.8 (a) present the total fluorescence intensity which sums up the eight direct neighbors for every pixels. Target pixels can be found using threshold of 20000 and processed using the data processing method (Pancake model disks) presented above. The χ^2 value was calculated for every target pixel. According to the χ^2 value and the total intensity (I_0), these distorted pixels can be filtered out using the χ^2_f criteria presented above which is related to the total intensity, illustrated by a red line in Fig. 2.8 (c). The pixels which has a larger χ^2 than what is expected for its total intensity I_0 and appears above the red line would be thought as the distorted pixel due to possible local fluctuations. For instance, the pixel labeled as "A" in Fig. 2.8 (b) with a large χ^2 appears to be affected by visible fluctuations as illustrated in Fig. 2.8 (d) and was rejected. After filtering these distorted pixels, the ρ and ψ values for "good" pixels were plotted respectively in Fig. 2.8 (e) and (f) which are superimposed in the gray scale map of the total intensity. As expected the molecular angular distribution ψ behave homogenously around the whole contour, as illustrated in Fig. 2.8 (g). Over the whole contour the ψ value is constant with a value $\psi \sim 76^\circ$, with a standard deviation of 8° which is close to the values obtained in similar systems using fluorescence anisotropy [38, 11].

2.4.2 Giant unilamellar vesicles labeled by di-8-ANEPPQ

The test on GUVs presented above is made for the "pancake" model. In this section a test is also made on GUVs with labeled by dye di-8-ANEPPQ which inserts perpendicularly to the membrane, and is therefore described by the "cone" model (see Fig. 2.1 (c)). The data processing procedure is similar as used for GUVs labeled by DiIC$_{18}$. The only difference is that here we used the disks made for the 'cone' model in the data processing (see Fig. 2.4 (a)).

Fig. 2.9 shows an example of measurement. Using the χ^2 threshold the distorted pixels were discarded. For the left 'good' measurements, the ρ and ψ value are presented respectively in Fig. 2.9 (a) and (b). The molecules over the whole contour exhibits a uniform angular distribution with $\psi = 98^\circ \pm 8^\circ$. This number is very close to the values obtained in similar systems using fluorescence anisotropy [38, 11].

2.4.3 An application in Cos-7 Cells

Compared to the artificial membrane GUVs, the morphology of cell membranes is more complex. In addition to very different molecular content (with the presence of different lipids, cholesterol, proteins), the cell membrane is also affected by local morphological changes with wrinkles of different scales [1, 2] due to vesiculation, trafficking, endocytosis, exocytosis, interaction with the cytoskeleton. As shown in Fig. 2.10 where a portion of cell membrane was investigated, wrinkles that may be present (at a scale below the confocal resolution) exhibit a larger ψ than the membrane with flat contour.

Here we show an illustration of application of this technique in reporting membrane morphological changes treated with different drugs. In this work, COS-7 cells are treated with macroscopic modifications and drugs which are known to affect the cytoskeleton: Hypotonic shock (which induces a swelling of the cell), Cytochalasin D (which provokes actin depolymerization), Latrunculin A (an actinpolymerization inhibitor), Japlakinolide (which stabilizes actin filaments) (see [13] for the detail of the treatements). In this study, the cells were labeled with di-8-ANEPPQ. For each treatment, a typical sample is selected to illustrate the ψ map in Fig. 2.11(a). In order to avoid the influences induced by individuality of a single sample, one treatment over 12 cells is used to create a global histogram of ψ values. The results were presented in Fig. 2.11(b) where the histograms for cells treated with different drugs were compared with that of cells without treatment. Moreover, for every treatment the average values and standard error of the mean (SEM) over all pixels are presented in Fig. 2.11(c).

Among this treatments, mechanical disruption of the cytoskeleton by a hypotonic shock leads to an increase of molecular orientational order, an effect which is also observed using Cytochalasin D, Latrunculin A, lead to a somewhat similar effect, with additional heterogeneities. Jasplakinolide, provokes a new population of high disorder around $\psi \sim 150°$, which seems to be correlated with the visible additional membrane wrinkles around its contour, but also with invisible features occurring at the sub-diffraction scale. "ARLD is shown here to be a precise quantitative tool of molecular order measurement in cell membranes, in particular sensitive to local morphology changes that can occur at sub-diffraction scale [13]. Note that even if the molecular concentration might rise in membrane folds and therefore energy transfer is likely to occur in these regions, the present technique is insensitive to this effect. This is extensively detailed in Appendix A.

2.5 The limitations

2.5.1 Out-of-plane orientation η

Above, all the measurements and analysis were performed under the assumption that the mean orientation of the cone is in the sample plane, namely $\eta = 0°$ with the definition of η in Fig. 2.12(a). To evaluate the influences of the out-of-plane orientation η on ψ, a Monte-Carlo simulation was made for a modeled cone with ($\rho = 0°, \psi = 120°$) with different η values ranging from 0° to 180°. In this simulation, for each η the polarization resolved intensity data was generated by expression 2.3, and then 1000 experiments data were generated with 5000 total number of photons and Poisson noise. By utilizing our ψ retrieving method in these 1000 data, an average ψ and standard deviation could be obtained for the corresponding η. As shown in Fig .2.12(b), the ψ is overestimated when η increases for the reason that the cone projection in the sample plane tends towards a more isotropic distribution function when this cone is tilted out of the sample plane. For relatively low values of η ($< 20°$), a few degree of bias on ψ is induced. For the case where $\psi = 120°$, the bias is seen to be within a 10% range when η reaches 45°.

This was experimentally confirmed on a COS-7 cell membrane contour at different height Z above the sample surface (cell adherence plane) presented in Fig. 2.12(c). Fig. 2.12(d) and (f) show the fluorescence image and the retrieved map of ψ. As expected, below and above the cell adherence plane, the ψ is overestimated. At the top, the ψ reaches 180° because of the isotropic projection on sample plane.

This shows that this technique is limited to probe the 2D orientation ρ and the projected ψ in sample plane, even though the measurements in GUVs and cells provide generally a easy way to visualize their equatorial plane. Nevertheless it would be interesting to reach the top or bottom of a cell surface of regions close to the surface such as focal adhesion region for instance. A method will be proposed to retrieve the 3D orientation of molecules in an ensemble in Chapter 4.

2.5.2 Measurement speed

Our method was performed in a conventional laser-scanning confocal microscopy, which records a fluorescence image by employing two galvanometric mirrors to scan in X and Y directions. To get a high precision of about 2° on the retrieved ρ and ψ, 90 polarization steps need to be taken in the measurement in the labeling and intensity conditions used in this work. Typically, 150x150-pixel images were recorded with $100 \mu s$ pixel dwell time, yielding to an acquisition duration of about 5 min, including instruments communication delays. Reducing the number of polarization steps would increase the speed of measurements, however at the expense of a lower precision. So this technique is clearly limited by its sequential acquisition scheme, and therefore can only address static samples .

2.6 Conclusion

In this chapter we have presented the theoretical calculation of emission fluorescence from an ensemble of dipoles. In the theoretical calculation, a simple model has been introduced to characterize the molecular angular distribution. The implementation of ARLD in a conventional confocal system has been reviewed, and for this setup the polarization distortion has been roughly compensated. An efficient data processing method has been developed which allows reducing the processing time with high precision and filtering out the distorted measurements. By taking into account the remaining polarization distortion in the theoretical model, this data processing method can get rid of the influences of polarization distortion in final results. The precision analysis based on the Monte Carlo simulations has shown that the precision of this method reaches a few degrees on both ρ and ψ parameters for a few thousands photons, which are realistic measurement conditions. More generally this precision is determined by the recorded total numbers of photons. GUVs as an ideal testing sample has proven that this setup works as expected. We have presented an application of this method in reporting the morphological changes of cell membranes. In chapter 3, we describe a parallel confocal setup based on Nipkow-type spinning disk which immensely accelerate the measurement speed to a time scale of seconds, while keeping the same level of precision and without sacrificing the imaging capabilities offered by confocal microscopy.

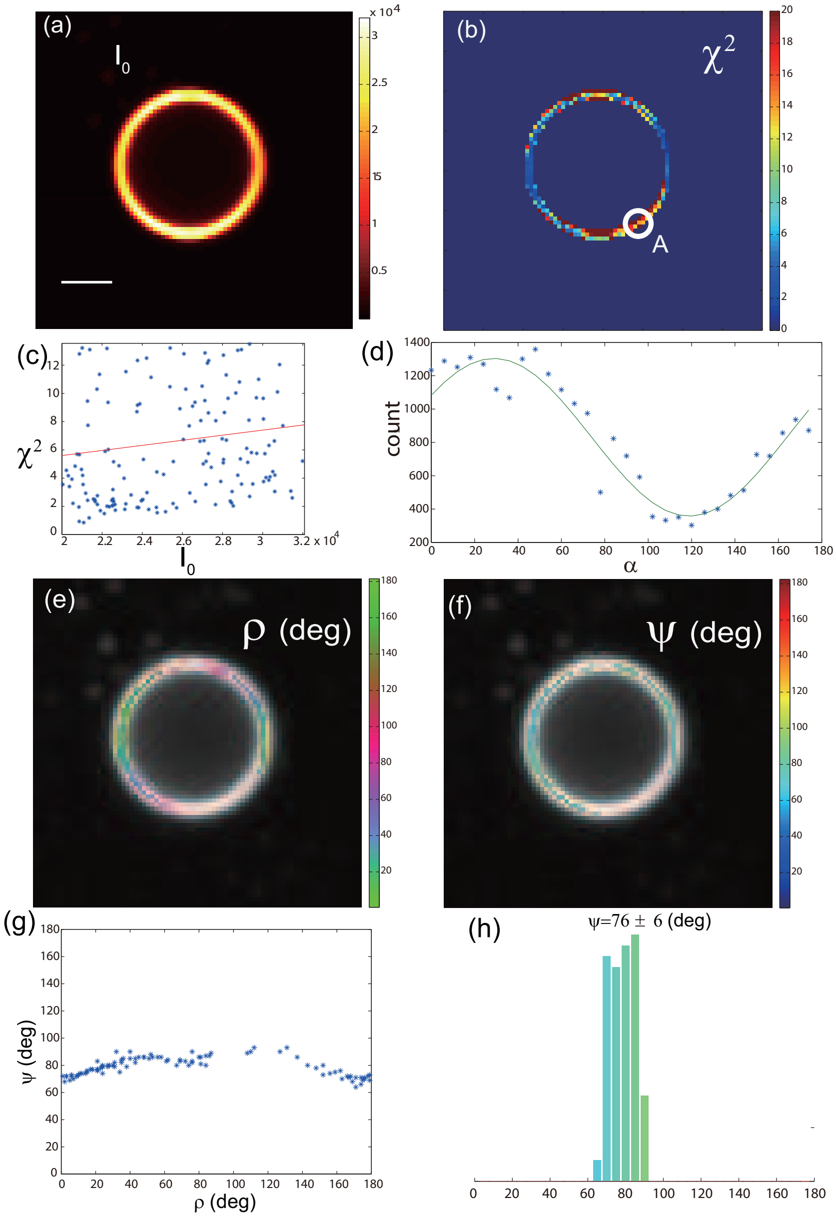

Figure 2.8: Validation of the method with giant unilamellar Vesicles labeled with DiIC$_{18}$. (a) Total fluorescence image with the bining of 3 × 3 pixels. (b) Calculated χ^2 values for target pixels. (c) χ^2 vs. total intensity I_0, the red line is the threshold above which the data are discarded. (d) Measured polarimetric responses for point A labeled in (b) and the retrieved theoretical responses showing photo-bleaching behavior. (e) ρ-image superimposed with the fluorescence intensity image. (f) ψ-image superimposed with the fluorescence intensity image. (g) ψ vs. ρ. (h) Histogram of ψ. Scale bar 5μm.

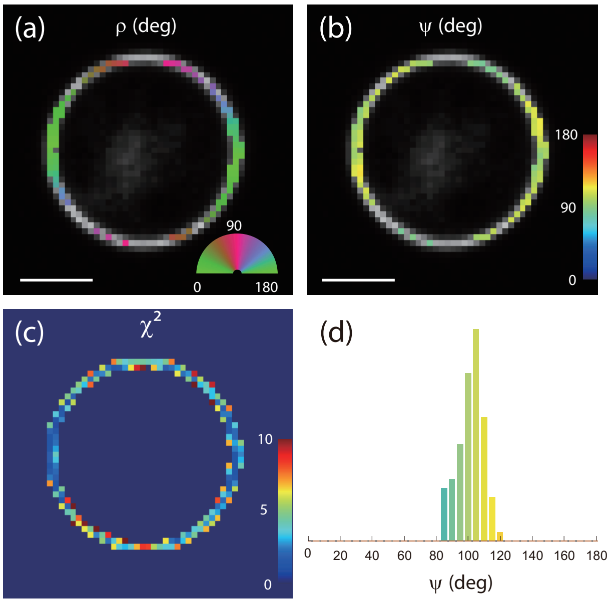

Figure 2.9: Validation of the method with giant unilamellar vesicles labeled by di-8-ANEPPQ. (a) ρ -image superimposed with the fluorescence intensity image. (b) ψ-image uperimposed with the fluorescence intensity image. (c) χ^2-image. (d) Resulting histogram of ψ. Scale bar 5μm.

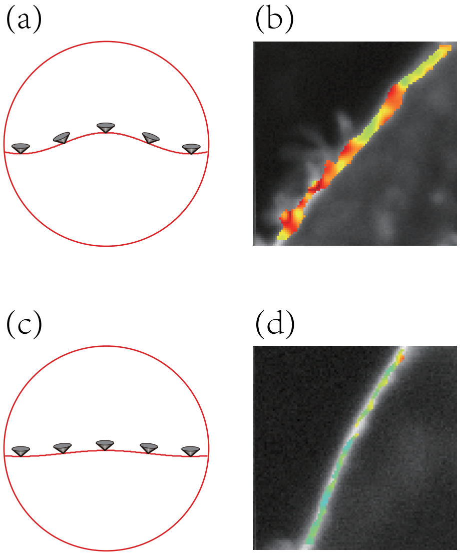

Figure 2.10: The cell membrane with wrinkle (a) and flat (c) shapes located in focal volume denoted by red circle. The winkle membrane exhibits a larger ψ value (b) than a flat membran (d).

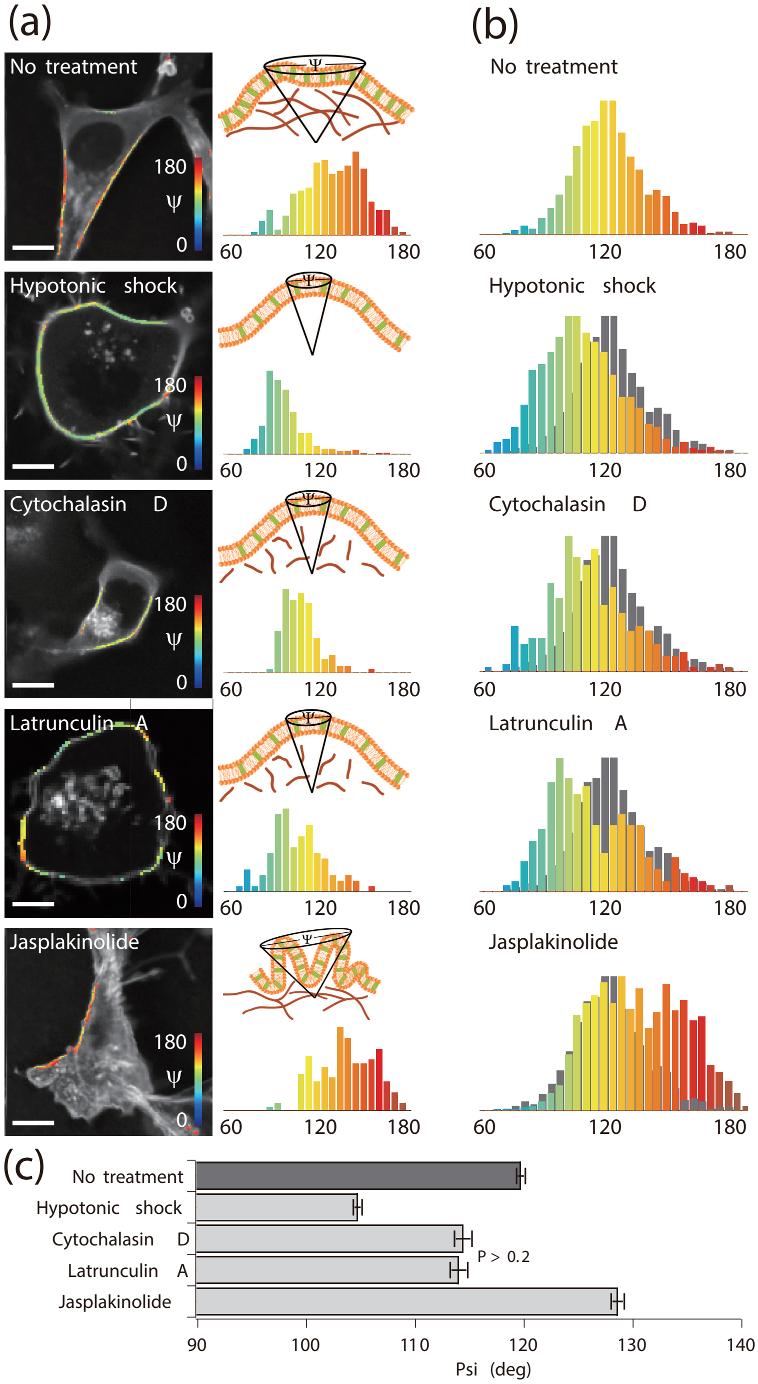

Figure 2.11: Molecular order effect of actin perturbation in COS-7 cells labelled with DiIC$_{18}$. (a) maps (superimposed to the fluorescence intensity image) from top to bottom: no treatment, Hypotonic shock, Cytochalasin D, Latrunculin A, Japlakinolide. (b) Histograms of the measured values on 12 cells for each treatment (in grey: reference histogram with no treatment). (c) Average and SEM values represented for each treatment.

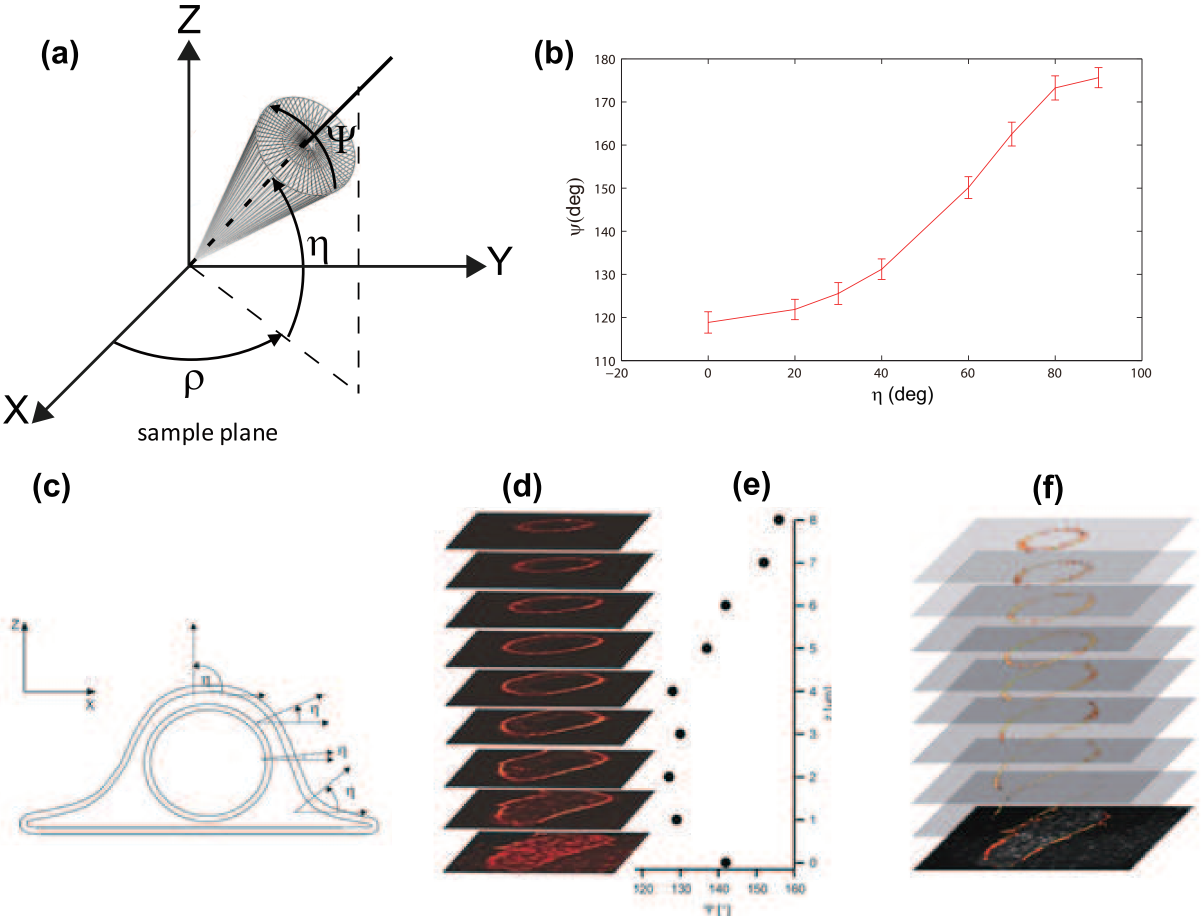

Figure 2.12: Polarization resolved fluorescence measurements and simulations, out of the membrane equatorial plane. (a) 3D cone model in the macroscopic frame, ρ: in-plane mean orientation, η: out-of-plane orientation and ψ: cone aperture (b) Simulation of ψ values for the modeled situation: $\psi = 120°, \rho = 60°$, for an increasing η from 0° to 90°. (c)The out-of plane angle η in a cell membrane. (d) Fluorescence images of a COS-7 cell at different Z values above the sample adherence plane. (e) Average ψ values on the cell membrane contour, measured for each plane represented in (c). (f) Corresponding ψ images.

Chapter 3

High frame rate confocal ARLD

The angle-resolved linear dichroism techinique proposed above allows to retrieve the mean orientation and the width of orientation distribution for an ensemble of dipoles in heterogenous samples. That has been proven in a scheme based on conventional laser scanning confocal microscopy, as presented in Chapter 2. However, the image recording in this setup relies on point-by-point scanning and the polarization control of excitation light is realized by half wave-plate rotation driven by a motor. The sequential acquisition scheme and these mechanical elements make this technique highly time consuming, therefore it can not address dynamic samples.

Some others approaches have been recently reported, which immensely accelerate the measurement to the timescale of seconds. However, they were based on wide field illumination [34, 32], so that do not provide axial section and are restricted to thin samples. Moreover, photo-bleaching easily occurs in this scheme.

In this section, we propose an instrumental development to improve the acquisition speed without sacrificing the axial sectioning provided by confocal configuration, using a highly parallel confocal imaging system and fast polarization switching. For this purpose, we propose to perform the image acquisition using a high speed spinning disk confocal unit. This system is capable of generating and scanning patterns of thousands of excitation spots in the specimen, that are analyzed in parallel in a confocal detection scheme by a camera, allowing acquisition speed up to several hundreds of frames per second. Fast switching of the polarization state is provided by an electro optical modulator placed in the excitation path. With this technique, fast confocal images can be recorded at any desired polarization angle, which offers the possibility to build polarization resolved stacks, in order to provide real-time monitoring of molecular order in dynamic specimens.

3.1 Experiment setup

3.1.1 Parallel confocal imaging

In order to introduce the principle of parallel confocal imaging, we first recall the principle of confocal microscopy. The principle of confocal imaging was proposed in 1957 by Marvin Minsky [39]. Compared to traditional wide-field fluorescence microscopes where the exciting light illuminates the entire sample and the resulting fluorescence is recorded by a camera, confocal microscopy is able to reject the unfocused background light by using a point illumination and a pinhole in the detection path.

Fig. 3.1(a) presents a common scheme of a confocal microscopy. A laser beam is focused by an objective lens into a small (ideally diffraction limited) focal volume. The fluorescent light from the focal volume is then re-collected by the objective lens. A dichroic mirror separates off the emission light into the detection path, and the emission light is focused by a lens through a pinhole and then is detected by a photo-detection device (usually a photomultiplier tube (PMT) or avalanche photodiode).

In the scheme presented above, the pinhole is conjugated with the excitation volume only in the detection path. In the excitation path, the excitation volume is conjugated to infinity. An alternative scheme can be used, where the pinhole is placed not only in the detection path but also in the excitation path, as shown in Fig. 3.1(b). A lens focuses the input parallel exiting beam into a pinhole which is conjugated with the excitation volume in the sample plane by an objective, and the emission light is focused back by the objective into the same pinhole and then reflected by a dichroic mirror into a detector. Due to conjugation with the same pinhole in both excitation and detection path, this scheme is intrinsically aligned.

In these two schemes, a set of two galvanometric mirrors or a sample scanning stage is needed to perform the point-by-point scanning to complete the image recording, which is sequential and therefore a highly time-consuming process. To reduce the scanning time, a named parallel confocal scheme has been proposed by replacing the single pinhole by an array of pinholes, as shown in Fig. 3.1(c) thus multiple excitation volumes are projected in the sample plane simultaneously and emission signals are imaged by a CCD camera.

This conception of parallel confocal was realized in the so-called Nipkow disk which was invented by Paul Nipkow in 1884 as an electrical image transmission device [40]. In a Nipkow disk, a series of pinholes were arranged in a spiral configuration in order to scan the specimen. As illustrated in Fig. 3.2, the laser beam illuminates a micro-lens arrayed

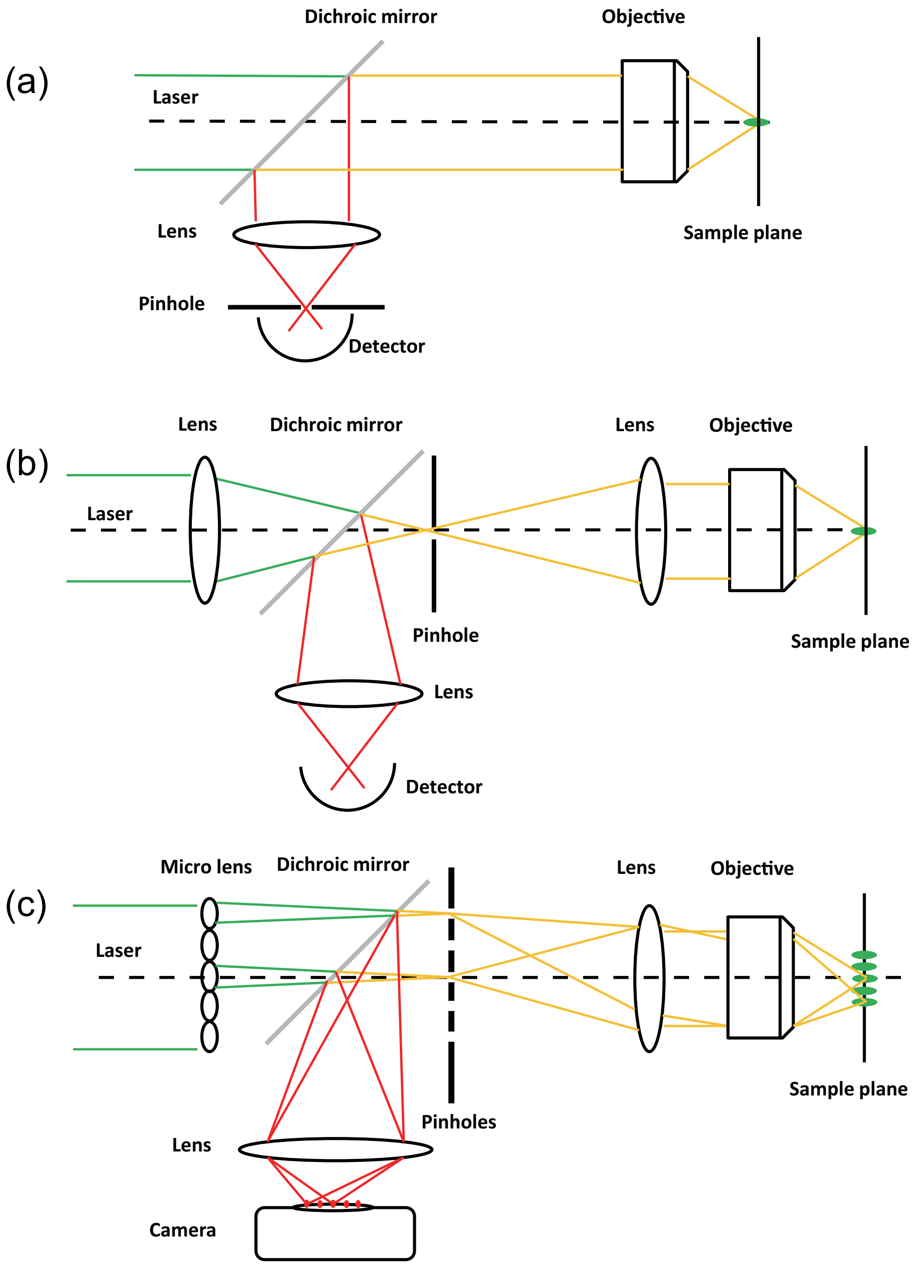

Figure 3.1: The optical configurations for (a) Conventional confocal microscopy, (b) modified laser scanning confocal microscopy, (c) Parallel confocal microscopy.

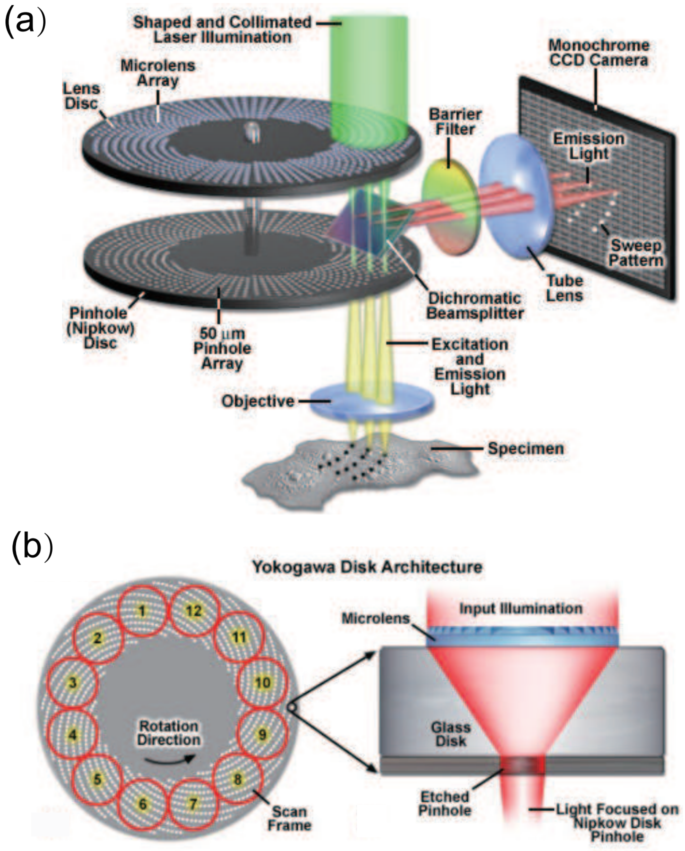

Figure 3.2: Yokogawa spinning disk unit optical configuration from [ZEISS campus online].

on a micro-lens disk and then is focused into the corresponding pinholes. These pinholes are conjugated in the sample plane by an objective and form thousands of focusing spots on sample plane at the same time. When the set of two disks rotates, these focusing spots move in the direction of rotation and scan the whole sample plane. The resulting fluorescence is imaged on the pinhole plane and finally is recorded by a CCD camera. Due to the confocal effect, the scattered light and background are rejected.

In our setup, we employed a spinning disk instrument designed by Yokogawa Electric Corporation of Japan, named the confocal scanning unit (CSU). The type used is CSU-10. Each disk contains approximately 20000 pinholes with a 250 μm spacing and the diameter of 50μm. The disk has a rotation speed of 1800 revolutions per minute, with the pinhole array pattern scanning 12 frames within a 360-degree rotation (see Fig. 3.2(b)). That yields a theoretical maximum frame rate of 360 frames per second at a resolution that is close to that of a scanning confocal microscopy [41].

3.1.2 Optical setup

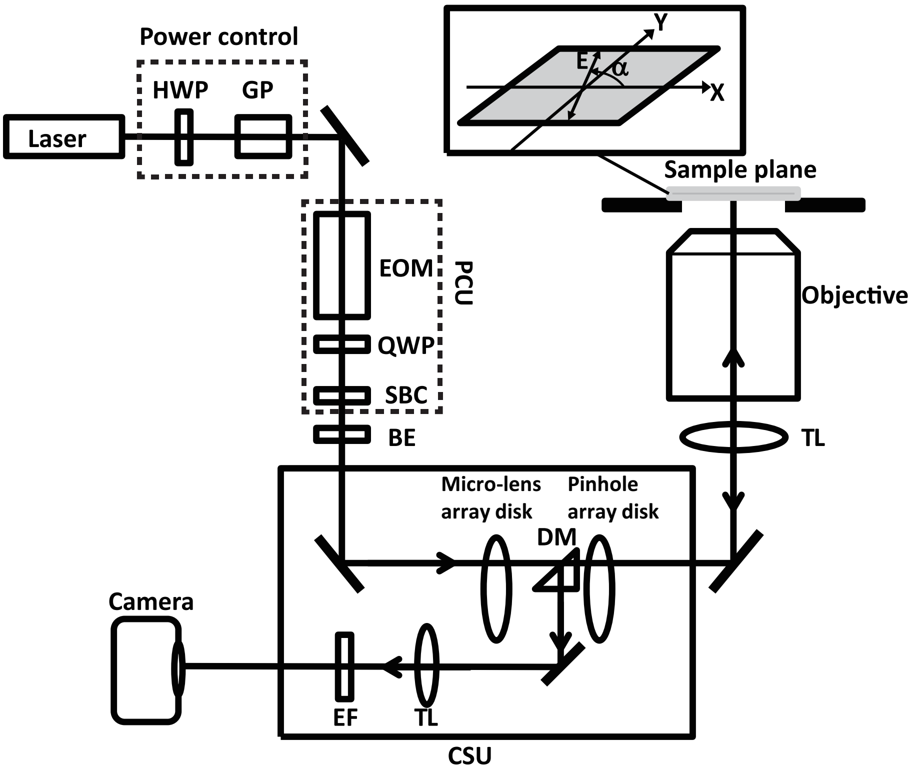

Figure 3.3: Experimental setup. HWP: half wave plate, GP: Glan polarizer, EOM: electrooptic modulator, QWP: quarter wave plate, SBC: Soleil Babinet compensator, BE: beam expander, DM: dichroic mirror, EF: emission filter, PCU: polarization control unit; CSU: confocal spinning disk unit.

The optical setup is presented in Fig. 3.3. It is based on a confocal spinning disk unit (CSU-X1-M1, Yokogawa) that is connected to the side-port of an inverted microscope (Eclipse Ti-U, Nikon). Laser excitation is provided by a continuous-wave vertically-polarized 488-nm optically-pumped semiconductor laser (Sapphire 488-20, Coherent). The cxcitation power is adjusted by rotating a half-wave plate (WPH05M-488, Thorlabs) in front of a Glan polarizer (GL5-A, Thorlabs) having its transmission axis vertical. The laser beam is then sent into the polarization control unit (see section 3.1.3) which requires a beam diameter lower than 3mm. It is then expanded using a 10× telescope, in order to reach a transverse size that is comparable to the area of the pinhole array disk that is imaged onto the specimen. In order to minimize the number of optical elements on the excitation path, the collimation and shaping optics of the CSU were bypassed. A mirror mount in the excitation path of the CSU, which was accessible from outside, was removed, so that the laser beam could, after reflection by a mirror , directly illuminate the microlens array disk of the CSU. The optical configuration of the CSU, which is detailed above, uses this microlens array disk in order to improve the illumination of the pinhole array disk, which is optically conjugated onto the sample plane, using a objective lens (Nikon Plan Apo VC 60×, N.A. = 1.2, water immersion) and a lens tube (×1.5) to get a ×90 magnification and fit better with the pinhole diameter. This generates about 1,000 excitation spots that illuminate simultaneously the specimen. The emitted fluorescence light is collected through the same objective lens, spatially filtered by the pinhole array disk, reflected by the dichroic mirror (Di01-T488-13x15x0.5, Semrock), spectrally filtered (bandpass 525/45) and imaged onto the camera (iXon 897 EMCCD, 512×512 pixels, Andor). Microlens and pinhole array disks rotate synchronously at a speed of 1,800 rpm, and can generate a uniform scanning by a rotation of 30° (12 frames per 360°), so that the exposure time of the camera needs to be an integral multiple of that time, namely $1/360 = 2.77$ ms. Note that there is no need to monitor or synchronize the rotation angle since any rotation of 30°, irrespectively to the start and stop position, provides an appropriate illumination [40].

3.1.3 Polarization control

In the confocal setup presented in previous chapter, the polarization of the exciting light was controlled by a rotating half waveplate which was driven by a motor. This mechanical rotation method, about 500ms for one rotation, is unacceptable in the high-speed setup which is designed to acquire a polarization-resolved stack with a time scale of seconds.

Therefore, in this setup an electro optical transverse modulator (EOM) (Pockels cell,model No 28-NP, Quantum Technology) is employed to perform the polarization control in the excitation path. The Pockels cell is based on the Pockels effect which describes the phase change produced on a polarized light passing through a uniaxial crystal submitted to an electric field. The response time is very short of the order of nanoseconds. The effect is a linear function of the voltage which is applied parallel to the crystal optical axis in the same direction as the propagation of the incident light. Therefore, the

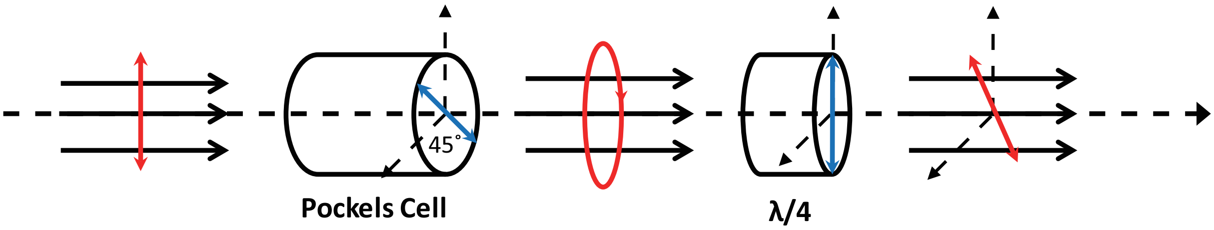

Figure 3.4: The optical configuration of polarization control unit using a Pockels cell combined with a quarter waveplate. Red arrows indicate the polarization states, and blue arrows represent the orientations of fast axes of the Pockels cell and the quarter waveplate.

Pockels cell can be employed to achieve retardance tunability of the polarized excitation light. Combined with a quarter-wave plate, it provides a linear polarization rotation of the excitation field within the timescale of nanoseconds.

Fig. 3.4 illustrates the scheme of rotating the polarization of the input light by using a Pockels cell. The Pockels cell is placed with its fast axis rotated at 45° with respect to the input linear polarization. Behind the Pockels cell a quarter wave plate (WPQ05M-488, Thorlabs) is inserted with its fast axis parallel to the input linear polarization.

This effect can be easily shown using the Jones formalism:

$$\begin{array}{ccccccc} \text{QWP} & \times & \text{Pockels cell} & \times & \text{Linear input} & & \\ \begin{bmatrix}1 & 0\\ 0 & -i\end{bmatrix} & \times & \cos(\Gamma/2)\begin{bmatrix}1 & i\tan(\Gamma/2)\\ i\tan(\Gamma/2) & 1\end{bmatrix} & \times & \begin{bmatrix}0\\ 1\end{bmatrix} & \propto & \begin{bmatrix}\sin(\Gamma/2)\\ -\cos(\Gamma/2)\end{bmatrix}\end{array} \tag{3.1}$$

In this equation, the input light is vertically-polarized and the retardance created by the Pockels cell is denoted by Γ. As presented in the right side of this expression, after passing through the quarter waveplate, the output light is linearly polarized with a rotation angle equivalent to half of the retardance Γ, which is proportional to the applied voltage. In this optical configuration, a rotation range of 180° is therefore achievable by a retardation range of 2π (one wavelength). With the specific crystal type (ADP 45° X cut with the length of 4.98 inch in our Pockels cell), it corresponds to a typical high voltage range of 400 V.

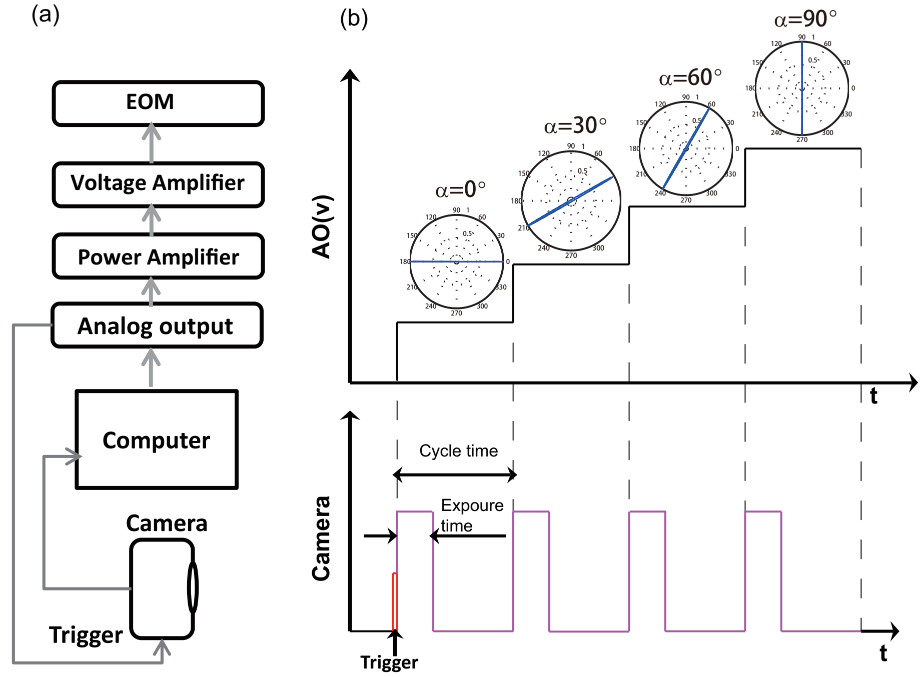

Figure 3.5: (a) Electronic instruments used for polarization control and image acquisition. (b) The working sequence of the analogue output and camera kinetic mode during a measurement.

3.1.4 Hardware

The data acquisition hardware is presented in Fig. 3.5(a). The command of the polarization control includes a high-speed analog output (AO) board (NI-USB-6351, National Instruments), which generates a control voltage in the ±2.5 V range, followed by a waveform amplifier (WA301, Aim & Thurlby Thander Instruments) that does not affect the voltage but boosts up the output power to reach the adequate value to control, and a high voltage amplifier (HVA-1M, Quantum Technology) which produces the high voltage (±200 V) that is applied to the EOM, in addition to a bias of 200 V. All these elements have a frequency response from DC to 1 MHz. Moreover, the AO board uses direct memory access, so that the calculated sequence of command voltages is stored in a buffer, and then delivered without communication to the computer. This ensures fast switching between successive linear polarization states.

In order to ensure the shortest acquisition time together with an accurate synchronization between polarization control and the camera, the timing of the camera acquisition sequence has been carefully optimized. When the exposure time, an integral multiple of

1/360 s, is set by the user to the camera, the minimum cycle time, which includes exposure time and delay to read the camera chip, is returned by the camera to the computer. The AO board is informed by the computer that the cycle time will be the duration of each polarization step, and determines the effective acquisition rate. When the acquisition is started by the user, as illustrated in Fig. 3.5(b) the camera acquisition is externally trigged by a start pulse generated by the AO board at the starting of each sequence. And then the camera and the AO board will respectively complete exposure and analogue voltage output sequence with no communication between each other. The cycles number is equivalent to the number of polarization steps. During one exposure sequence, the polarization resolved images are stored in the buffer of the camera, then are sent to the computer once after completing the whole stack of acquisition.

Our camera can operate down to cycle times of 30 ms, a value that is obtained for full definition operation and that can be reduced drastically using binning and/or a cropped sensor mode. Ultimately, by using three polarization angles, up to about ten full definition polarization stacks can be recorded by the system every second.

Note that in this case the number of photons recorded is higher that for a single-point scanning for which the pixel integration time did not exceed 100μs, In the present case the only limitation in intensity is fixed by photo-bleaching.

3.2 Calibrations

3.2.1 Polarization Calibration

Exciting path

Because of the prescence of the dichoric mirror placed between the microlens array and the pinholes array of the CSU, the polarization of the exciting light in the sample plane can be distorted (see Section 2.2.2). In order to ensure that any desired polarization state of the excitation can be properly delivered to the sample, the possible polarization distortions induced by the CSU have been investigated. Using the method as described in Appendix B.2, the results presenting the output polarization state for every input linear polarized light (Fig. 3.6) show that the output light polarization follows the same orientation than the input light polarization, but the CSU clearly induces a weak ellipticity. We found out that this polarization response could be perfectly reproduced numerically by modeling the CSU (including transmission through the microlens array and the dichroic

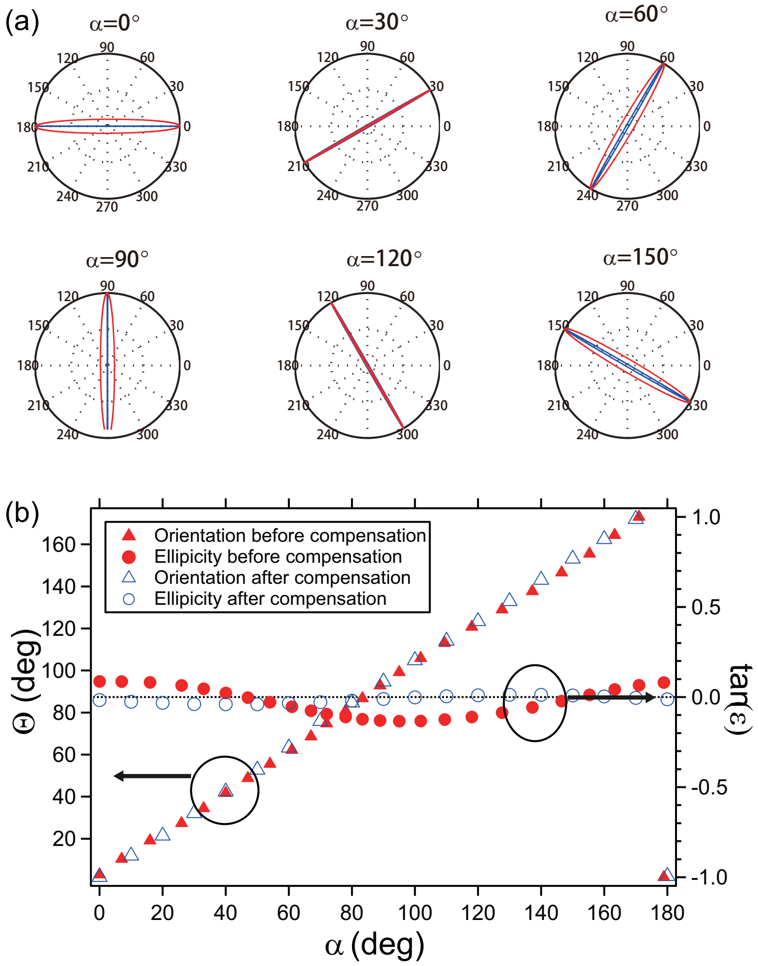

Figure 3.6: (a) A varying linear polarized input light with various orientations α, polarization states after passing CSU measured at sample plane, without compensation(red line) and with compensation(blue line). (b) Polarimetric analysis of the excitation light after being transmitted through the CSU, as a function of the input linear polarization angle α. Filled markers: before compensation. Empty markers: after compensation.

mirror, and reflections on the mirrors) as a single birefringent optical element having its fast axis oriented at 32.4° with respect to the horizontal axis X, a phase retardation of 12.3°, and no diattenuation.

In order to compensate these distortions, a Soleil Babinet compensator (SBC-VIS, Thorlabs) was finely oriented and tuned in retardation and introduced in the polarization control unit after the quarter waveplate. By repeating the measurements after compensation by the Soleil Babinet, the output light shows clearly (empty markers in Fig. 3.6)

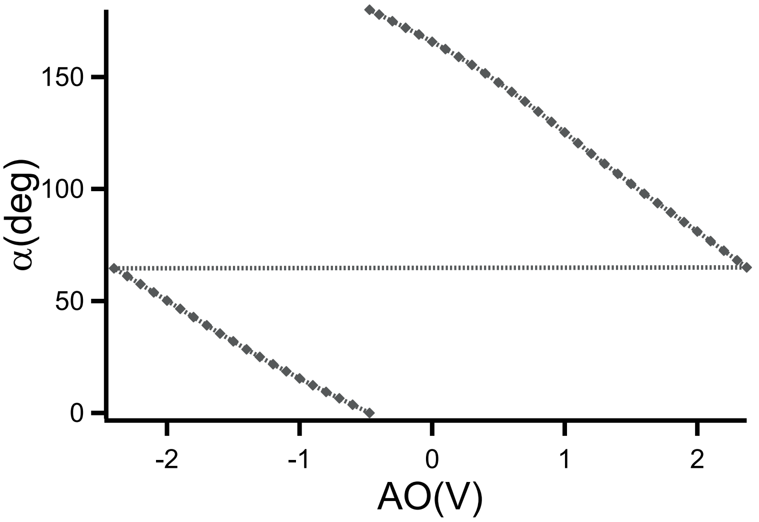

Figure 3.7: Calibration of the excitation polarization angle vs. AO voltage.

that the appropriate linear polarized light is now delivered to the objective lens.

After compensating distortions, the relationship between the polarization angle α and the AO voltage by the board (NI-USB-6351) was finely calibrated as illustrated in Fig. 3.7. The polarization angle α is proportional to the voltage V, therefore using interpolation this reference curve allows to set accurately any polarization angle to the system by setting the AO voltage.

Collection path

Similar investigations are needed in principle for the emission path. However, in this technique since fluorescence is only analyzed in terms of intensity, and not polarization, only diattenuation is a relevant parameter. A test was performed where white light from a tungsten lamp was attenuated, collimated, linearly polarized, introduced in place of the objective lens, sent into the CSU (i.e. reflected on the dichroic mirror and other deflections mirrors), spectrally filtered, and measured at the outport of the CUS with a optical power meter. By rotating the input polarization, we have recorded output intensity variations of a few percents only, as illustrated in Fig. 3.8, and the fluctuation bout 4% was considered as negligible.

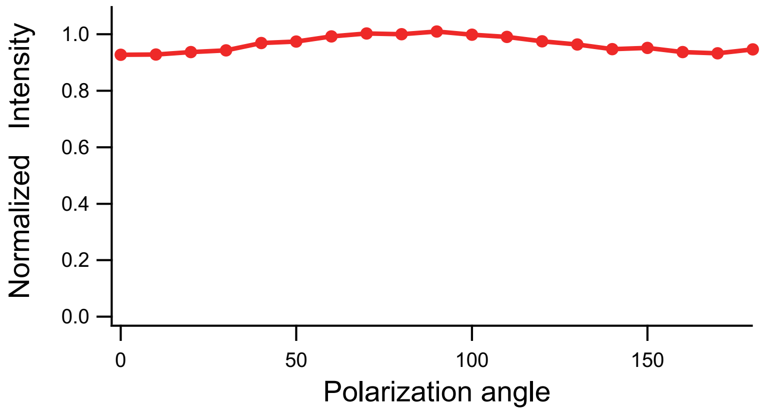

Figure 3.8: For linear polarized input light passing though the collection path, the measured intensity vs. polarization orientation from 0° to 180°

3.2.2 Camera calibration

In order to ensure precise quantitative data analysis, the response of the camera has been carefully investigated. First, the analysis of the camera response in dark conditions shows a systematic offset of 380 as returned by the camera, irrespectively of the gain and exposure time. This offset will be systematically subtracted from all data acquisitions, including calibrations below.

Linearity of camera response

In order to investigate the linearity of the camera response for given acquisition settings, fluorescence images of a 1-μM solution of Rhodamine 6G have been recorded under various excitation power, ranging between 50 μW and 7.5 mW, in order to generate a wide range of signal. At each test 100 fluorescence images were recorded and averaged to avoid fluctuations. For every condition, several regions of interest of 10×10 pixels have been selected, over which the response has been averaged. This analysis has been carried out for various camera gain settings, ranging between 100 and 1000. As it clearly appears in Fig. 3.9, we have observed a systematic threshold value of a measured signal (as encoded by the camera) of 6,000, above which a clear saturation effect appears. Note that since this threshold does not depends on the excitation power, it clearly indicates that the source of the saturation is not a saturation of fluorescence itself, but is due to the camera encoding. Below this threshold, the linear relationship of recorded signal vs. the excitation power is clear, which guarantees that the measurements can be processed in a quantitative way.

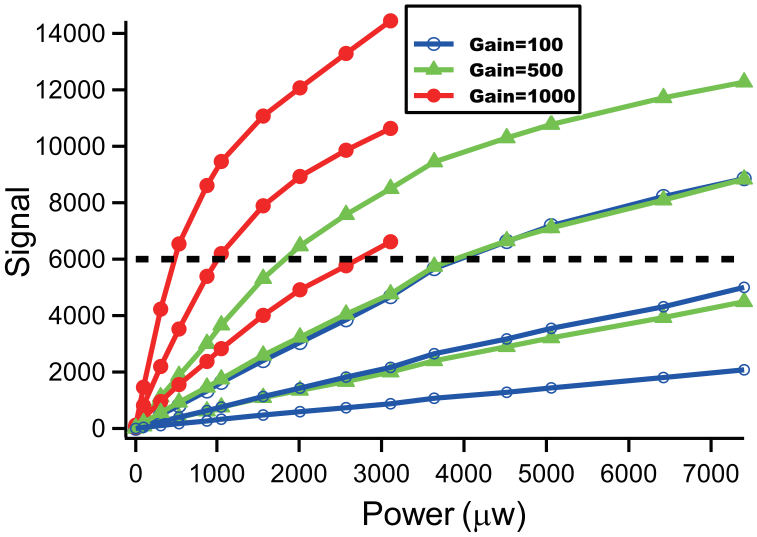

Figure 3.9: Signal returned by the camera vs. excitation light power for different area of the sample (connected data points) and different gain values. Response is linear below signal value of $6,000$.

Camera noise analysis

The noise that affects the signal returned by the camera has been analyzed in details since EMCCD differs from pure photon counters. Using, as above, a solution as a fluorescent sample, various measurement conditions of exposure time and gain have been tested. For each case, 100 fluorescence images have been recorded, allowing to analyze systematically the standard deviation σ_I as a function of the mean value $\langle I \rangle$ of the returned signal. A global analysis performed for many configurations shows that σ_I depends on the mean signal according to $\sigma_I = \kappa_g \sqrt{\langle I \rangle}$, as illustrated in Fig. 3.10a for the case $g = 600$. The factor κ_g was found to be only dependent on the gain g, although $\langle I \rangle$ depends both on gain and exposure time. The dependence of κ_g versus g is plotted in Fig. 3.10b. By using polynomial fitting method, the dependence of κ_g upon g could be written as:

$$\kappa_g = ag^2 + bg + c \tag{3.2}$$

with $a = 1.32 \times 10^{-6}$, $b = 1.89 \times 10^{-4}$, $c = 0.7151$. The effect of the camera noise on the precision of the technique will be discussed in Section 3.2.4.

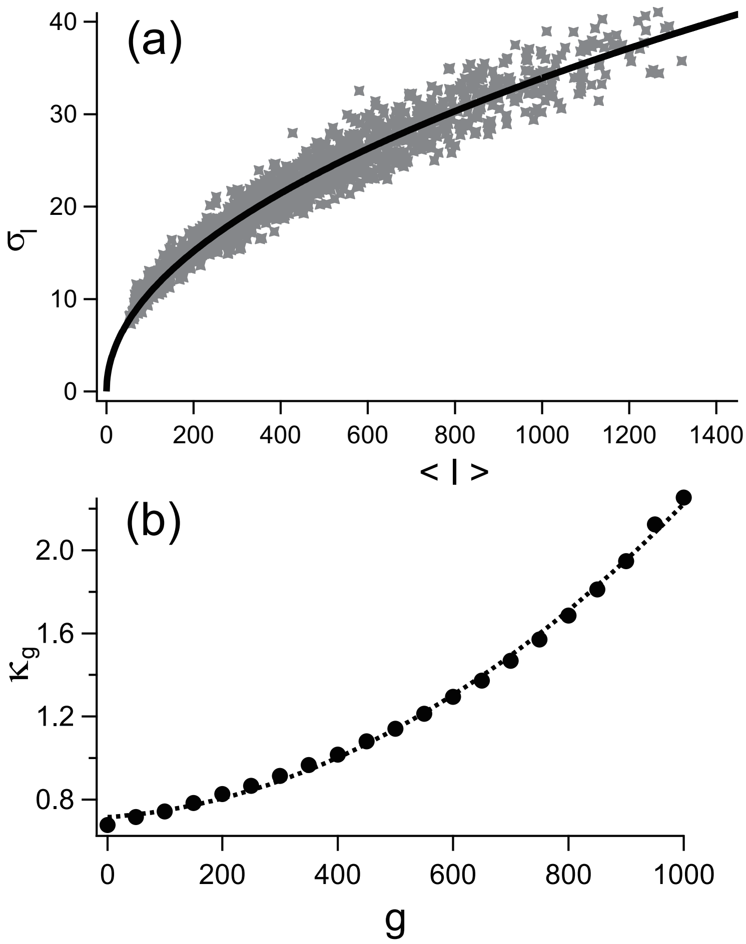

Figure 3.10: Camera noise analysis. (a) Relationship between the standard deviation σ_I and the mean value $\langle I \rangle$ for the case $g = 600$. Square markers: data, black line: best fit using relationship $\sigma_I = \kappa_g \sqrt{\langle I \rangle}$, with here $\kappa_g = 1.3$. (b) Dependence on the noise factor κ_g as the function of gain g.

3.2.3 Data processing

As in the previous setup, the same method based on the calculated relationship between (ρ, ψ) and the fourier series coefficient (A, B) of the polarization-resolved intensity curve is used to retrieve the ρ and ψ values from the fluorescence images recorded by the camera. In this setup, thanks to the compensation with the Soleil Babinet compensator, the residual polarization distortion in the exciting path is reduced to almost zero and the fluorescence intensity detection efficiency in the collection path is independent on the emitted polarization. Therefore, there is no need to introduce considerations about

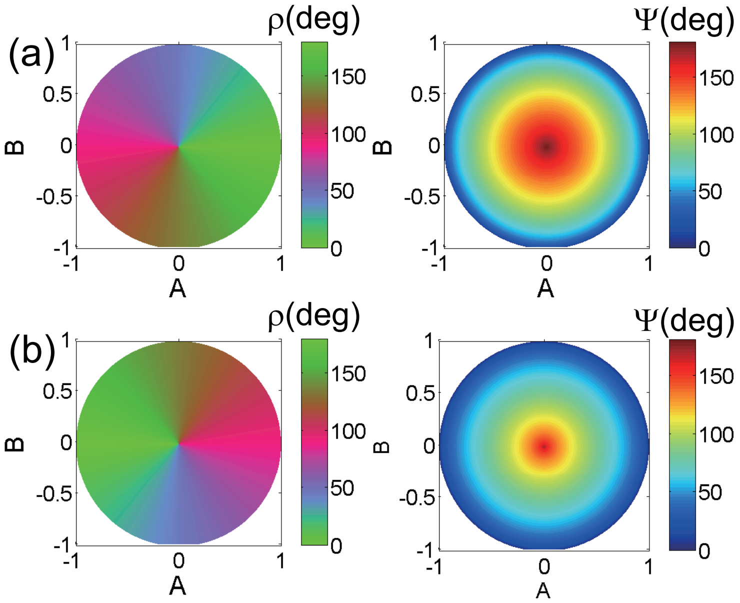

Figure 3.11: Reference maps for data processing. Simulated colormaps illustrating the unambiguous relationship between the coefficients (A, B) (coordinates) and the set(ρ, ψ) (color scale, angles are in degrees). (a) for the di-8-ANEPPQ lipid probe, cone model; (b) for the DiIC18 lipid probe, pancake-like model.

distortion corrections in the calculation of the relation between (ρ, ψ) and (A, B). The resulting disks map for the cone model and the "pancake" model are respectively given in Fig. 3.11(a)(b), which reproduce Fig 2.4 (a) and (b) without distortions.

In practice, pixels of interest are selected by regions defined manually by the operator and on the basis on their total fluorescence intensity $\sum_k I(\alpha_k)$. This allows to reject systematically image areas where the low signal (below 300) compromises the precision of the method [13], as previously done in confocal microscopy (see Section 2.3).

Similarly as we did in the previous setup, the validity of the retrieved set (ρ, ψ) is assessed by calculating the normalized chi-square given by eq. 2.16. Compared to the previous setup, the difference is that the noise is not Poisson distributed anymore and depends on the camera gain, as detailed in Section 3.2.2. The variance of every data point σ_I^2 is therefore assumed to be $\kappa_g^2 I(\alpha_k)$. According to our experience with testing various samples, data with $\chi^2 < 1.5$ always showed a good agreement between measurement and theory.

Thanks to this fast data processing method, the whole data processing takes about 100 ms on a standard personal computer, which supplies the capability of realtime monitoring of ρ and ψ in dynamic samples (Note that the number of analyzed pixels is larger than in the previous setup sin the camera chip has 512 × 512 pixels).

3.2.4 Precision analysis

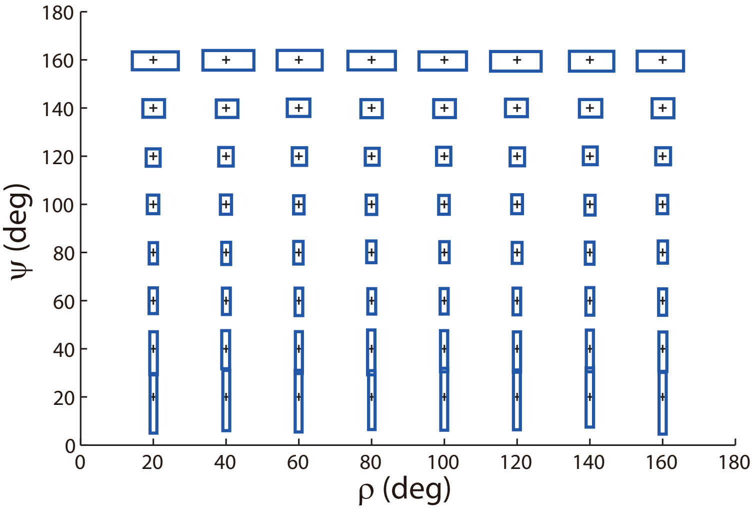

Figure 3.12: Precision analysis. For each set (ρ, ψ) (indicated by a cross, the rectangle represents error bars on ρ (rectangle width is twice the standard deviation on ρ) and ψ (rectangle height is twice the standard deviation on ψ). Total intensity $I_0 = 2000$ and camera gain $g = 500$.

In the setup based on laser scanning confocal microscopy, a Monte carlo simulation was performed to investigate the precision obtained for the determination of ρ and ψ . A similar simulation also is made for this setup, for each set (ρ, ψ), the theoretical response $I(\alpha_k)$ has been computed by theoretical expression for six angles α_k from $\alpha_1 = 0°$ to $\alpha_6 = 150°$ and scaled in order to simulate a total fluorescence signal $I_{\text{tot}} = 2000$, using a camera gain of $g = 500$. These values correspond to typical acquisition parameters. Compared to previous calculations detailed in Section 2.3.2 which used poisson distribution, a normally-distributed random numbers generater was used here.

The result are summarized in Fig. 3.12, where each nominal set (ρ, ψ) is represented as a cross. The rectangle quantifies the distribution of the retrieved values ρ and ψ. The center of the rectangle is the mean value, and its width (and height) is twice the standard deviation on ρ (and ψ, respectively). This results show an uncertainty on ψ

of about 5° for ψ ranging between 60° and 120°. This precision is slightly better for large ψ values. Because of the absence of distortion the uncertainty dose no depend on ρ. The uncertainty on ρ is in the range of the degree, except for large values of ψ for which orientation becomes meaningless. Simulations carried out for various I_{tot}, and not presented here, show that the obtained uncertainties on both ρ and ψ are simply scaled according to $1/\sqrt{I_{\text{tot}}}$, irrespectively on the number of angle steps. Therefore, increasing the exposure time, using smaller angle steps, or binning neighbor pixels, are appropriate ways to improve the precision. The analysis is based on the cone model. Although not presented here, comparable results have been obtained for the "pancake" model.

Note that camera gain provides another powerful way to increase the signal. However, the effect of gain on signal and noise is specific to the camera used, so a systematic noise measurement study needs to be done for each system.

3.3 Examples of measurements

3.3.1 Giant unilamellar vesicles labeled with DiIC_{18}

To verify the validity of our setup, as we have done for the confocal setup, giant unilamellar vesicles (GUVs) have been chosen as model system. The samples were prepared with the method described in Section C.1 and labeled by dye DiIC_{18} which is refereed by the "pancake" model (see Section 2.4.1).

The sample was probed by 30 polarization angles from $\alpha_1 = 0°$ $\alpha_{30} = 174°$ with space of 6°, Camera gain was set to g = 1000, exposure time was set to 33.3 ms, cycle time was 72 ms, so the whole image stack was acquired in about 2.5 s.

The total fluorescence image obtained on the equatorial plane of a GUV of diameter about 15μm is presented in Fig 3.13(a) after filtering out pixels with total signal below 500. As expected from a confocal system, the center of GUV appears dark, a signature of good sectioning capabilities. Fig 3.13(b) shows the data corresponding to point labeled as A in Fig 3.13(a), as well as the theoretical response corresponding to the retrieved parameters ρ and ψ. Note that these data are not affected by any photobleaching effect.

The data were processed with the method presented above. The obtained results about ρ and ψ are encoded with different color map and respectively illustrated in Fig 3.13(c) and (d) with rejecting distorted measurements by the χ^2 filter described above, which is calculated and presented in Fig. 3.13(e), with an experiential threshold of $\chi^2 < 1.5$.

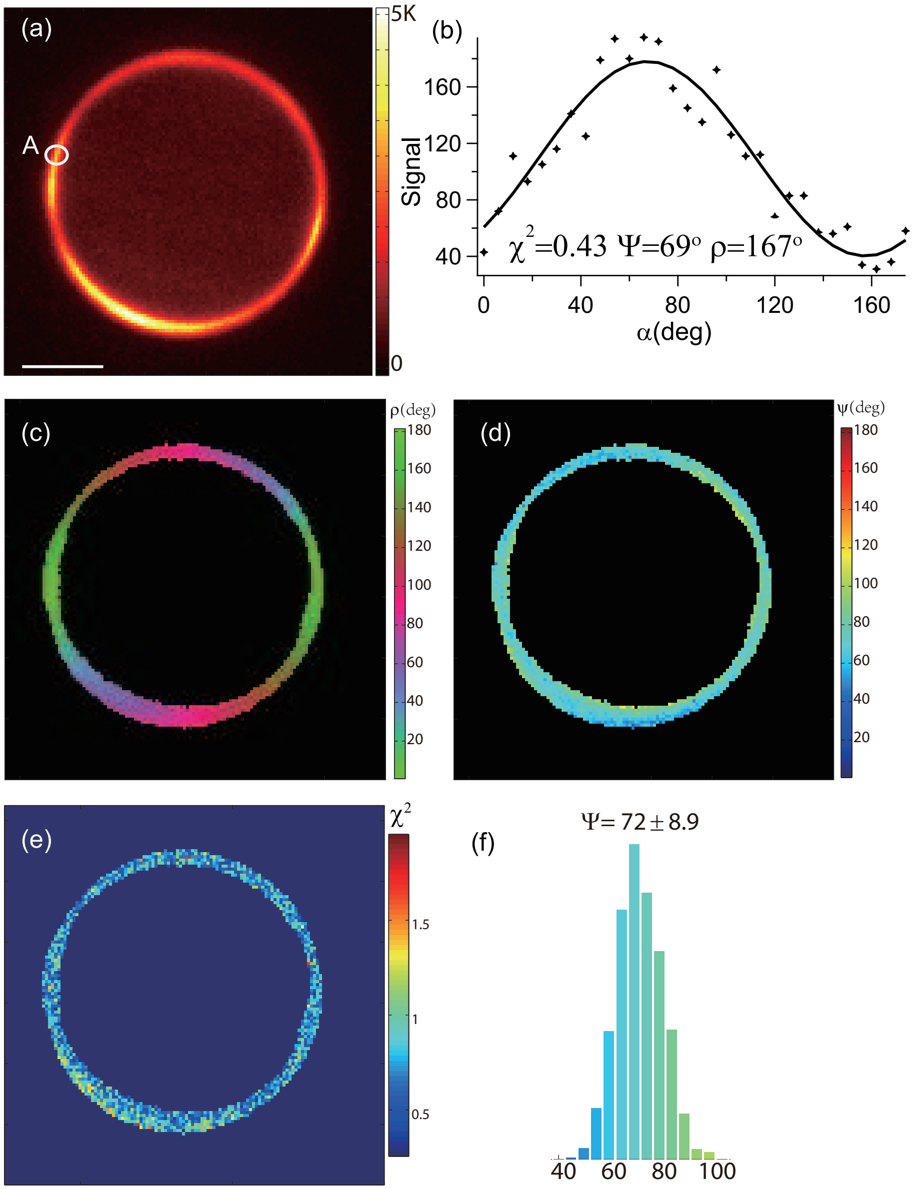

Figure 3.13: Validation experiments on giant unilamellar vesicles labeled with DiIC$_{18}$. (a) Fluorescence image (b) Measured polarimetric responses for point labeled with A in (a) and the theoretical value corresponding to the retrieved set of $(\rho = 167°, \psi = 69°)$. (c) Retrieved ρ-image. (d) ψ-image (e) χ^2-image. (f) Resulting histogram of ψ. Scale bar $5\mu m$

Such picture are displayed in real time to the user, with a frame rate of 0.4 fps. These results show clearly that the angle ρ is perpendicular to the membrane lipids, i.e., the fluorescent dipole lies on the membrane. As expected for this system, made of a unique molecular species, the value of the angle ψ is homogeneous over the membrane contour, showing remarkably that the technique addresses with the same efficiency all membrane orientations. The histogram in Fig. 3.13 shows the average value of ψ of 72° and standard deviation of 8.9°, which are in agreement with the results obtained by the previous setup (see Fig. 2.8).

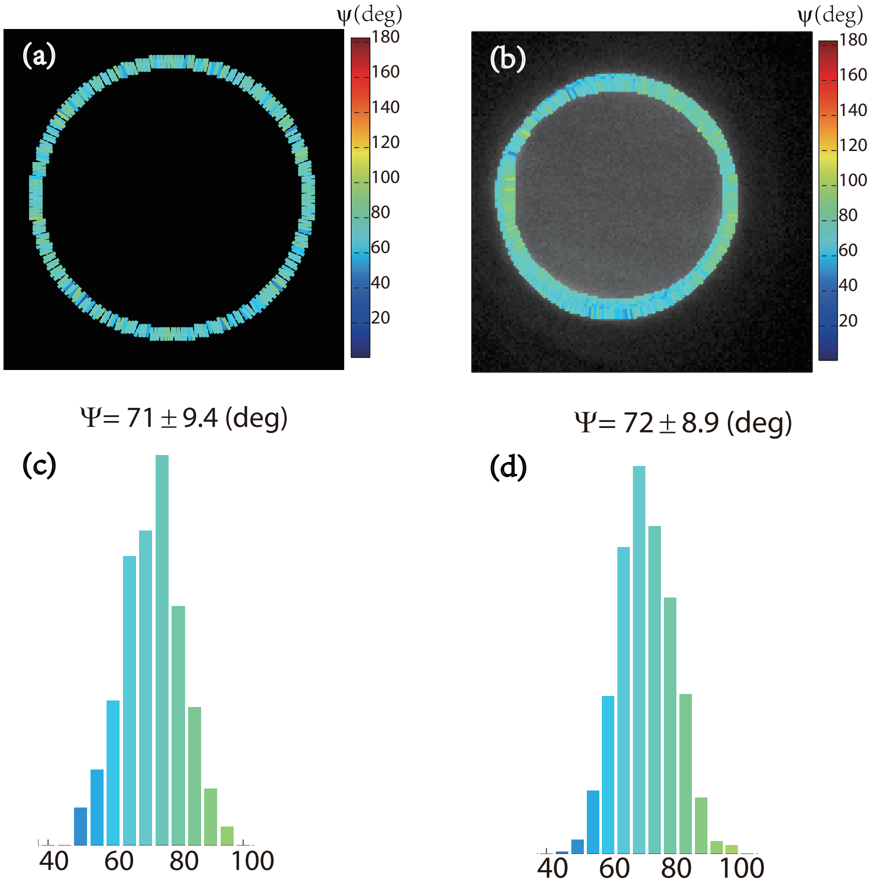

Figure 3.14: Composite image summarizing the results of the mean orientation ρ (indicated by an orientated stick) and the angular aperture ψ (ranging from 0° to 180° , encoded as a color) among (a) the numerical simulation based on an artificial GUV , (b) the previous measurement on confocal setup and On the bottom (c)(d) are corresponding histogram.

In order to validate the results obtained by this setup, a numerical simulation has been run where an artificial GUV with a unique $\psi(= 72^\circ)$ value over the contour was generated by Matlab and based on the artificial GUV a data set of polarization images stack was generated assuming the same measurement conditions as taken in the test presented above(angle setps, total intensity, camera gain, etc.). The results of retrieved ρ and ψ for artificial GUV and experiment measurement are respectively illustrated in Fig. 3.14(a)and (b), which are composite images built by superimposing a gray-scale image of total fluorescence and colored sticks for every processed pixel. Each stick is oriented with the retrieved angle ρ, while its color gives the value of ψ. The histograms in Fig. 3.14(c)(d) show the comparable standard deviations of about 9° for these two cases, which means that the distribution of ψ values is only due to the precision of the method.

GUVs Labeled by di-8-ANEPPQ

The test on GUVs presented above is made for the "pancake" model where the fluorophore lies on the membrane surface. In this section a test is also made on GUVs with labeled by dye di-8-ANEPPQ which is refereed by the "cone" model (see Secction 2.4.2).

In the measurement, the sample was probed by less polarization angles of 18 from $\alpha_1 = 0^\circ$ to $\alpha_{18} = 170^\circ$ with space of 10°. Camera gain was set to $g = 1000$, exposure time was set to 33.3 ms, cycle time was 72 ms, so the whole image stack was acquired in about 1.3 s. In order to boost up the signal, pixel response were summed with the eight direct neighbors. An example of total fluorescence image obtained on the equatorial plane of a GUV of diameter 25 μm is shown in Fig. 3.15(a). For the point labeled as A, the measured polarimetric response and the corresponding theoretical value are presented in Fig. 3.15(b). Note that these data are not affected by any photobleaching effect.

The data were processed using the cone model, the results are illustrated by a composite image using a stick representation: the sticks are oriented with the retrieved value of ρ and their color indicates the value of ψ, as shown in Fig. 3.15(c). This representation permits to show ρ and ψ in a same image. A homogeneous distribution of ψ is retrieved all over the membrane. The average value of ψ shown in in Fig. 3.15(d) is consistent with the measurement obtained using fluorescence anisotropy[27] and confocal setup (see Section 2.4.2). The standard deviation on ψ is 15°, a value which can be attributed to the low signal (below 200 in one pixel due to less steps) of the measurement.

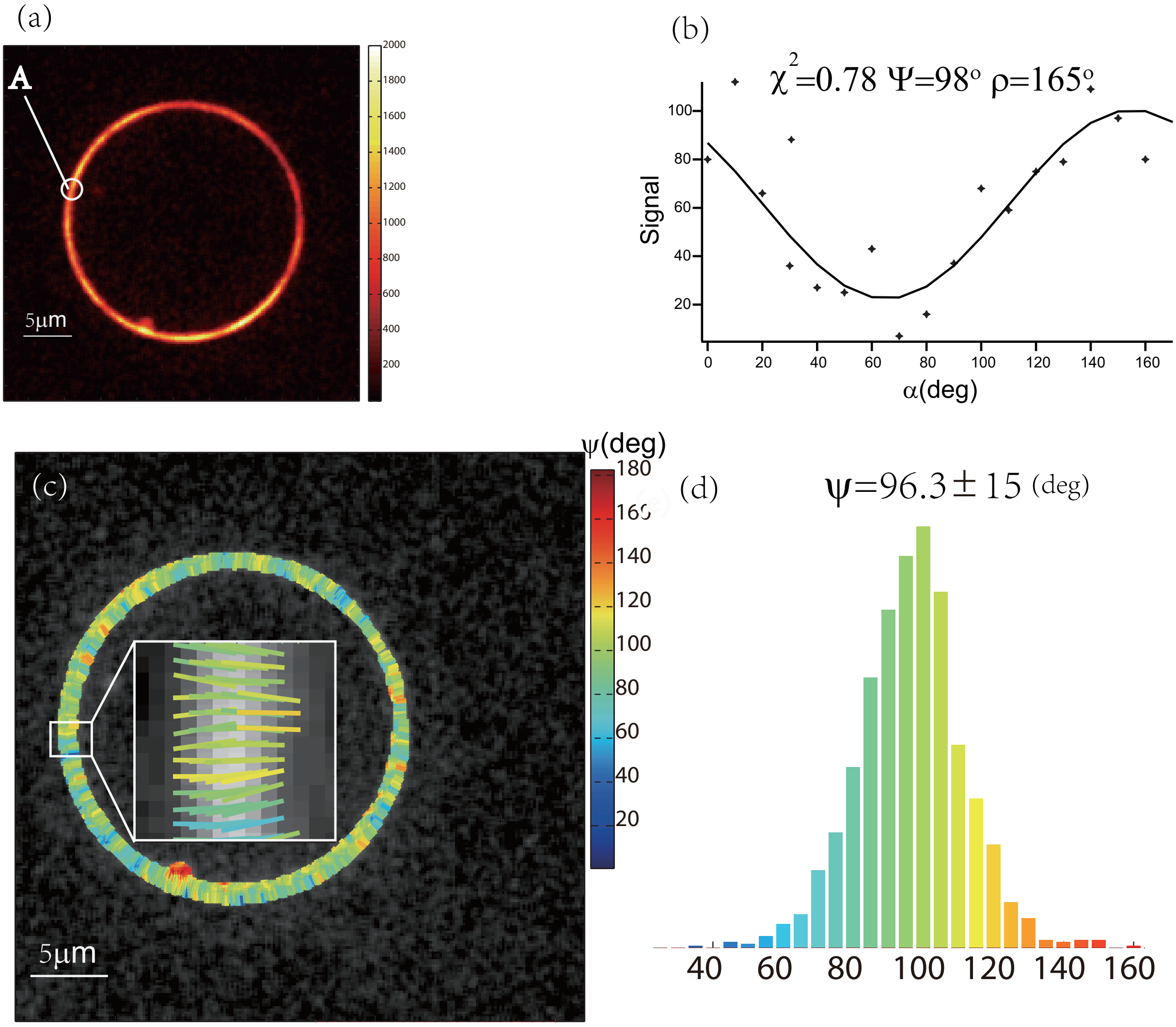

Figure 3.15: Validation experiments on giant unilamellar vesicles labeled with di-8-ANEPPQ.(a) Fluorescence image (b) Measured polarimetric responses for point labeled with A in (a) and the theoretical value corresponding to the retrieved set of ($\rho = 165°, \psi = 98°$). (c)Composite image summarizes the mean orientation ρ and the angular aperture ψ. (d) the resulting histogram.

3.3.2 Cos-7 cells

We use here COS-7 cells that have been labeled by di-8-ANEPPQ, and the samples were prepared following the protocol detailed in Appendix C.2.

The measurement has been carried on at the room temperature with the same acquisi-

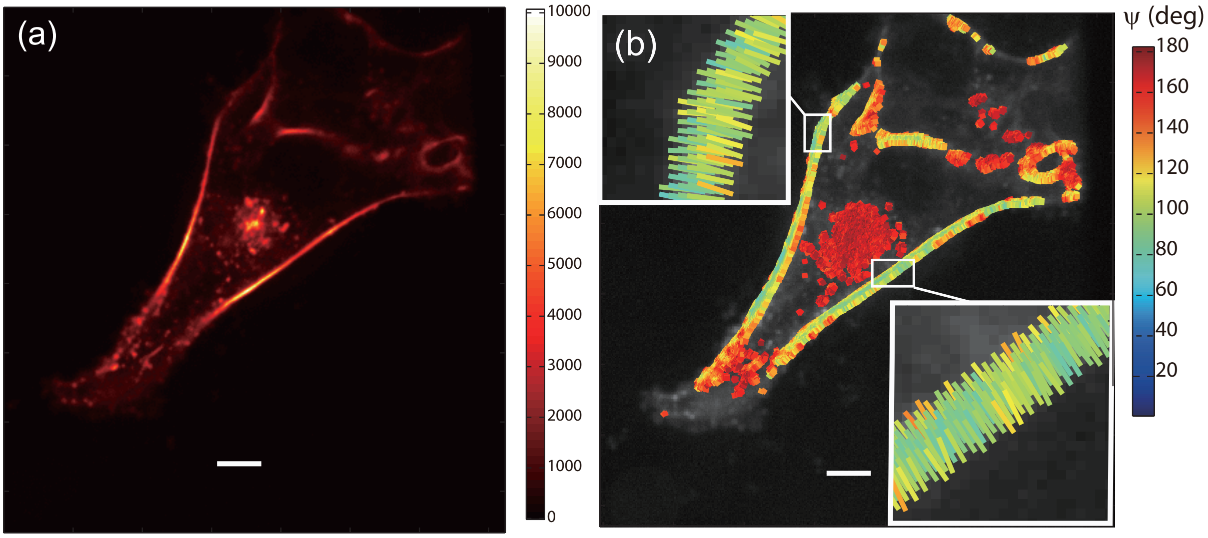

Figure 3.16: Experimental results on COS-7 cells labeled with di-8-ANEPPQ.(a) Fluorescence image. The color scale indicates the total intensity $\sum_k I(\alpha_k)$. (b) Composite image summarizes the mean orientation ρ (indicated by an orientated stick) and the angular aperture ψ (ranging from 0° to 180° , encoded as a color). Insets are close-ups. Scale bars are $5\mu m$.

tion parameters that were used on measurements of GUVs labeled with DiIC$_{18}$, the sample was probed by 30 polarization angles from $\alpha_1 = 0°$ $\alpha_{30} = 174°$ with space of 6°, Camera gain was set to g = 1000, exposure time was set to 33.3 ms, cycle time was 72 ms, so the whole image stack was acquired in about 2.5 s. These setting are slightly different from GUVs measurements to accommodate to the lower signal. No pixel summation was used here. The focus was set in an intermediate plane in order to ensure that the fluorescent molecules lie in average in the sample plane. An example of measurement for a typical cell is shown in Fig 3.16. Here again, dipoles are clearly perpendicular to the membrane. Similarly to what was observed with the setup using conventional laser-scanning confocal microscopy, the values of ψ recorded on the membrane allow to separate clearly regions of high order ($\psi \approx 80°$) and low order ($\psi \approx 150°$) along the contour which can be explained by possible sub-resolution morphological features [13]. A more homogeneous response is obtained in the less ordered cytoplasm regions, where $\psi \approx 180°$ indicates an isotropic angular distribution of fluorophores.

3.4 Acquisition rate

These examples show that our technique allows retrieving the values of ρ and ψ at the rate of 0.4 fps, a value which is still lower than the acquisition rate of 10 fps reachable by our setup (see Section 3.1.4). This is mainly due to the high precision that was desired for ρ and ψ, together with the relatively low brightness of the fluorophores that we have used in this work. These two conditions impose indeed a high amount of polarization angles to ensure a sufficiently high level of signal.

More generally, for a given setup and sample, strategies to improve the acquisition rate include: (i) reducing the number of polarization angles or the exposure time, which will also reduce the precision of the retrieved parameters, as discussed in Section 3.2.4, (ii) reducing the number of pixel to be measured, by means of pixel binning or sensor cropping, which does not affect the precision. In practice, it appears that the acquisition rate is much more limited by the fluorophore brightness and camera signal to noise ratio than by the polarization switching or CSU velocity.

3.5 Conclusion

In this chapter we have presented the implementation of the angle resolved LD in a parallel confocal system. The polarization and camera calibration has been detailed and their corresponding effects in data processing have been presented. We have presented the measurements in GUVs and cells in this setup, and the GUVs results have been compared with the results obtained by the previous confocal setup. This setup has been proven that it considerably improves the acquisition rate, therefore it allows monitoring the molecular angular distribution in more dynamic samples while keeping a good axial resolution.

Chapter 4

Determining 3D orientation distribution

As discussed previously, out-of-plane dipoles contribute to the signal of fluorescence of ARLD. However, their our-of-plane angle cannot be resolved. In this chapter, we propose a method to probe the 3D orientation.

4.1 Measuring of 3D orientation: the case of a single dipole

Although the measurement of the molecular orientation in the plane perpendicular to the optical axis could be accomplished in a number of ways, determination of the 3D orientation of a single dipole is considerably more challenging. There are some schemes developed to determine the 3D orientation of a single dipole, which will be reviewed briefly in this section. Here we suppose that the fluorescence dipole has been excited by a given 3D polarization (it will be specified later how to produce it) and we want to retrieve its 3D orientation.

All the schemes described here are based on the fact that a dipole radiation pattern depends on its orientation, and can be collected by a high numerical aperture objective. Analyzing the defocusing image behind an objective is one of schemes to determine the out-of-plane orientation of a single molecule [42, 43]. As presented in Fig. 4.1, for dipoles with different out-of-plane orientation the defocusing images experience different shapes with varied defocusing distance. This method is easy to implement by use of a conven-

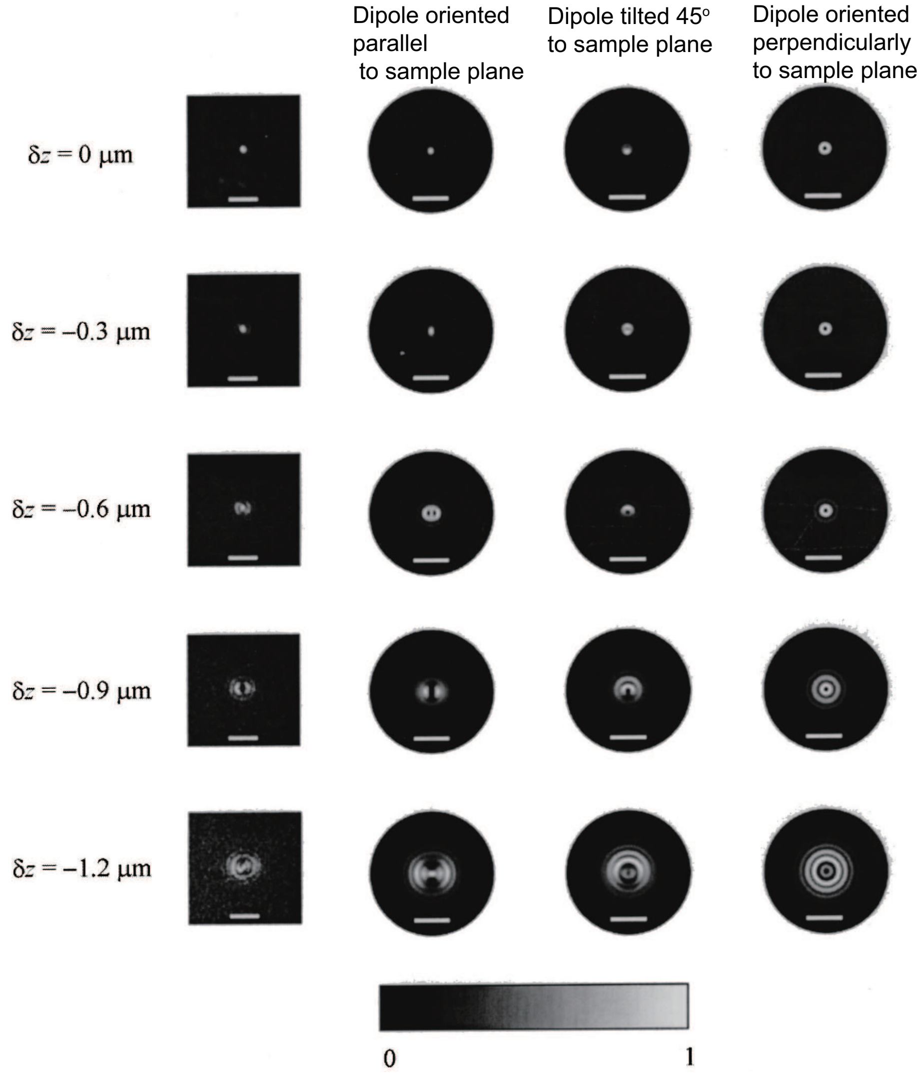

Figure 4.1: Comparison of, left to right, measured images of a single molecule and theoretically calculated images for three different dipole orientations as marked above and for the defocusing values indicated at the left (relative to the image plane). The scale bars: 100 mm. The correspondence between intensity and gray value is shown by the gray scale at the bottom (all intensity images are normalized to 1). From [42].

tional CCD-imaging in an epi-fluorescence microscope with laser wide-field illumination. However this techniques requires the collection of a considerable number of photons over a full image, as well as complex and time-consuming image analysis.

Recently, the scheme based on analyzing the polarization state of the field at the back

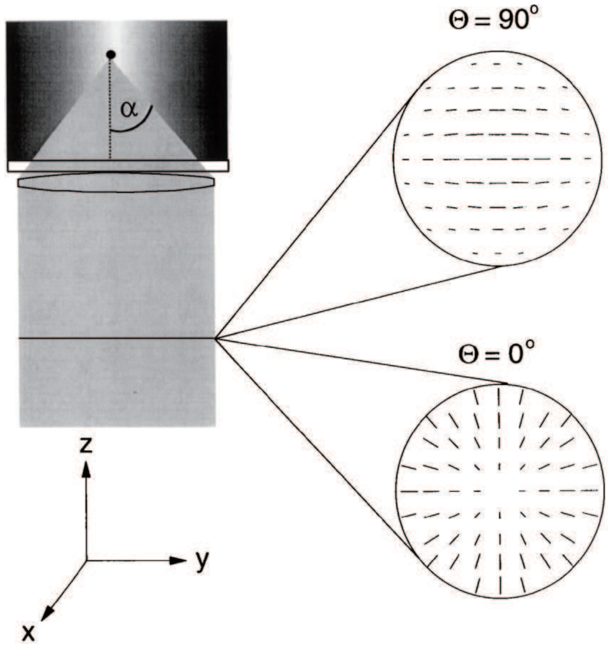

Figure 4.2: The polarization states of emission field respectively for a dipole oriented along y axis ($\Theta = 90$) and z axis ($\Theta = 0$). From [44].

focal plane of an objective has been proposed [44]. It is assumed that a single molecule is located at the focus point on the optical axis of the collection objective. If the fluorescent dipole is oriented in the sample plane perpendicular to the optical axis of the objective, then the spatial distribution of the polarization in the back-focal plane is nearly uniform and keeps the same orientation as the one of the dipole, as illustrated in Fig. 4.2. If the dipole lies along the optical axis of the objective, the polarization direction in the back-focal plane is radially distributed, so that the image beam appears as not polarized. Therefore the in-plane orientation of a single radiating dipole could be determined by the orientation of the polarization in the back focal plane. and out-of-plane orientation could be monitored by analyzing the change of polar orientation within the back-focal plane.

Besides analyzing the polarization state of the emission field behind a high NA objective, another method proposed is based on direct comparison of the emission intensity from the in-plane and the out-of-plane components of a single dipole [45, 46, 47]. For the in-plane component measurements, the emission is allowed to be detected by a low NA objective combined with a detector. For the out-of -plane component (Z component) of the dipole, in this technique a $0|\pi$ phase mask or a circular beam stop is employed to break the symmetry of the emission pattern as presented in Fig. 4.3. This will be more

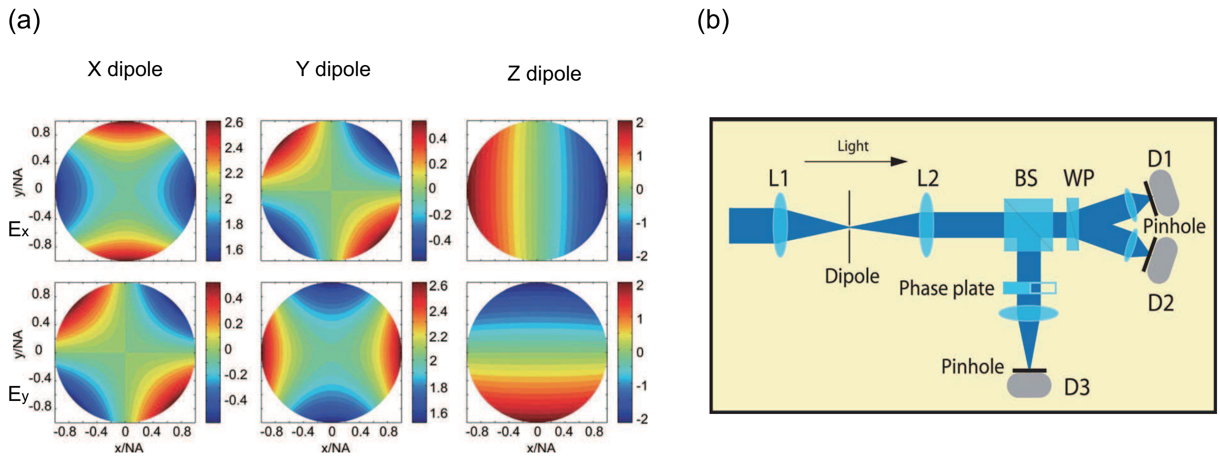

Figure 4.3: (a) The emission field in the back-focal plane of a high NA objective for dipoles respectively oriented along X, Y and Z (propagation direction) , E_x (top), E_y (bottom). (b) Proposed optical setup for determination of the full 3D orientation of an electric radiating dipole. From [45].

detailed in Section 4.2.3 (see Fig. 4.13).

The schemes presented above are designed to determine the 3D orientation of a single molecule. However this case is not likely to happen in biology where the sample is usually complex and is labeled by a lot of fluorophores in the observation volume. The methods described above do not work any more even for two dipoles, for which the radiation pattern is expected to be a lot more complex.

More generally, for an ensemble of dipole, a distribution function need to be considered as a cone model introduced previously and shown in Fig. 2.1, where ρ and η respectively indicate the in-plane and the out-of-plane mean orientation, and ψ represents the cone aperture which describes the order of the molecular orientation distribution. When the molecular is highly ordered, the cone aperture ψ is small, oppositely when the molecular is disordered the cone aperture is big.

Contrary to a single dipole, and additional parameter has to be resolved (ψ). Therefore for a cone, the out-of-plane mean orientation η and cone aperture ψ cannot be resolved simultaneously by the techniques mentioned above (polarization analyzing of the field at the back-focal plane of a high numerical aperture (NA) objective, or the ratio between emission intensities from in-plane components and out-of-plane components). We illustrate this issue in Fig. 4.5 where we calculate the intensity ratio between the out-of-plane component and in-plane component ($\frac{\mathrm{I_Z}}{\mathrm{I_X+I_Y}}$) for cones with different set of (η, ψ). For a

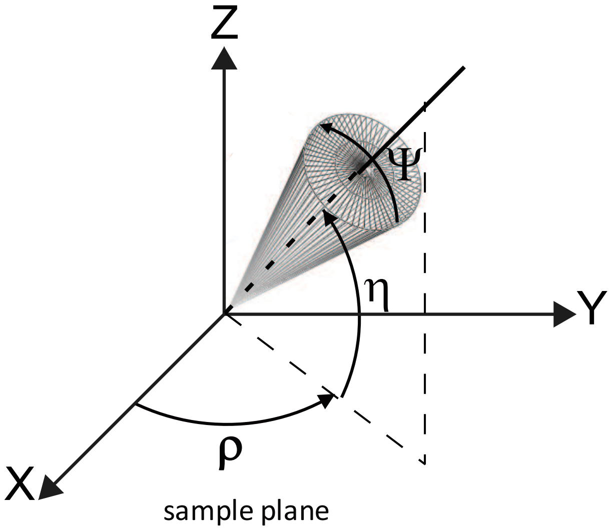

Figure 4.4: the 3D model of a cone in XYZ coordinate, where Z axis is parallel to the optical axis. In the 3D model, the ρ indicates the projection direction in XY plane of mean orientation of the cone, the η indicate the mean orientation of the cone off the XY plane and ψ indicates the cone aperture.

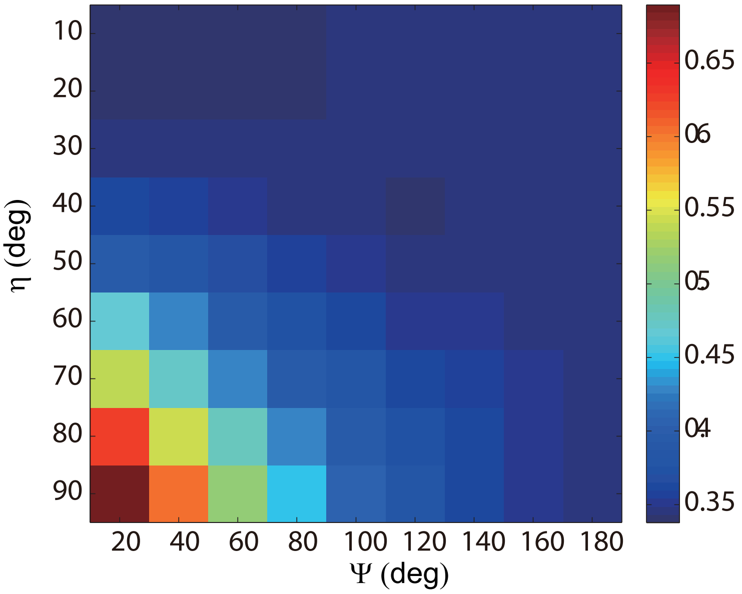

Figure 4.5: the map of the intensity ratio between the out-of-plane component I_Z and the in-plane component $I_X + I_Y$ for every set of (η, ψ).

given ψ this ratio increases with η increasing , and the ratio reduces with a bigger ψ for a given η . It is clear from Fig. 4.5 the η and ψ values can not be determined unambiguously by the ratio. For example, the cones $(\eta = 60°, \psi = 40°)$ and $(\eta = 80°, \psi = 80°)$ give similar ratios.

In the following, we propose a method based on the out-of-plane excitation polarization tuning to simultaneously probe the 3D orientation and the order information ψ for a cone exhibiting any kind of orientation in 3D.

4.2 3D excitation and detection for a distribution of dipoles

4.2.1 About the need of a full calculation

In the method developed in Chapter 2 and 3, we made several assumptions

1. we assumed that the probed dipoles (i.e. in the confocal volume) experience the same exciting field. Fig 4.6(a) (which calculation will be detailed in the next section) shows the 3D distribution of exciting field when focusing linearly polarized light. It appears clearly that the field polarization is nearly homogeneous in the focal volume, which justifies our assumption.

2. we assumed that the detection efficiency did not depend on the in-plane orientation of the dipoles. This was justified by the fact that the detection was performed perpendicularly to the dipole plane, always showing to the objective lens the same portion of emission intensity pattern.

With the aim to probe the out-of-plane dipoles, the focusing of unusual polarizations to reach excitation fields oriented in 3D appears to be necessary. For instance, focusing radial polarization patterns allows to create fields along the axial direction and could address the out-of-plane dipoles. However, as appears clearly in Fig. 4.6(b) (which calculation is detailed in the next section) the field distribution in volume is no more homogenous, so that our first assumption is no more valid. Moreover, the detection efficiency of a dipole will depend on its out-of-plane angle, so that our second assumption is also not valid neither.

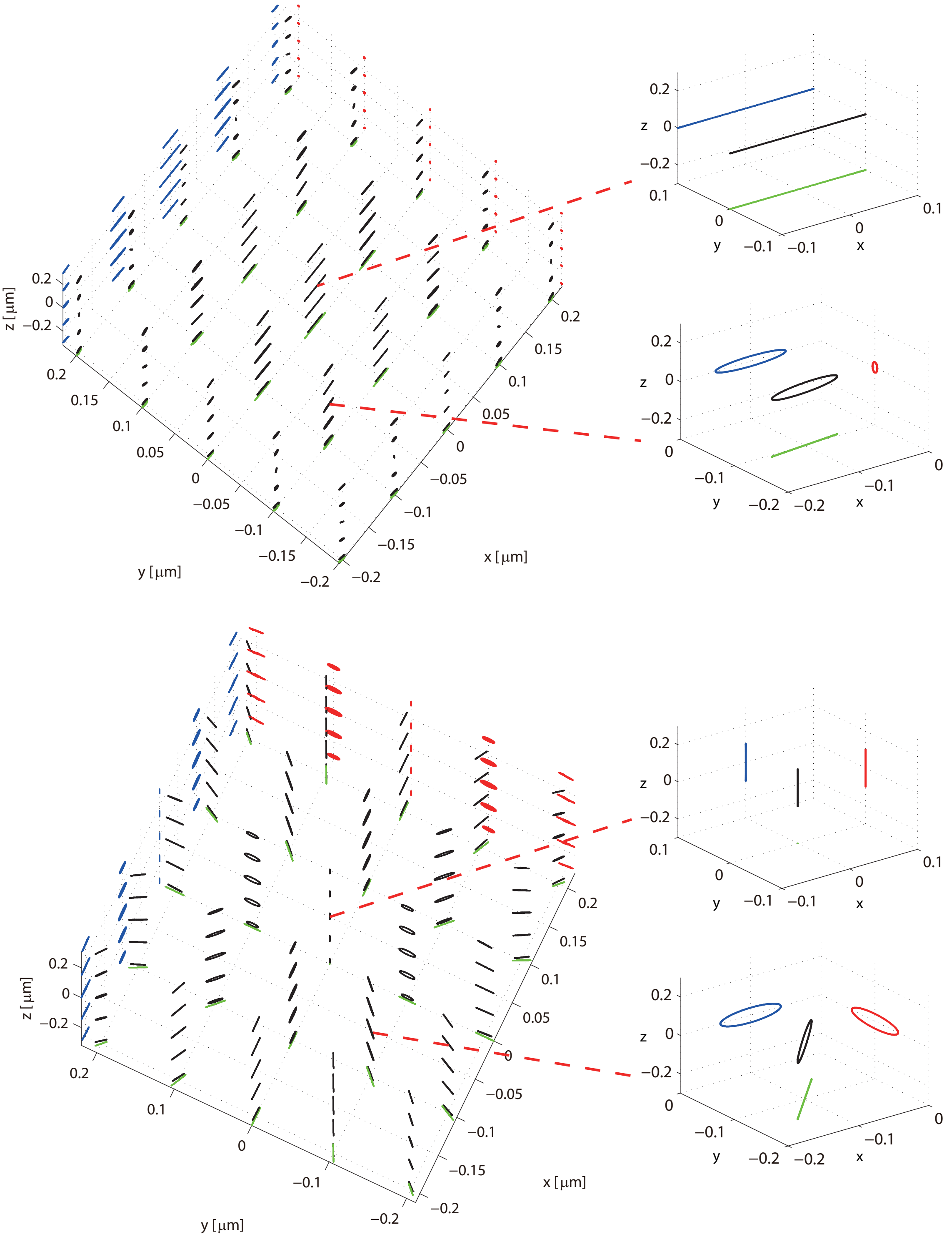

Figure 4.6: Polarization state in the whole focusing volume and its projection (red: projections superimposed on YZ plane, green: projections superimposed on XY plane,blue: projections superimposed on XZ plane) for (a) a X direction linearly polarized, (b) a radially polarized input light, the.

Therefore, instead of using the equation

$$I = \iint \overline{|\vec{\mu}(\theta,\phi,\rho,\eta)\cdot\vec{E}|}^2 f(\theta,\phi)J(\theta,\phi,\rho,\eta)\sin\theta\mathrm{d}\theta\mathrm{d}\phi \tag{4.1}$$

the emitted intensity needs to be written using a more general expression

$$I = \iiint \overline{|\vec{\mu}(\theta,\phi,\rho,\eta,\vec{r})\cdot\vec{E}(\vec{r})|}^2 |E_{em}(\theta,\phi,\rho,\eta,\vec{r})|^2 f(\theta,\phi)\sin\theta\mathrm{d}\theta\mathrm{d}\phi\mathrm{d}r \tag{4.2}$$

which is a full volume integral, where the dependence on space of $\vec{E}(\vec{r})$ and $E_{em}(\theta,\phi,\rho,\eta,\vec{r})$ are clearly taken into account. This justifies the full 3D modeling which will be detailed in the following.

In the following part, we will first address the issue of the calculation of $\vec{E}$ and then the calculation of $\vec{E}_{em}$.

4.2.2 The electric field in the focus volume of a high NA objective

The complex field of the collimated gaussian beam before passing a high NA objective can be written: .

$$\vec{E}(x,y,z) = \vec{E}_0(x,y,z)\exp(-\frac{x^2+y^2}{\sigma^2})\exp(ik_0z) \tag{4.3}$$

Here σ indicates the half width when intensity decreases to the $1/e$ of the maximum intensity at the center, $k_0 = 2\pi/\lambda$ is the wavevector and $\vec{E}_0(x,y,z)$ is the incident field amplitude.

Here, we define a parameter γ to characterize the filling ratio of the input beam relative to r_0, the radius of the pupil of the objective lens (Fig. 4.7):

$$\gamma = \frac{r_0}{\sigma} \tag{4.4}$$

In cylindrical coordinates, the incident field on the objective lens can be written as:

$$\vec{E}(\theta,\varphi,z) = \vec{E}_0(\theta,\varphi)\exp\left[-(\frac{n\gamma\sin\theta)}{\mathrm{NA}})^2\right]\exp(ik_0z) \tag{4.5}$$

with

$$NA = n\sin\theta_{max}$$

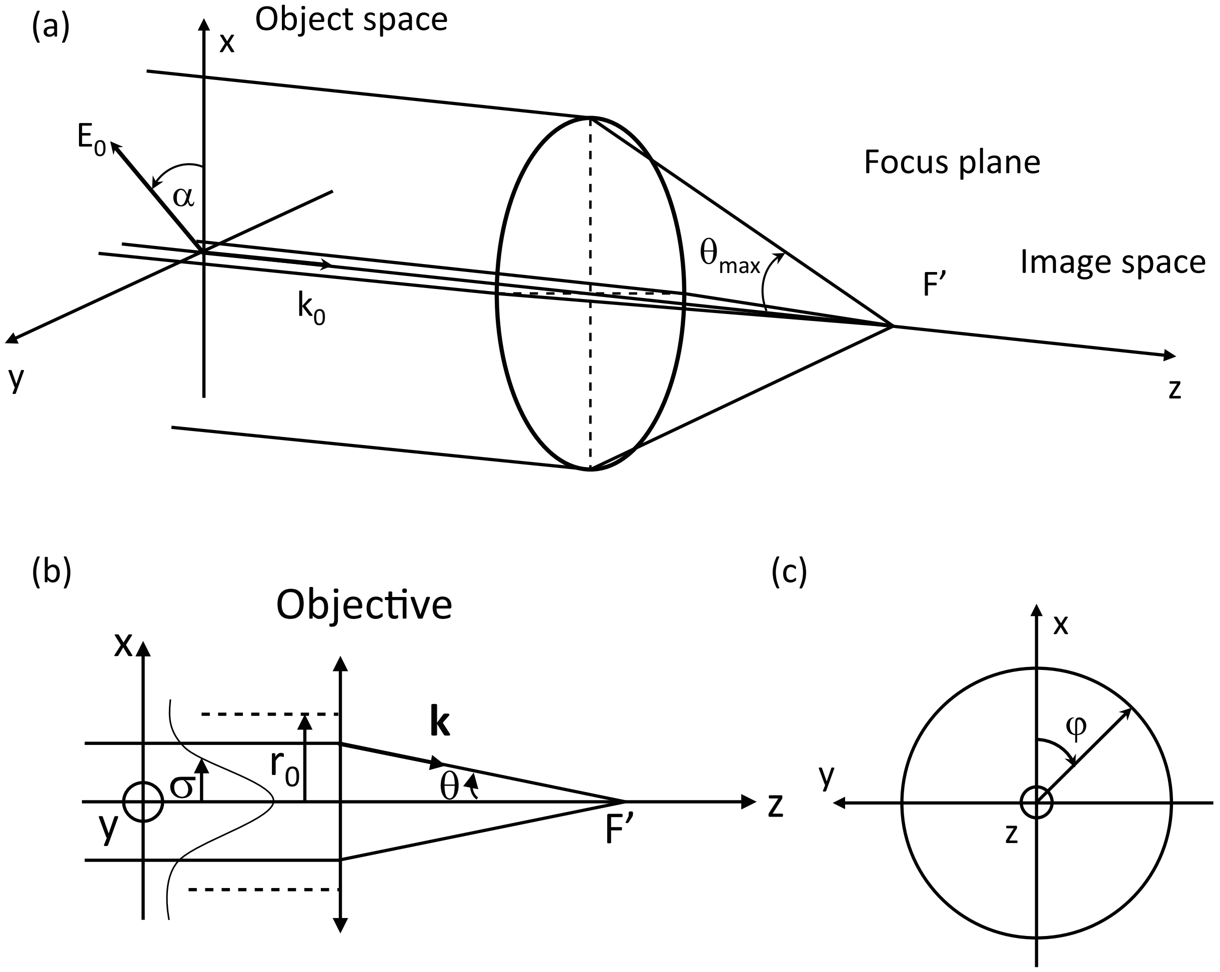

Figure 4.7: The focusing by a high NA objective. (a) The polarization angle of the input Gaussian beam with respect the X axis is indicated by α, k_0 is the wavevector, the optical axis is along the Z direction, F' is the focusing point in image space, the θ_{max} is the maximum focusing angle. (b) σ indicates the half width when the field intensity reduces to $1/e$, r_0 is the radius of the entrance pupil, θ is the focusing angle for wavevector k. (c) φ is the angle relative to X of the projection of the wavevector k in the XY plane.

Note that through this whole section the angle θ refers here to spherical coordinates, a definition that is different from the orientation in Chapter 2.

Due to the high NA of the objective the paraxial approximation is not valid anymore, we must decompose the input field into planewaves (see [48]). In the image space of the objective, the field out of the objective aperture is the superposition of plane waves taken by wavevector $\vec{k}$, and $\vec{E}_k$ denotes the electric field taken by $\vec{k}$:

$$\vec{k}(\theta,\varphi) = \frac{2\pi n}{\lambda}\begin{pmatrix} \sin\theta\cos\varphi \\ \sin\theta\sin\varphi \\ \cos\theta \end{pmatrix} \tag{4.6}$$

$$\vec{E}_k(\alpha,\theta,\varphi) = \frac{-ik_0 f'}{2\pi}|E_0(\theta,\varphi)|A(\theta)\vec{u}_k(\theta,\varphi) \tag{4.7}$$

where f' is the focal length of the objective in the image space and $A(\theta)$ is given by:

$$A(\theta) = \sqrt{\frac{\cos\theta}{n}}\exp\left[-(\frac{n\gamma\sin\theta}{\mathrm{NA}})^2\right] \tag{4.8}$$

here the factor $\sqrt{\frac{\cos\theta}{n}}$ is introduced to guaranty the energy conservation out of the objective aperture.

Due to the focusing of the high NA objective, the wavevector of each plane wave points to the focus point. Thus, the field taken by each wavevector $\vec{k}$ rotates in the image space. And the rotation angle of each plane wave depends on it's own position (x, y) in the aperture of the objective. To analyze the field $\vec{E}$ taken by each wavevector $\vec{k}$, a local frame is introduced where $\vec{e}_r$ points the $\vec{k}$ vector direction, and $\vec{e}_\varphi$ is perpendicular to the plane formed by $\vec{k}$ and the optical axis, $\vec{e}_\theta$ lies in this plane and is perpendicular to $\vec{e}_r$.

$$\vec{e}_r = \begin{pmatrix} 0 \\ 0 \\ 1 \end{pmatrix} \quad \vec{e}_\theta = \begin{pmatrix} \cos\varphi \\ \sin\varphi \\ 0 \end{pmatrix} \quad \vec{e}_\varphi = \begin{pmatrix} -\sin\varphi \\ \cos\varphi \\ 0 \end{pmatrix} \tag{4.9}$$

In the image space, the $\vec{e'_r}, \vec{e'_\theta}, \vec{e'_\varphi}$ is expressed as:.

$$\vec{e'_r} = \begin{pmatrix} -\sin\theta\cos\varphi \\ -\sin\theta\sin\varphi \\ \cos\theta \end{pmatrix} \quad \vec{e'_\theta} = \begin{pmatrix} \cos\theta\cos\varphi \\ \cos\theta\sin\varphi \\ \sin\theta \end{pmatrix} \quad \vec{e'_\phi} = \begin{pmatrix} -\sin\varphi \\ \cos\varphi \\ 0 \end{pmatrix} \tag{4.10}$$

The field carried by $\vec{k}$ is described by three components u_{kx}, u_{ky}, u_{kz}. Finally in Cartesian coordinates three components of the field of each plane wave after passing the objective could be written by:

$$\begin{pmatrix} u'_{kx} \\ u'_{ky} \\ u'_{kz} \end{pmatrix} = \begin{pmatrix} u_{kx} \\ u_{ky} \\ u_{kz} \end{pmatrix} \cdot \vec{e}_r * \vec{e'_r} + \begin{pmatrix} u_{kx} \\ u_{ky} \\ u_{kz} \end{pmatrix} \cdot \vec{e}_\theta * \vec{e'_\theta} + \begin{pmatrix} u_{kx} \\ u_{ky} \\ u_{kz} \end{pmatrix} \cdot \vec{e}_\varphi * \vec{e'_\varphi} \tag{4.11}$$

So u_{kx}, u_{ky}, u_{kz} are written as

$$\begin{aligned} u'_{kx}(\theta,\varphi) &= u_{kx}(\cos\theta + \sin^2\varphi(1-\cos\theta)) + u_{ky}\sin\varphi\cos\varphi(\cos\theta - 1) - \\ &\quad - u_{kz}\sin\theta\cos\varphi \end{aligned} \tag{4.12}$$

$$\begin{aligned} u'_{ky}(\theta,\varphi) &= u_{kx}\cos\varphi\sin\varphi(\cos\theta - 1) + u_{ky}(\cos\theta + \cos^2\varphi(1-\cos\theta)) - \\ &\quad - u_{kz}\sin\theta\sin\varphi \end{aligned} \tag{4.13}$$

$$u'_{kz}(\theta,\varphi) = u_{kx}\sin\theta\cos\varphi + u_{ky}\sin\theta\sin\varphi + u_{kz}\cos\theta \tag{4.14}$$

For an arbitrary point S in the focus volume, the field is finally the coherent superposition of all the plane waves from the objective aperture. So, it can be expressed as:

$$\vec{E}(S) = \int_0^{2\pi}\int_0^{\theta_{max}} \vec{E}_k \exp\left[i\left(\vec{k}\cdot\overrightarrow{F'S}\right)\right] \mathrm{d}\Omega \tag{4.15}$$

where the solid angle Ω is written as:

$$\mathrm{d}\Omega = \sin\theta \mathrm{d}\theta \mathrm{d}\varphi \tag{4.16}$$

In our calculation the objective is a water immersion objective (refractive index in the focus volume is 1.33), and the NA of the objective is 1.2 , the focal length is 4.1mm. We respectively calculated the electric field in the focus volume for a X orientated linear polarization light and a radial polarization light. For linearly polarized light along direction α,

$$\vec{E}_0(\theta,\varphi) = \begin{pmatrix} E_0\cos\alpha \\ E_0\sin\alpha \\ 0 \end{pmatrix} \tag{4.17}$$

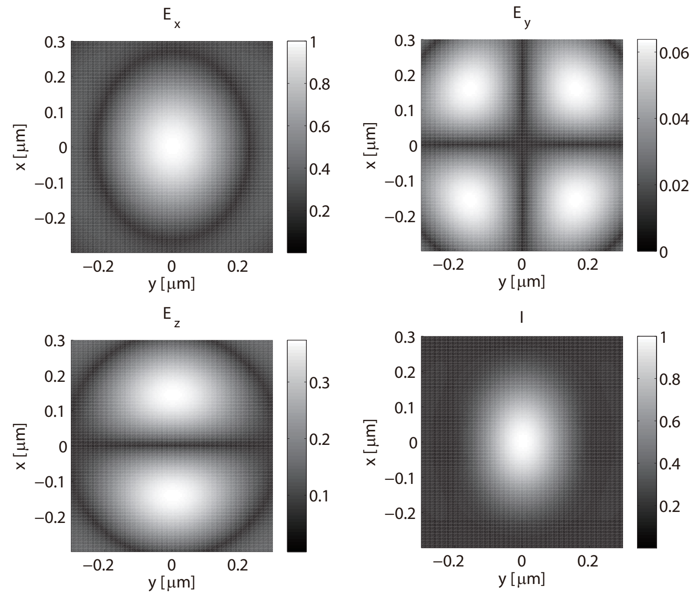

Figure 4.8: For a linear polarized input light along X ($\alpha = 0$), the focusing electric field map ($|E|$) and intensity map of at the focus plane of a high NA objective.

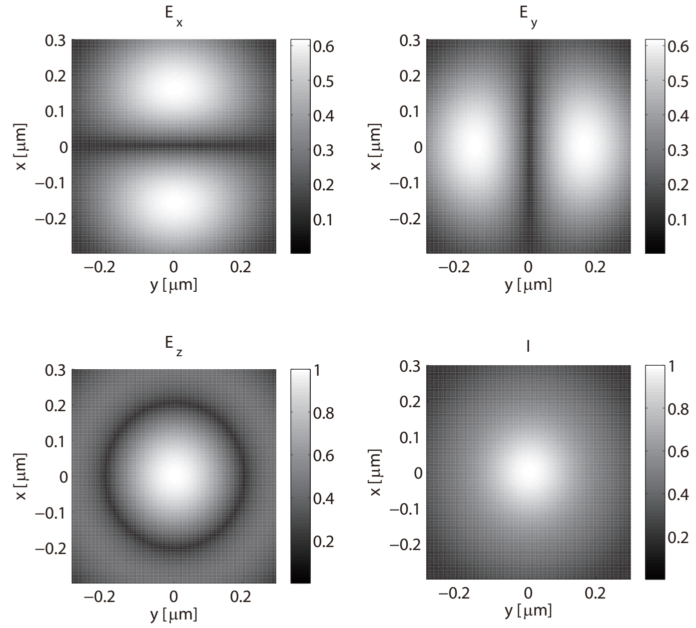

Figure 4.9: For radial polarized input light, the focusing electric field map and intensity map of at the focus plane of a high NA objective.

for radially polarized light

$$\vec{E}_0(\theta,\varphi) = \begin{pmatrix} E_0 \cos\varphi \\ E_0 \sin\varphi \\ 0 \end{pmatrix} \tag{4.18}$$

Fig. 4.8 and Fig. 4.9 depict the electric field $|\mathrm{E_x}|$, $|\mathrm{E_y}|$, $|\mathrm{E_z}|$ and intensity I distribution on the focal plane respectively for linear polarization and radial polarization input light. We also calculated the polarization states distribution in the whole focal volume for linearly and radially polarized input, as shown in Fig. 4.6.

4.2.3 Emission field by an excited dipole

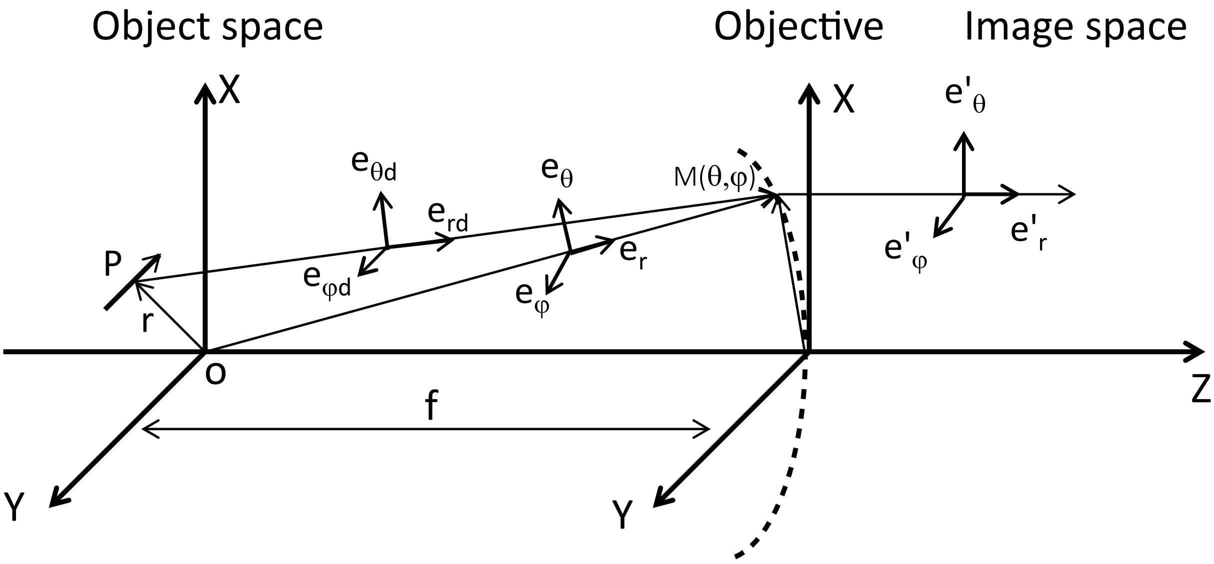

Figure 4.10: The scheme of the emission field from a single fluorescence dipole through a high NA objective.$\vec{P}$: the dipole, $\vec{r}$: the position of the dipole to the center of the focal volume, f: the focal length of the objective, $\vec{r_d}$: the vector from the dipole to the measurement point M, $\vec{e}_r$: the vector between the origin O to the measurement point M,$(\vec{e}_r, \vec{e}_\theta, \vec{e}_\varphi)$:the local frame carried by $\vec{e}_r$, $(\vec{e}_{rd}, \vec{e}_{\theta d}, \vec{e}_{\varphi d})$:the local frame carried by $\vec{e}_{rd}$.

In this section, we will detail the emission field of a single dipole behind in the back-focal plane. As shown in Fig. 4.10 before the objective for arbitrary points $M(\theta,\varphi)$ positioned on the reference sphere of the objective, the field $\vec{E}(M)$ radiated by a single fluorescence dipole $\vec{P}$ is expressed as:

$$\vec{E}(M) \propto \vec{k} \times \vec{k} \times \vec{P} = k^2 \; P \sin(\vec{P}, \vec{e}_{rd}) \times \vec{e}_{\varphi d} \tag{4.19}$$

where the $\vec{r}_d$ is the unit vector between the dipole and point M. $(\vec{e}_{rd}, \vec{e}_{\theta d}, \vec{e}_{\varphi d})$ is the local frame carried by the vector $\vec{r}_d$. $(\vec{P}, \vec{e}_{rd})$ indicates the angle between dipole $\vec{P}$ and vector $\vec{e}_{rd}$.

In the local frame, the vector $\vec{e}_{rd}$ and $\vec{e}_{\varphi d}$ could be calculated as

$$\vec{e}_{rd} = \frac{f \cdot \vec{e}_r - \vec{r}}{|f \cdot \vec{e}_r - \vec{r}|} \qquad \vec{e}_{\psi d} = \frac{(\vec{P} \cdot \vec{e}_{rd})\vec{e}_{rd} - \vec{P}}{|(\vec{P} \cdot \vec{e}_{rd})\vec{e}_{rd} - \vec{P}|} \tag{4.20}$$

and $\sin(\vec{P}, \vec{e}_{rd})$ could be calculated by:

$$\sin(\vec{P}, \vec{e}_{rd}) = \sqrt{1 - (\vec{P} \cdot \vec{e}_{rd})^2} \tag{4.21}$$

where f is the focal length of the objective, vector $\vec{r}$ indicate the position of dipole $\vec{P}$ respect to origin O and $(\vec{e}_r, \vec{e}_\theta, \vec{e}_\varphi)$ is the local frame carried by the vector $f \cdot \vec{e}_r$ is the normalized vector between the origin O and point M. $(\vec{e'_r}, \vec{e'_\theta}, \vec{e'_\varphi})$ is the local frame carried by the corresponding vector $\vec{e'_r}$ of vector $\vec{e}_r$ after passing the objective (see Fig. 4.10) (note that even though the chosen notation is the same, these vectors are defined here for the detection scheme while they were defined in Section 4.2.2 for the excitation scheme).

$$\vec{e_r} = \begin{pmatrix} \sin\theta\cos\varphi \\ \sin\theta\sin\varphi \\ \cos\theta \end{pmatrix} \quad \vec{e_\theta} = \begin{pmatrix} \cos\theta\cos\varphi \\ \cos\theta\sin\varphi \\ -\sin\theta \end{pmatrix} \quad \vec{e_\varphi} = \begin{pmatrix} -\sin\varphi \\ \cos\varphi \\ 0 \end{pmatrix} \tag{4.22}$$

$$\vec{e'_r} = \begin{pmatrix} 0 \\ 0 \\ 1 \end{pmatrix} \quad \vec{e'_\theta} = \begin{pmatrix} \cos\varphi \\ \sin\varphi \\ 0 \end{pmatrix} \quad \vec{e'_\varphi} = \begin{pmatrix} -\sin\varphi \\ \cos\varphi \\ 0 \end{pmatrix} \tag{4.23}$$

The field $\vec{E}'(M)$ carried by vector $\vec{e'_r}$ could be obtained by projecting the field in local frame $(\vec{e}_r, \vec{e}_\theta, \vec{e}_\varphi)$ to the corresponding local frame $(\vec{e'_r}, \vec{e'_\theta}, \vec{e'_\varphi})$ in the image space (see Fig. 4.10):

$$\vec{E}'(M) = (\vec{E}(M) \cdot \vec{e}_r)\vec{e'_r} + (\vec{E}(M) \cdot \vec{e}_\theta)\vec{e'_\theta} + (\vec{E}(M) \cdot \vec{e}_\varphi)\vec{e'_\varphi} \tag{4.24}$$

We have now all the elements to model the emission field for a single dipole with arbitrary position and orientation. Here we present the emission field behind the objective for dipole at the focus point respectively along the X, Y and Z axes, as shown in

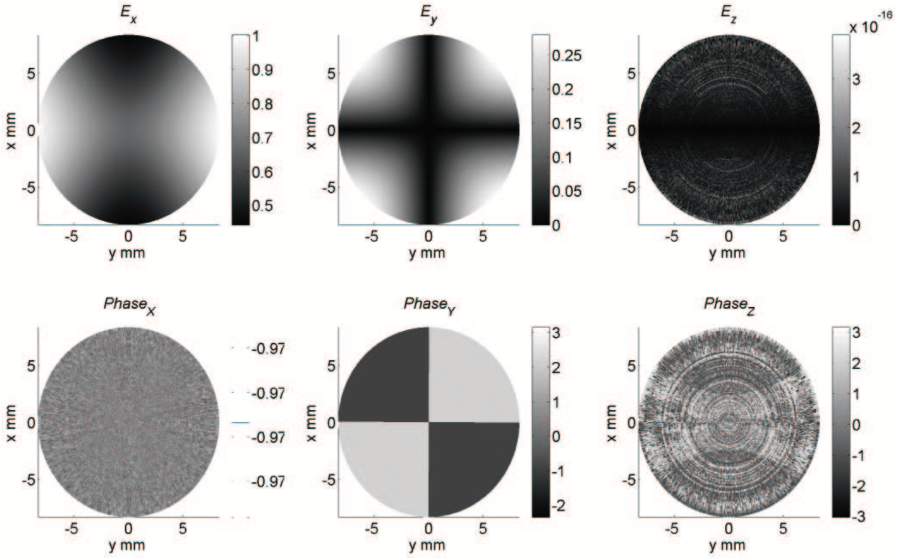

Figure 4.11: For a single dipole parallel to the X axis and located at the center of focal volume, the emission field map of E_x, E_y,E_z and the their phase distribution after passing a high NA objective.

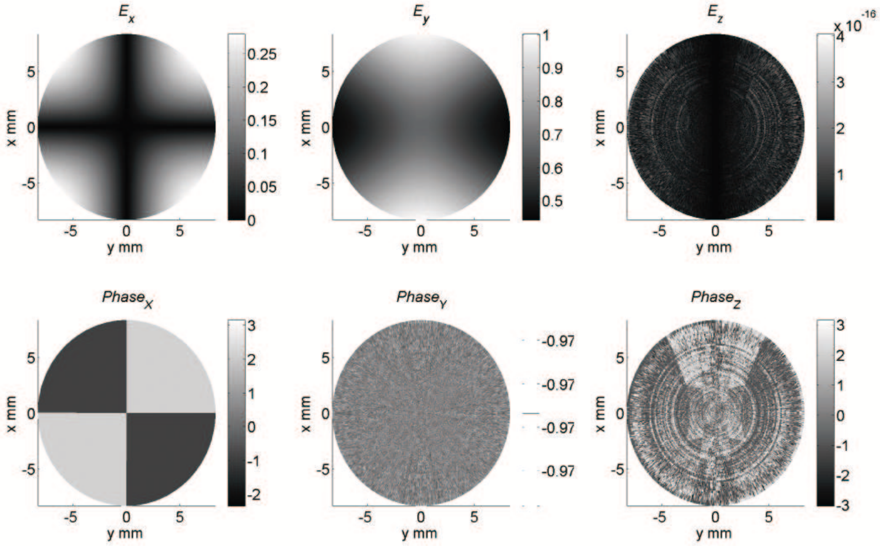

Figure 4.12: For a single dipole parallel to the Y axis and located at the center of focal volume,the emission field map of E_x, E_y,E_z and the their phase distribution after passing a high NA objective..

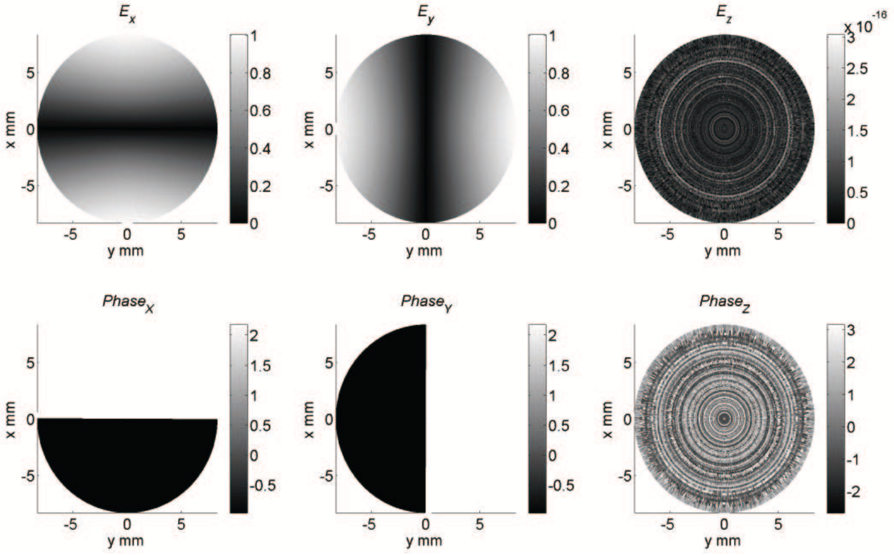

Figure 4.13: For a single dipole parallel to the Z axis and located at the center of focal volume,the emission field map of E_x, E_y,E_z and the their phase distribution after passing a high NA objective..

Fig. 4.11,Fig. 4.12 and Fig. 4.13. Any orientation of dipole could be decomposed into these three orientations. Moreover, when a dipole shifts by a little distance with respect to the focus point, the phase distribution also varies but the amplitude maps of the electric field remain the same as that of the dipole located at the focus point.

From these three figures, it is clearly visible that the emission field behind the objective is a transverse field for an arbitrary orientation of the dipole in the (X, Y) plane, in addition the polarizations of the emission field behind the objective exhibit the same orientation as the dipole. The field of a dipole along Z direction exhibits a $0|\pi$ phase difference and symmetrical amplitudes, that is the reason why a $0|\pi$ phase plate is required for breaking the symmetry to detect out-of-plane oriented dipoles. The random phase distribution for E_z in these figures is purely numerical has no meaning since the amplitude is zero.

4.2.4 Image of a dipole and detection efficiency

Finally to calculate the image of a dipole, the emission field behind the objective (within its aperture defined by NA) is refocused by a lens into a pinhole and collected by a detector. In this part we compute the intensity pattern on the focal plane of the lens and

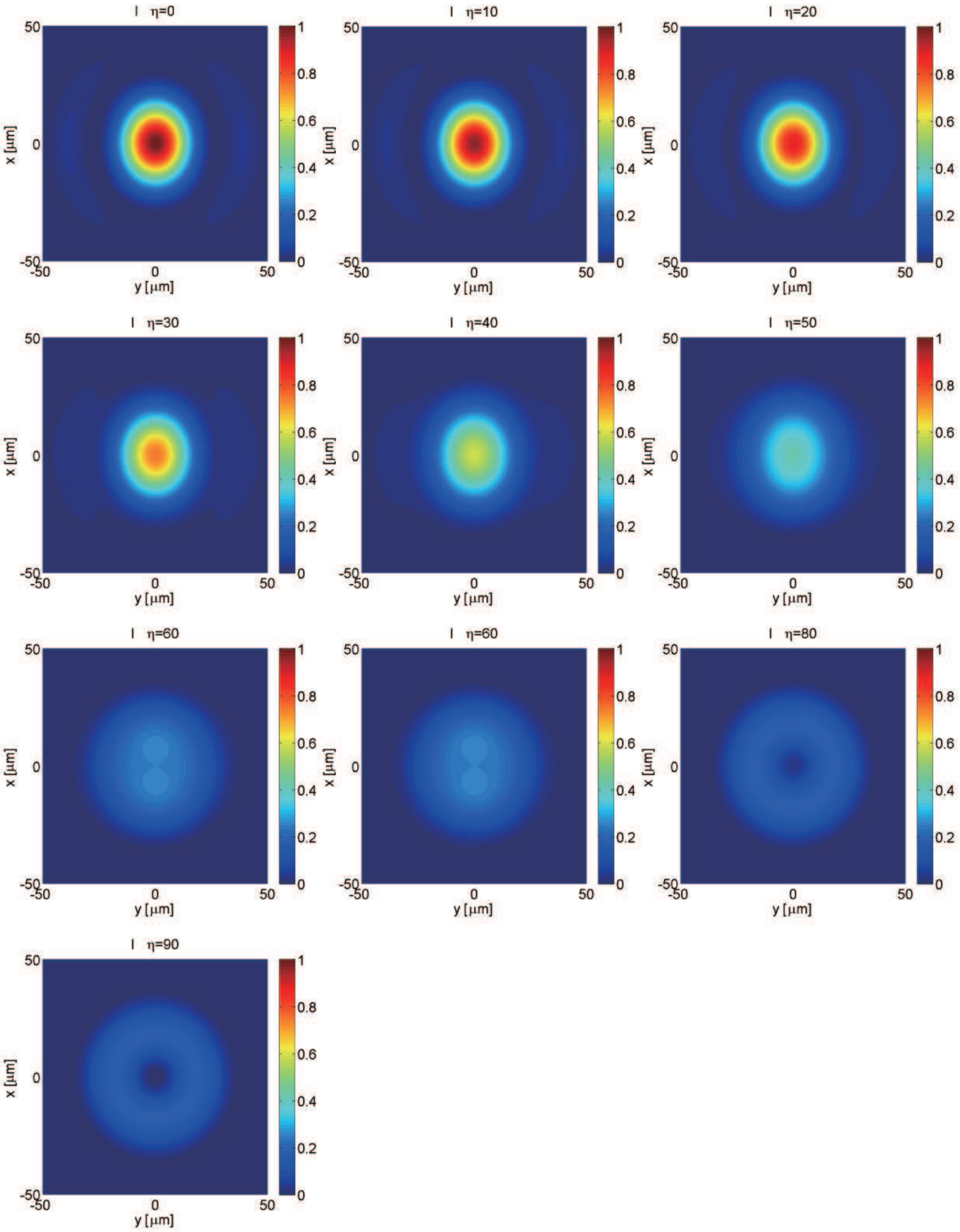

Figure 4.14: Intensity pattern (in the image focal plane) for a single dipole located in the focal point with varied orientation η respect to the X axis ranging from 0° to 90°.

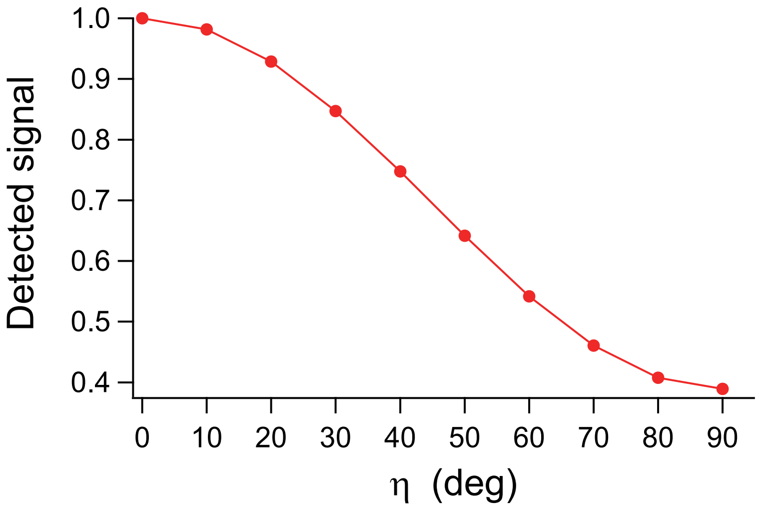

Figure 4.15: Effect of the out-of-plane angle on the collection efficiency for a single dipole.

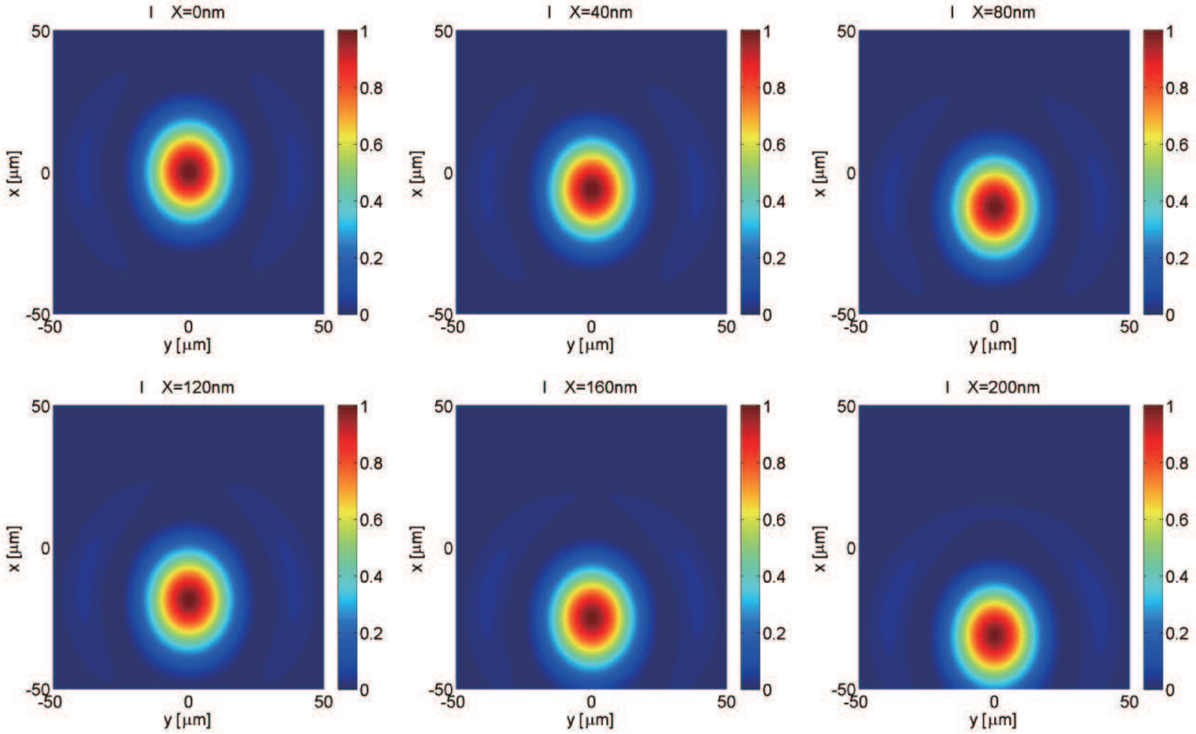

Figure 4.16: Intensity pattern. Effect of a lateral shift of a dipole.

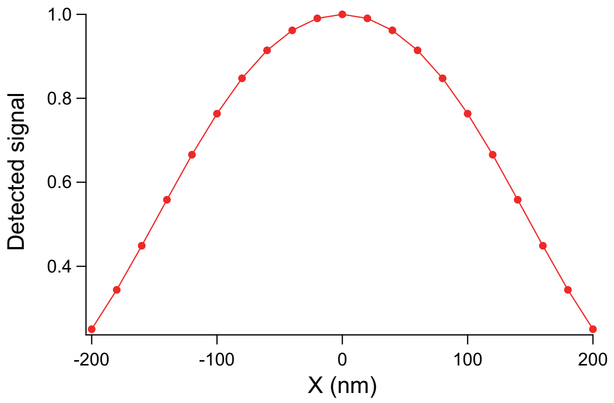

Figure 4.17: Effect of a lateral shift of the dipole on the detected signal

the total signal acquired by the detector behind the pinhole. We also show how it varies with the dipole position and orientation.

Calculating the focusing part is similar to the calculation of the excitation field presented in Section 4.2.2 with replacing the objective by a lens. Considering the size of the emission beam behind the objective and the telescope in the detection path, the real focusing effect is equivalent to a lens with a focal length of 450 mm and NA of 0.0111 (the beam diameter is 10 mm behind the objective, and the magnification of telescope is 3, and actual focal length of the lens is 150 mm).

Considering a emitting dipole at the focus point of the objective, the intensity patterns in the focal plane of the focusing lens are shown in Fig. 4.14 with out-of-plane orientations η varying from 0 to 90 degrees respect to the X axis in the XZ plane. When the orientation of a dipole varies from X to Z, the intensity pattern is progressively spreading, which causes a decrease of signal through the pinhole. As shown in Fig. 4.15 the detected signal obtained by summing up of the intensity inside the pinhole (diameter of $50\mu m$) decreases with η increasing from $0°$ to $90°$.

We describe now the variation of the intensity pattern and the detected signal when the position of the dipole is varied whthin the focal volume. In this calculation, the dipole with orientation parallel to X is shifted along X as well as along Z. The results about the intensity pattern variation are respectively presented in Fig. 4.16 and Fig. 4.18. When the dipole shifts along the X axis the intensity pattern also shifts in opposite direction with remaining shape (as expected from imaging properties), while when the dipole shifts along the Z axis the intensity pattern is spreading. Both of the two cases will cause a decrease of the detected signal, which are respectively presented in Fig. 4.17 and Fig. 4.19 where,

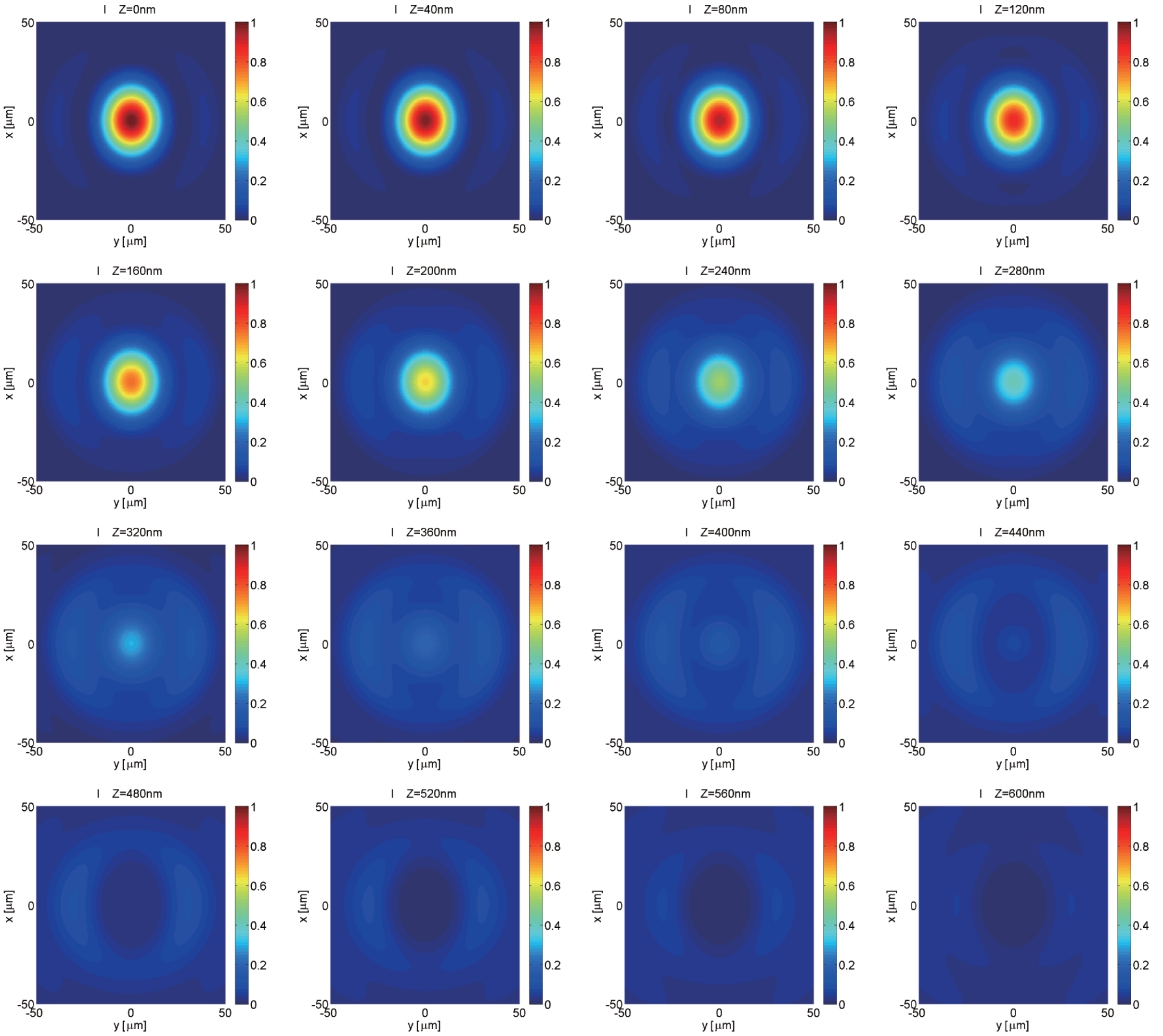

Figure 4.18: Intensity pattern. Effect of an axial shift of a dipole.

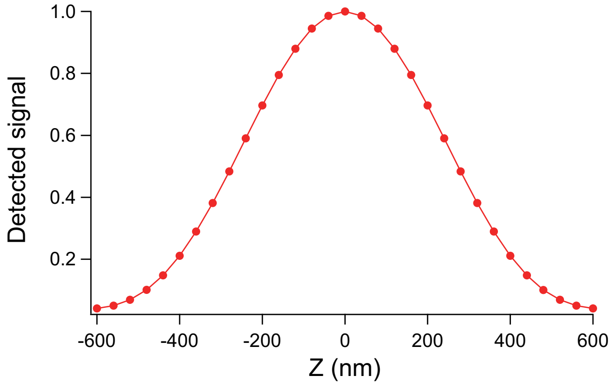

Figure 4.19: Effect of an axial shift of the dipole on the detected signal.

predictably, we recognize the detection point spread function of a confocal microscope . Note that the position shifting along Y axis has same the effect as shifting along X axis on the intensity pattern and the detected signal. Consequently, the dipoles in the focal volume will affect the measurements due to different detection efficiencies.

4.3 Proposed method to probe the order in 3D

4.3.1 Scanning scheme of the polarization of the exciting field

As mentioned above, inspired by the method to retrieve the in-plane orientation and the orientation order of a cone, we propose a scheme to simultaneously probe the out-of-plane orientation η and order information ψ of a cone by analyzing the emission intensity dependence when tuning the out-of-plane polarization angle of the exciting light. In this scheme (as shown in Fig. 4.20(b)) the out-of-plane polarization orientation of the exciting light, denoted by β, is rotated from 0° to 180° in the plane constructed by Z axis and the in-plane projection of the field. In order to reveal the 3D orientation (ρ, η) and order information (ψ), the method relies on the analyzing of the emission responses on the in-plane polarization orientation α and out-of-plane polarization orientation β of exciting light. The additional tuning parameter β should provide information on η, in the same way that α was providing information on ρ. As shown in Fig. 4.20(b), where the vectors from origin to the pink circles indicate the polarization orientation of the exciting field $\vec{E}$, the in-plane polarization orientation α is rotated from 0° to 180° along the blue circle in the XY plane, and for every in-plane orientation α the out-of-plane polarization

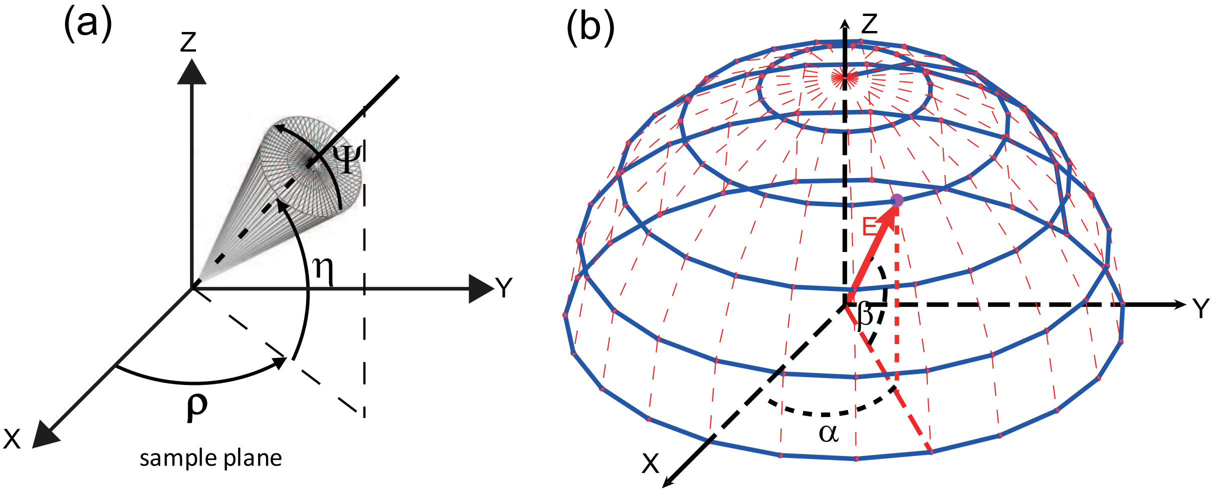

Figure 4.20: The polarization scanning scheme. α and β respectively indicate the in-plane and out-of-plane polarization orientation of exciting light.

orientation is set from 0° to 180° along the red dashed line in the corresponding vertical plane defined by $\vec{E}$ and Z.

The proper orientation (α, β) of the exciting field will be produced by the coherent sum of (1) a field in the (X,Y) plane and (2) an out-of plane field. This requires to generate in the back focal plane of the objective lens a sum of a linearly polarized field and a radially polarized field with the appropriate ratio. Note that the Z polarization produced by the radial polarization is only true at the center of the focal volume (see Fig 4.6), however we will demonstrate below that this scheme is sufficient to quantify, with a good contrast, the 3D information on a molecular distribution.

Now we present in detail the calculation of the arbitrary control of the out-of-plane polarization orientation β. To guarantee the identical exciting intensity at the focus point for different β, the total input light intensity is assumed to be 1. The input light is split into two paths, in one path the light is linearly polarized and the intensity is weighted by a factor T, and in another path the light is transfered to radially polarized light with intensity weight of $1 - T$. For a given out-of-plane orientation β, the T value can be obtained by:

$$T = \frac{\tan(\beta)^2}{1 + \tan(\beta)^2} \tag{4.25}$$

Considering the different focusing efficiency between linear and radial polarized light, the linear polarized input light should be attenuated by a factor R which depends on the property of the objective. For our objective with $NA = 1.2$ and focal length of 4.1mm, the factor R is 2.09, which is the intensity ratio between the linear and radial polarization input at the focusing center (calculation of excitation field presented in Section 4.2.2). For β from 0° to 90°, the linear and radial polarized light keep an identical phase. For β from 90° to 180°, there is a phase difference of 180° between linear and radial polarized input lights Therefore, to rotate the exciting polarization in 3D, one needs to take care of setting the appropriate relative phase.

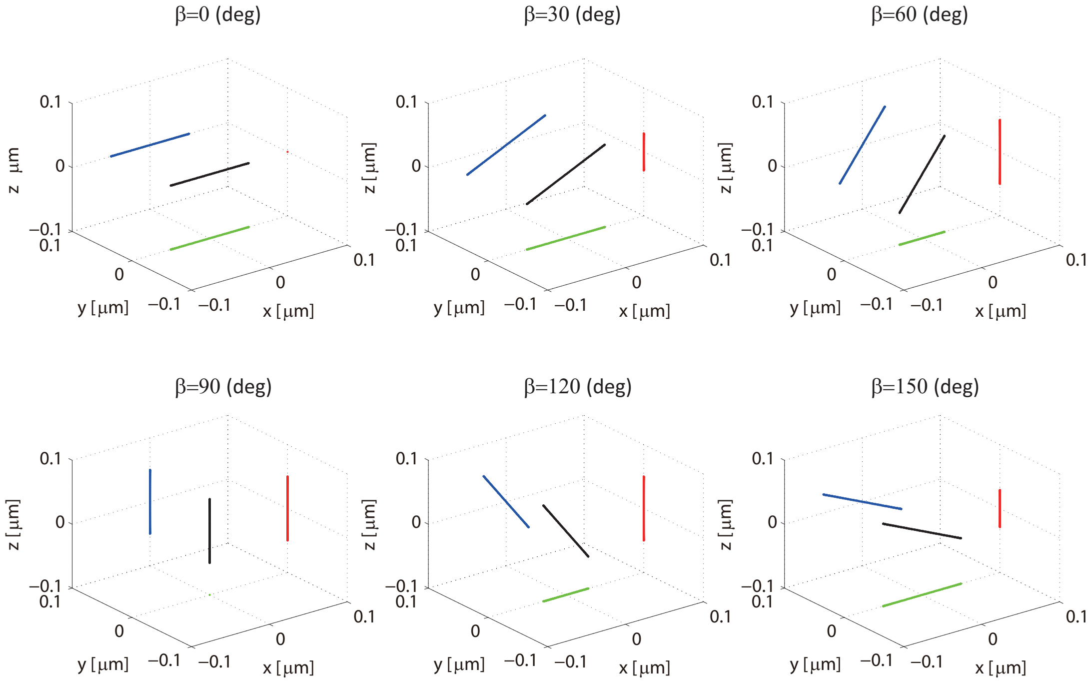

Figure 4.21: the 3D polarization state at the focus center and its projection on three orthogonal planes (red: YZ plane, green: XY plane,blue: XZ plane) for different off-plane angles β which is achieved by tuning the ratio between input linear and radial polarized lights.

Here, we present the polarization states at the focal point for mixed fields with different ratios as shown in Fig. 4.21. We can see that the out-of-plane orientation β can be rotated perfectly from 0° to 180° at the focus center by this method. We also calculate the polarization state in the whole focusing volume (presented in Fig. 4.22). The polarization is elliptically polarized except at the focus center. Although the ellipticity and orientation are dependent on the position in the focal plane, the main component of the electric field

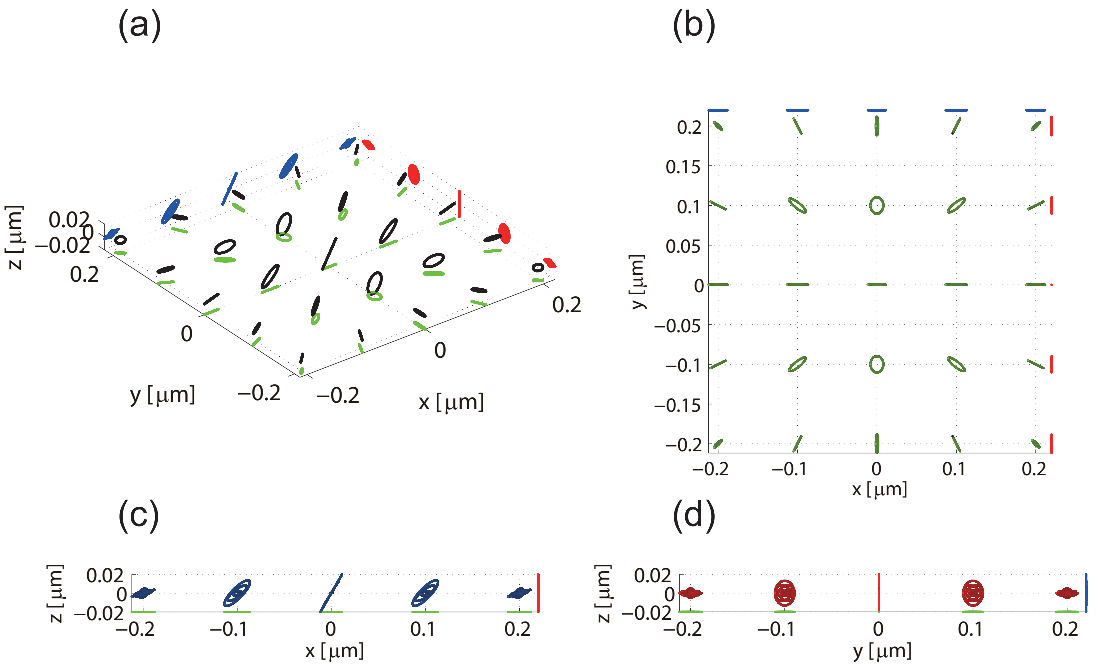

Figure 4.22: For $\beta = 60°$, the 3D polarization state on the focal plane and its projection on three orthogonal planes.

is oriented along β. At the border of the focal plane the polarization is no more purely longitudinal. This however will not affect significantly the results since this region of the excitation volume exhibits a weaker intensity(demonstrated below).

4.3.2 Unambiguous retrieval of (η, ψ)

In this part we present the method to retrieve the out-of-plane orientation η and the cone aperture ψ from the emission responses obtained when varying the out-of-plane polarization orientation β of the exciting light. The main principle is similar to the method presented in Section 2.3 for retrieving the in-plane orientation ρ and cone aperture ψ, based on the relation between (ρ, ψ) and the Fourier series coefficients (A, B) of the emitting intensity curve $I(\alpha)$. This retrieval presents the advantage to be very fast and can be applied to any estimation problem with a sinusoidal response and two unknown parameters. Inspired by this method, in our 3D approach we also want to retrieve the η and ψ by building a relation between (η, ψ) and the Fourier series coefficients (A, B) of the emitting intensity curve $I(\beta)$. In the following, that is presented in detail.

By analyzing the emitting intensity variation with respect to the in-plane polarization rotation of the exciting light, the in-plane orientation ρ could be obtained easily and independently from ψ. For simplifying the computation, here we assume that $\rho = \alpha = 0$. So, the emitting intensity could be written as:

$$I(\beta) = \iiint \overline{|\vec{\mu}(\theta, \phi, \eta, r) \cdot \vec{E}(\beta, r)|}^2 |E_m(\theta, \phi, \eta, r)|^2 f(\theta, \phi) \sin\theta \mathrm{d}\theta \mathrm{d}\phi \mathrm{d}r \tag{4.26}$$

In this part, we start with a single cone located at the focus center point, the emitting intensity could be expressed as:

$$I(\beta) = \iint \overline{|\vec{\mu}(\theta, \phi, \eta) \cdot \vec{E}(\beta)|}^2 |E_m(\theta, \phi, \eta)|^2 f(\theta, \phi) \sin\theta \mathrm{d}\theta \mathrm{d}\phi \tag{4.27}$$

From the intensity expression, which is similar to eq. 4.1, we can find that the emitting intensity $I(\beta)$ has a sinus dependence on the polarization angle β with a period of 180°. So, it could be written as:

$$I_{\eta,\psi}(\beta) = I_0[1 + A(\eta, \psi)\cos(2\beta) + B(\eta, \psi)\sin(2\beta)] \tag{4.28}$$

with

$$A(\eta, \psi) = \frac{2}{I_0\pi}\int_0^\pi \mathrm{d}\beta I_{\eta,\psi}(\beta)\cos(2\beta)$$

$$B(\eta, \psi) = \frac{2}{I_0\pi}\int_0^\pi \mathrm{d}\beta I_{\eta,\psi}(\beta)\sin(2\beta) \tag{4.29}$$

$$I_0 = \frac{1}{\pi}\int_0^\pi \mathrm{d}\beta I_{\eta,\psi}(\beta) \tag{4.30}$$

And then the relationship between the set of (η, ψ) and (A, B) is calculated for every set of (η, ψ). The η varies from 0° to 180° with a step of 10°, and ψ also ranges from 0° to 180° with a step of 2°. In our calculation for a cone with given mean orientation η and cone aperture ψ, the polarization β of the exciting light is rotated from 0° to 180° with step of 10° and the correspondence emitting light intensity $I(\beta)$ is calculated according to eq. 4.27. Based on the emitting intensity curve $I(\beta)$ the (A,B) value are calculated by using the expression 4.29 for this pair of (η, ψ). We do the same calculation for every set of (η, ψ) and finally the relationship between (A, B) and (η, ψ) is illustrated in two disk-like figures as shown in Fig. 4.23, where one disk is made for η and another is for ψ. From these two disks, it is very convenient to retrieve the value of η and ψ by unambiguously.

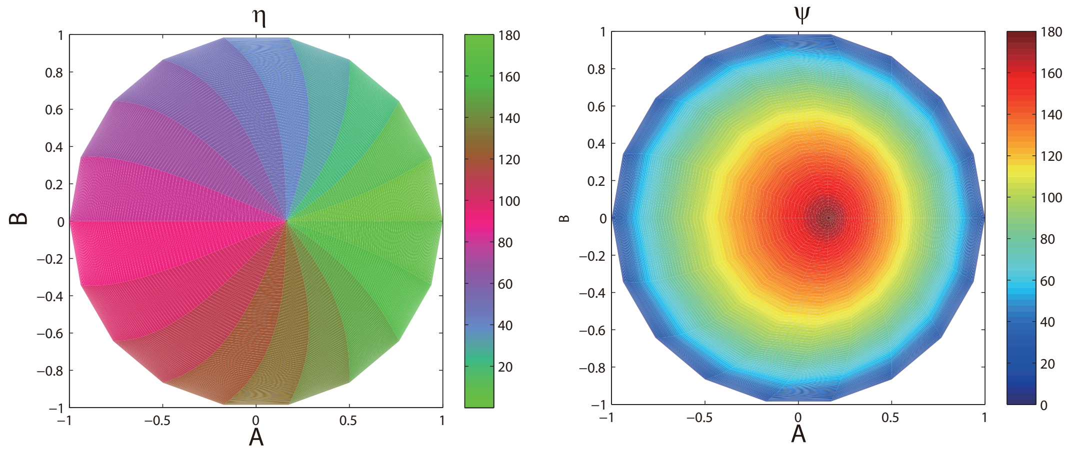

Figure 4.23: The relationship between (η, ψ) and (A, B) for a single cone located at the focus center. Left: η as a function of (A, B), the dependence is purely azimuthal (with slight distortion). Right: ψ behaves as a radial dependence on (A, B) (with slight distortion).

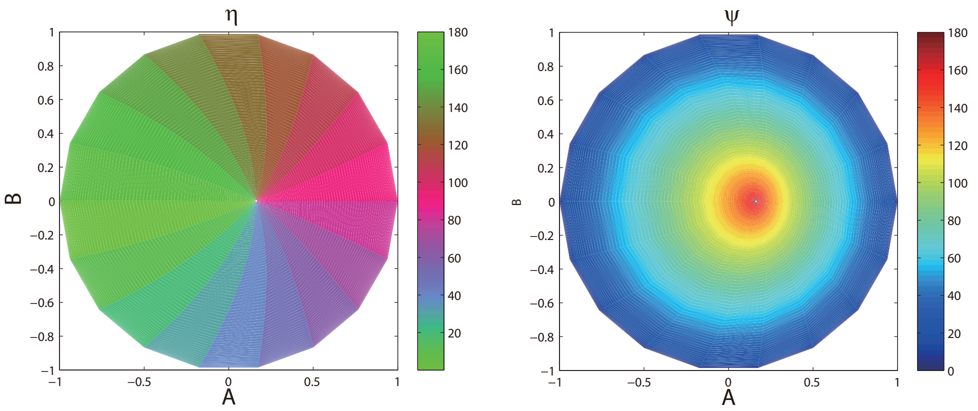

Figure 4.24: The relationship between (η, ψ) and (A, B) for a Pancake model located at the focus center. Left: η as a function of (A, B), the dependence is purely azimuthal (with slight distortion). Right: ψ behaves as a radial dependence on (A, B) (with slight distortion).

By observing these two disks, we can find that these two disks are slightly distorted, compared to the (ρ, ψ) disks shown in Section 2.3 above. In the η disk the radial distribution is not uniform and twisted, moreover the center is shifted to the right, which also happens to the disk of ψ. All these 'distortions' are introduced because the emitting intensity depends on the out-of-plane angle of the emitting dipole as discussed above. However, this 'distortion' does not affect the one-to-one correspondence relationship between the set of (η, ψ) and (A, B).

Besides the cone model, as mentioned above some fluorescence dipoles such as DiIC_{18} lie on the surface of the cell membrane, that could be modeled as a pancake-like distribution. For such pancake model, the same computation is performed as for a cone model and the relation between the set of (η, ψ) and (A, B) is illustrated as Fig. 4.24. The behavior is very similar to a cone model.

4.3.3 The membrane geometry

In the discussion above, we demonstrated the validation of the method for a single cone which is placed exactly in the focus center point. However, in confocal microscopy the focus spots occupies a volume about 400nm × 400nm × 600nm$(X \times Y \times Z)$, which is the point spread function (PSF) of the objective. As discussed above, in the focus volume the exciting field and the detection efficiency of the emission light depend on the considered position, which would definitely affect the final signal acquired by the detector. In the following, we detail how the PSF influences our method to retrieve the 3D orientation information of the cell membrane.

As mentioned above, the molecules in cell membranes are characterized by a cone model which is perpendicular to the cell membrane surface. Considering the position of the membrane in the focusing volume, it is assumed that the cones are positioned in a very thin flat plane which normal orientation is given by (ρ, η). The cones are oriented perpendicularly to this plane, as shown in Fig. 4.25(a).

In the calculation, a flat plane is placed at the center of the focusing volume. For simplifying the computation, the in-plane orientation ρ is assumed to be already known and to be 0. We make a similar calculation to build the relationship between the set of (η, ψ) and (A,B) as we did for a single cone. The difference is that in the membrane case the plane also rotates with the variation of η, which results in position changes of the cones in the focal volume for different η as presented in Fig. 4.25(b). Therefore, in this calculation the position change should be considered for different η. When $\eta = 0$ the

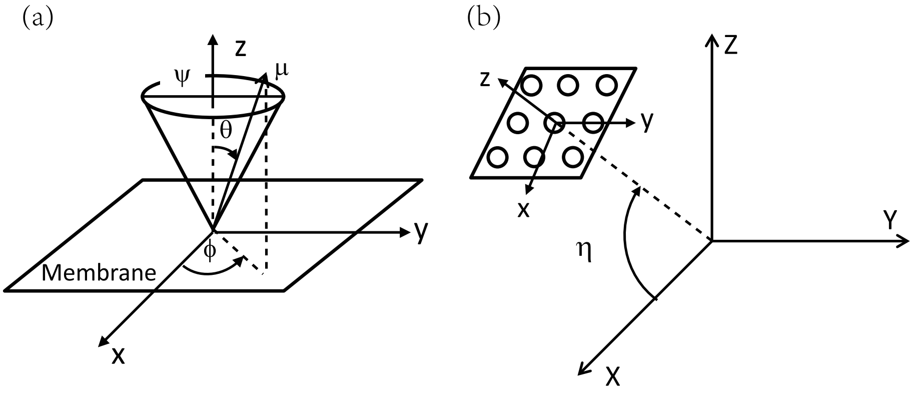

Figure 4.25: Schematic presentation of a single dipole in a cone which is perpendicular to a plane representing the membrane.(a) A single dipole (μ) in a cone, in the local microscopic frame the out-of-plane and in-plane orientation are respectively indicated by θ and ϕ, the cone axis is perpendicular to the plane.(b) The plane is oriented in the macroscopic frame by the (ρ, η) angles.

frame of the cones is set to be $[X, Y, Z]$, and when the plane rotates by η the frame is changed to a new one denoted by $[X', Y', Z']$. The transformation between $[X, Y, Z]$ and $[X', Y', Z']$ can be made by a rotation matrix around the Y axis:

$$R(\eta) = \begin{pmatrix} \cos\eta & 0 & -\sin\eta \\ 0 & 1 & 0 \\ \sin\eta & 0 & \cos\eta \end{pmatrix} \tag{4.31}$$

In order to keep reasonable precision and calculation time, 9 cones are distributed in the flat plane with spacing of 200nm in the two directions of the membrane plane. In our calculation, the (η, ψ) and β values are sampled similarly as we did above for a single cone. For every set of (η, ψ) the β dependence of the total emission intensity summed 9 cones on β is calculated. Finally as for a single cone, the relation between the set of (η, ψ) and (A, B) is illustrated by two maps as shown in Fig. 4.26. Compared to the results of the single cone, the two disks are not round any more and more distorted because of the dependencies of the exciting field and detection efficiency on the dipoles position in the focal volume.

We performed the same calculation for the pancake model distributed in a plane. The relation between the set of (η, ψ) and (A, B) is also calculated and illustrated in Fig. 4.27. Compared with the cone model, the disk shifts to the left and a degree of overlap occurs at

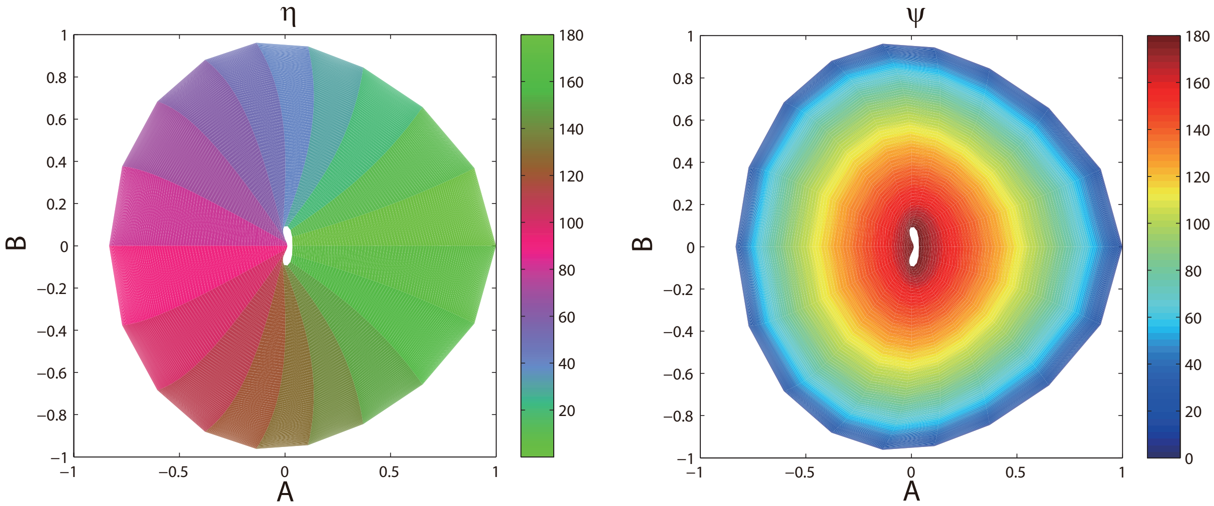

Figure 4.26: The relation between the set of (η, ψ) and the set of (A, B) for a plane perpendicularly distributed cones located in focusing volume.

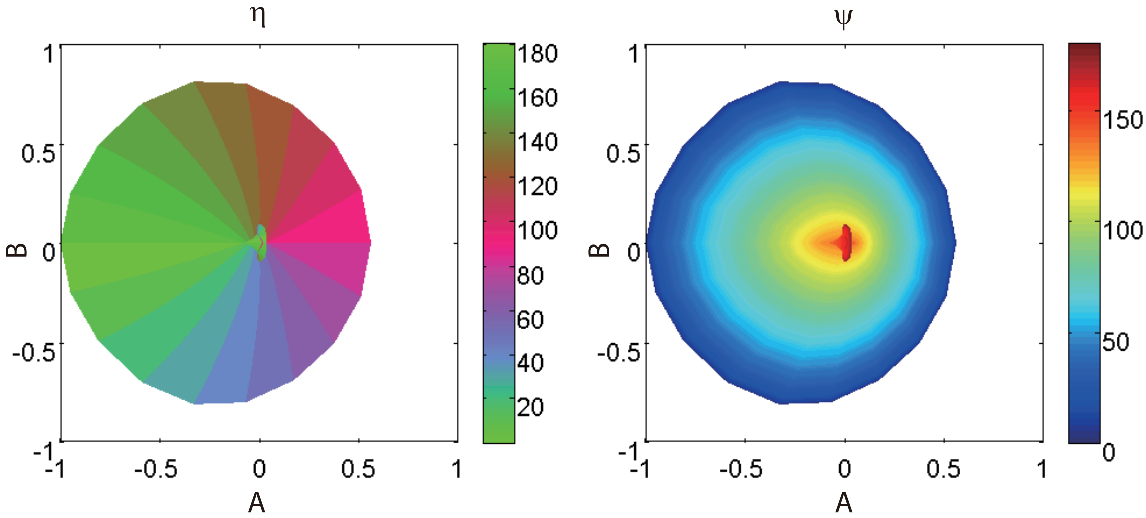

Figure 4.27: The relation between the set of (η, ψ) and the set of (A, B) for a plane perpendicularly distributed pancake model located in focusing volume.

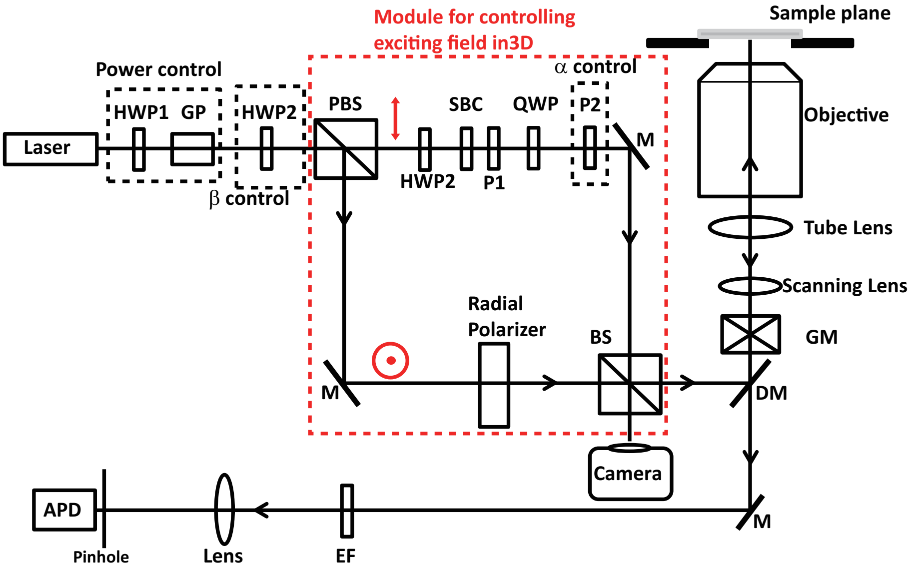

Figure 4.28: A proposed practical setup. The module for controlling the polarization is emphasized by the red rectangle frame. Notations are the same as in Fig. 2.3.

the center of the disk. This confines our method to the cases $\psi < 130°$ because for higher ψ values, the relations between (η, ψ) and (A,B) becomes ambiguous and multiple solutions can exist. This is because compared to cone model, the geometry of pancake model make results more easily affected by the dipoles position and orientation dependencies of emission detection and the excitation. Therefore, for large ψ, the "distortion" confuses the results.

Finally, this model shows that the measurement of molecular order in a membrane of known geometry can be performed in 3D using a polarization-resolved 3D approach, using a similar fast processing method as developed in the previous chapters.

4.3.4 Practical setup

In this part, according to the discussion above to retrieve 3D orientation information in an ensemble of molecules, we propose a setup which is able to perform a tuning of α and β from 0° to 180°.

The optical setup is presented in Fig. 4.28. It is based on the setup of chapter 2 (Fig. 2.3). The only difference is that the in-plane polarization modulator is replaced by a 3D polarization modulator (emphasized by the red rectangle frame) which sums the linearly and radially polarized incident light. The mixing of the linear and radial polarized light is complemented by a Mach-Zehnder interferometer. This configuration should allow to reach any (α, β) 3D field orientation and in particular to tune α and β independently to retrieve the complete 3D information on the molecular distribution. The β angle is rotated by tuning the ratio between linear and radial polarized light paths, which is controlled by a rotated half wave plate (HWP2) followed by a polarization beam splitter. In the radial polarization path, the linear polarized light is transformed into a radial polarized light by a radial polarizer element, for instance a liquid crystal device (Arcoptix). In the linear polarization path, a polarizer P1 is introduced to attenuate the light by a factor R (R=2.09 for our objective) in the linear path relative to the radial path, as discussed above to compensate for the different focusing efficiency of linear and radial polarized light. Then the in-plane polarization orientation α is controlled by a rotated polarizer (P2) placed after a quarter wave plate which produces a circular polarized light by being placed with fast-axis orientated 45° respect to polarizer (P1). This scheme allows to vary α without changing the relative phase between the two arms of the interferometer. The relative phase between the two paths can be changed by slightly tuning the mirrors of by adding a tuneable element such as a Soleil-Babinet compensator set along one of its optical axes. To check the phase difference between two paths, a camera is placed. And then the combined light is reflected into the objective by a dichroic mirror. The rest of the optical bench is unchanged.

A first version of this scheme has been implemented in the lab by a phD student He Wei. The first results are promising since we can identify a complete and independent control of both alpha and beta angles using the method proposed here. the stability of the interferometer is ensured by its compactness and the identification of the α and β rotation angles is made by imaging the full beam surface at the exit of the interferometer, on a small CMOS camera.

4.4 Conclusion

In this chapter, we have presented a new excitation strategy which allows probing the out-of-plane dipoles. It is validated by simulation that the 3D molecular angular distribution can be probed by analyzing the emission response upon the out-of-plane polarization tuning of the excitation light. According to this scheme, a practical setup has been proposed to perform the 3D polarization scanning in the focusing volume of a microscopy objective.

Conclusion and outlooks

The aim of this PhD project was to develop optimized scheme for the technique of angle-resolved linear dichroism. Starting from the proof of principle that was experimentally demonstrated in our group, we considerably improved the experimental methodology as well as the data processing strategy. This allowed us (i) to reduce polarization distortions that could strongly affect the measured data, (ii) to take into account residual distortions in the data processing, (iii) to provide a numerical model that allows to retrieve the parameters of the angular geometrical model with a high efficiency, (iv) to quantify the expected precision of the method, depending on the measurement conditions. The new optimized scheme has allowed so far to quantify molecular order of lipid probes in cell membranes under physical perturbations [13], structural properties of amyloids [49] as well as orientation properties in actin stress fibers [Kress in preparation].

In order to push forward the time limits of the technique, we have proposed an instrumental implementation based on a multiplexed confocal geometry, using the technology of the spinning disk. This considerably improves the data acquisition rate, making possible precise acquisition at rates of a few tens of images per second. Together with the confocal axial resolution, this opens the door to investigation of 3D complex dynamic samples. For this reason, our experimental bench has been recently equipped with an incubator and moved to the Centre d' Immunologie de Marseille Luminy. It will contribute to investigate local structural changes of acceptor proteins in signaling processes and how the membrane architecture is modified during cell migration.

Because an important limitation of our technique (and of microscopy in general) is its low sensitivity to out-of-plane oriented molecules, we have investigated possible ways to resolve 3D orientations. We have proposed a new excitation strategy that allows, by using a combination of linear and radial polarizations, to monitor the out-of-plane tilt of the fluorescent dipoles. We have developed a 3D numerical model that takes into account the real spatial distribution of the exciting light as well as the dependence of the excitation and collection efficiency depending on the location and orientation of the dipole. The simulations show that 3D orientation distributions can be resolved without ambiguity. Based on this scheme, a practical setup has been proposed to perform 3D polarization scanning in a confocal geometry. Alignment and first calibrations of the excitation path have already started, as the first part of the PhD project of He Wei in our group. In the future static biological samples (in particular the 3D contour of cell membrane) or nanostructures could be investigated using this technique [50].

More generally, developments of angle-resolved linear dichroism can be made by following two directions. First, other contrasts than one-photon fluorescence can be used. For instance, one can mention two-photon absorption fluorescence. Because it allows a better angular selectivity, it should allow in principle to reveal more details on angular distributions. While one-photon fluorescence allows to quantify an angular distribution by two parameters (ρ and ψ in our work) two-photon fluorescence is expected to reveal up to four parameters, providing therefore more information about the molecular organization that is investigated [11, 35].

The second direction of development deals with dynamic properties, especially by running measurement at a single point, without any scanning. Although in this case the “image” will be lost, this approach should allow ultimately to monitor dynamic changes of the molecular organization at time scales below microseconds.

Appendix A

The effect of Homo-FRET on polarization resolved measurements

Förster energy transfer (also called fluorescence resonant energy transfer of FRET) between neighbor molecules is likely to occur in media of high concentration since it takes place at inter-distances of a few nanometers [26]. It is well known that the depolarization of emission light induced by energy transfer between molecules of the same species (known as Homo-FRET) affects the polarization resolved fluorescence techniques that rely on the emission light polarization analysis, such as fluorescence anisotropy method [5, 6]. However, this depolarization is expected to not affect the technique that are based on analyzing the absorption probability of excitation light by monitoring the total fluorescence response dependence to different polarized exciting light, such as linear dichroism. In this Appendix, by modeling the Homo-FRET mathematically for molecules distribution within a cone, we theoretically calculated the total fluorescence response and polarized response in X and Y direction ((X, Y) defining the sample plane) to different polarization angle α of the exciting light. The calculation results are analyzed and confirm that total the fluorescence response to α is independent on the energy transfer effect. Further analysis show that the robustness is even maintained in the geometric case of a cell membrane.

A.1 Modeling the fluorescence response of molecule in a cone with Homo-FRET

FRET studied first by Förster [26], is a mechanism describing energy transfer between a donor dipole and an acceptor dipole through nonradiative dipole-dipole coupling. The efficiency of this energy transfer is inversely proportional to the sixth power of the distance between donor and acceptor making FRET extremely sensitive to small distances (typically less than 10 nm). When donor and accepter is the identical dye, it is called homo-FRET.

In this section, we model mathematically the Homo-FRET effect for an ensemble of molecules angularly distributed in a cone and give the expression to calculate polarization resolved fluorescence responses involving homo-FRET. We will only focus here on the orientational dependence of homo-FRET without detailing the other factors involved in the transfer efficiency such as dipoles inter-distance, spectral overlap and quantum yields [26].

A.1.1 Definition of the coupled dipoles

To express the effect of homo-FRET on the emission of molecules in a cone, both acceptor and donor molecules are defined within the same cone characterized by (ρ, η, ψ) (see Section 2.1). The energy transfer process involves an excitation step by the donor molecule, followed by a transfer of energy to a neighbor molecule (the acceptor) which will be the emitter for the fluorescence radiation. The time taken for the energy transfer process is supposed to be much shorter than rotation times. In the present model the donor and the accepter molecules are respectively defined by their dipole orientation $\mu_1(\theta_1, \phi_1)$ and $\mu_2(\theta_2, \phi_2)$ in the cone frame (x, y, z), as illustrated in Fig. A.1. The relative position between donor and acceptor molecules is defined by the vector $r(\Theta, \Phi)$ also in the cone frame (x, y, z).

The orientations of μ_1, μ_2 and r in the macroscopic frame (X, Y, Z) are written as:

$$\mu_1(\theta_1, \phi_1, \eta, \rho) = \mathbf{M} \times \begin{bmatrix} \sin\theta_1 \cos\phi_1 \\ \sin\theta_1 \sin\phi_1 \\ \cos\phi_1 \end{bmatrix} \tag{A.1}$$

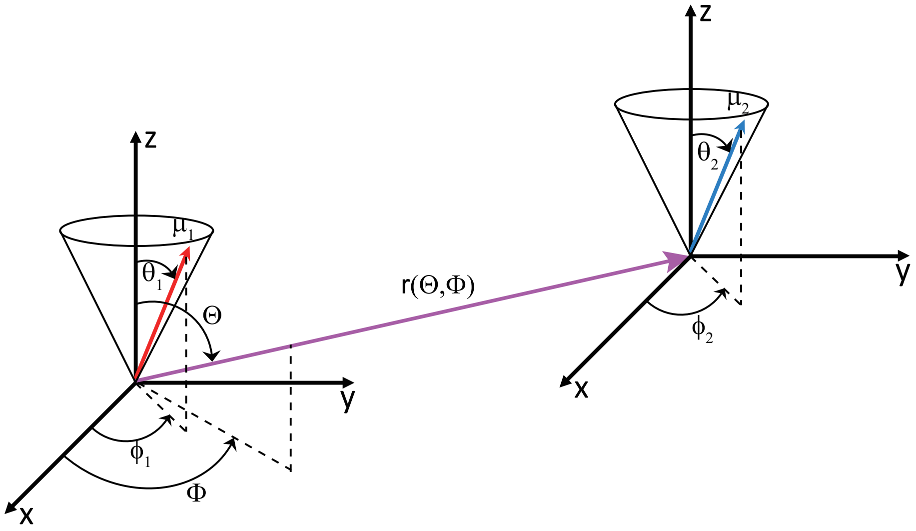

Figure A.1: Orientation of the acceptor (μ_2) and donor (μ_1) molecular excitation-emission dipoles in the homo-FRET process, depicted in (x, y, z) local frame. The orientation of the donor μ_1 is defined by the set of (θ_1, ϕ_1), and the acceptor μ_2 is defined by the set of (θ_2, ϕ_2). The orientation of the unitary vector r between the two fluorophores is defined by the set of (Θ, Φ).

$$\mu_2(\theta_2, \phi_2, \eta, \rho) = \mathbf{M} \times \begin{bmatrix} \sin\theta_2 \cos\phi_2 \\ \sin\theta_2 \sin\phi_2 \\ \cos\phi_2 \end{bmatrix} \tag{A.2}$$

$$r(\Theta, \Phi, \eta, \rho) = \mathbf{M} \times \begin{bmatrix} \sin\Theta \cos\Phi \\ \sin\Theta \sin\Phi \\ \cos\Phi \end{bmatrix} \tag{A.3}$$

where $\mathbf{M}$ is the transfer matrix from the cone frame (x, y, z) to the macroscopic one written as:

$$\mathbf{M} = \begin{bmatrix} \sin\eta\cos\rho & -\sin\rho & \cos\eta\cos\rho \\ \sin\eta\sin\rho & \cos\rho & \cos\eta\sin\rho \\ -\cos\eta & 0 & \sin\eta \end{bmatrix} \tag{A.4}$$

To account for the emission intensity from a pair of donor and acceptor dipole, we respectively take into account of the absorption probability of the donor and the detection probability of the emission light from the acceptor.

A.1.2 Absorption probability of the donor

The absorption probability of the donor is expressed as:

$$P_{abs} \propto |\vec{\mu}_1(\theta_1, \phi_1, \eta, \rho) \cdot \vec{E}|^2 \tag{A.5}$$

A.1.3 Detection probability of the acceptor

The detection probability of the emitting fluorescence from the acceptor is characterized by $J_{X,Y}(\theta_2, \phi_2, \eta, \rho)$ in both X and Y polarization direction, which is expressed as following:

$$J_X(\theta_2, \phi_2, \eta, \rho) = K_1\mu_{2X}^2(\theta_2, \phi_2, \eta, \rho) + K_2\mu_{2Y}^2(\theta_2, \phi_2, \eta, \rho) + K_3\mu_{2Z}^2(\theta_2, \phi_2, \eta, \rho) \tag{A.6}$$

$$J_Y(\theta_2, \phi_2, \eta, \rho) = K_2\mu_{2X}^2(\theta_2, \phi_2, \eta, \rho) + K_1\mu_{2Y}^2(\theta_2, \phi_2, \eta, \rho) + K_3\mu_{2Z}^2(\theta_2, \phi_2, \eta, \rho) \tag{A.7}$$

where μ_{2X} ,μ_{2Y} and μ_{2Z} are the three orthogonal components of the acceptor in the macroscopic frame. K_1, K_2 and K_3 are constants introduced to quantify the polarization coupling at the collection [5]. These coefficients are dependent on the numerical aperture of the objective, and expressed as [5]:

$$\begin{aligned} K_1 &= (-3\pi\cos{\sigma_0}^3 - 3\pi\cos{\sigma_0}^2 - 9\pi\cos\sigma_0 + 15\pi)/12 && \text{(A.8)} \\ K_2 &= (-\pi\cos{\sigma_0}^3 + 3\pi\cos{\sigma_0}^2 - 3\pi\cos\sigma_0 + \pi)/12 && \text{(A.9)} \\ K_3 &= (4\pi\cos{\sigma_0}^3 - 12\pi\cos\sigma_0 + 8\pi)/12 && \text{(A.10)} \end{aligned}$$

where σ_0 is the maximum half angle subtended by the objective, and can be calculated from its known numerical aperture (N.A.).

$$\text{N.A.} = n\sin\sigma_0$$

where n is the immersion refractive index. For N.A.=1.2 and a water immersion objective, $K_1 = 2.7020$, $K_2 = 0.0482$ and $K_3 = 0.8237$.

A.1.4 Coupling factor

The transfer rate angular dependence is characterized by a factor κ^2, and expressed as [26]:

$$\kappa^2 = [(\vec{\mu}_1 \cdot \vec{\mu}_2) - 3(\vec{\mu}_1 \cdot \vec{r})(\vec{\mu}_2 \cdot \vec{r})]^2 \tag{A.11}$$

Usually this factor is averaged angularly over the whole angle range for an isotropic orientation of dipoles: the averaged value equals to $\frac{2}{3}$, is often used as a simplification [26].

A.1.5 The emitted fluorescence

The emission fluorescence I_i^{FRET} contribution affected by the homo-FRET effect can be calculated by summing up the emission intensities from every pair of donor and acceptor dipoles within the cone, which can be accomplished by an integration over three domains of $\Omega_1 = (\theta_1, \phi_1)$, $\Omega_2 = (\theta_2, \phi_2)$ and $\Omega = (\Theta, \Phi)$, as presented as following:

$$I_i^{FRET}(\rho, \eta, \psi, \alpha) = \iiint |\mu_1 \cdot \vec{E}(\alpha)|^2 J_i(\theta_2, \phi_2, \eta, \rho)\kappa^2 f_1(\Omega_1) f_2(\Omega_2) g(\Omega) \mathrm{d}\Omega_1 \mathrm{d}\Omega_2 \mathrm{d}\Omega \tag{A.12}$$

with

$$\begin{aligned} \mathrm{d}\Omega_1 &= \sin\theta_1 \mathrm{d}\theta_1 \mathrm{d}\phi_1 && \text{(A.13)} \\ \mathrm{d}\Omega_2 &= \sin\theta_2 \mathrm{d}\theta_2 \mathrm{d}\phi_2 && \text{(A.14)} \\ \mathrm{d}\Omega &= \sin\Theta \mathrm{d}\Theta \mathrm{d}\Phi && \text{(A.15)} \end{aligned}$$

where $f_1(\Omega_1)$ and $f_2(\Omega_2)$ define respectively the angular distribution of the donor and the acceptor within the cone, described by a rectangle function for simplifying computations. The width of the rectangle indicates the cone aperture ψ. The function $g(\Omega)$ is used to describe the angular distribution of the relative position r between donors and acceptors. It is assumed to be $\frac{1}{4\pi^2}$ (if normalized) when r is distributed in the whole volume, but it should be distributed in a plane or in an anti-cone for the case of a membrane. The influences of $g(\Omega)$ will be discussed in detail in Section A.2.2.

In the presence of homo-FRET, the total emission fluorescence from the cone is written as:

$$I_i^{total}(\rho, \eta, \psi, \alpha) = (1 - T)I_i(\rho, \eta, \psi, \alpha) + TI_i^{FRET}(\rho, \eta, \psi, \alpha) \tag{A.16}$$

where $I_i(\rho, \eta, \psi, \alpha)$ is the emission intensity without FRET (see Chapter 2), i indicates the polarization orientation X and Y in detection path. T quantifies the transfer efficiency which is determined mainly by the inter-distance between donor and acceptor dipoles, and therefore by the dye concentration.

A.2 Results

In order to obtain a good precision while keeping reasonable compute time, in the following calculations, θ_1 θ_2 and Θ were properly sampled with 10° per step, ϕ_1, ϕ_2 and Φ were all sampled with a step of 36°.

A.2.1 Cones distributed in the whole focal volume

Fig. A.2 shows the polarimetric responses for cones with the same cone orientation ρ ($\rho = 60°$) but different cone apertures ($\psi = 40°, 100°, 140°$), at transfer efficiencies $T = 0, 0.3, 0.5$. From this figure, it is easy to see that homo-FRET deforms the emission response on X and Y analysis directions, especially at large cone aperture ψ and high transfer efficiency T. The depolarization induced at high FRET efficiencies is illustrated by almost identical I_X and I_Y polarization responses (similar shape with different amplitudes). Although the emission responses on X and Y polarization directions are deformed by homo-FRET, the total polarimetric response $I_X + I_Y$ is immune to homo-FRET as illustrated by the identical response to that without homo-FRET. This is explained by the fact that $I_X + I_Y$ is only sensitive to the excitation probability and therefore probe the distribution of absorption dipoles, which is identical independently of the presence of Homo-FRET.

As presented above, the polarization response from a cone is depolarized by homo-FRET at high transfer efficiency T. We also investigated the limit case of $\psi = 180°$ and $T = 1$, which means that all the dipoles are homogeneously oriented and the emission light is completely dominated by FRET. Theoretically in this case, the emission responses in the X and Y analysis directions are both polarization independent indicated by a circle curve in the polar figure. Fig. A.3 presents the polarization responses for cones with $\psi = 180°$ and $\rho = (60°)$. The polarization response contributed by homo-FRET with

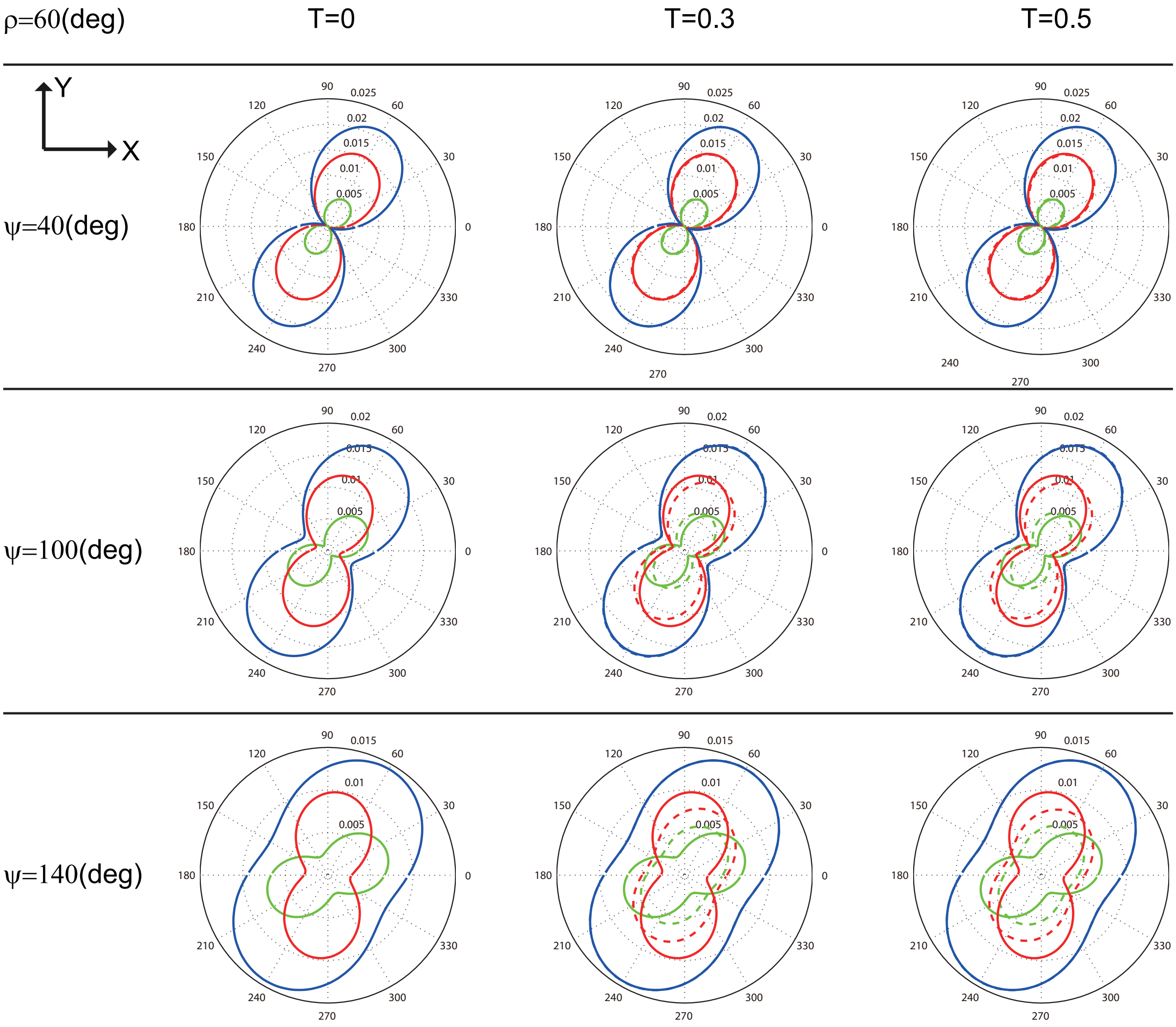

Figure A.2: The calculated polarization responses for cones ($\rho = 60°$, $\psi = 40°, 100°, 140°$) at different transfer efficiencies T. The red, green and blue solid lines respectively indicate the polarimetric responses I_X analyzed along X direction, I_Y analyzed along Y direction and the total response $I_X + I_Y$ without Homo-FRET. The dashed lines present the corresponding response with Homo-FRET.

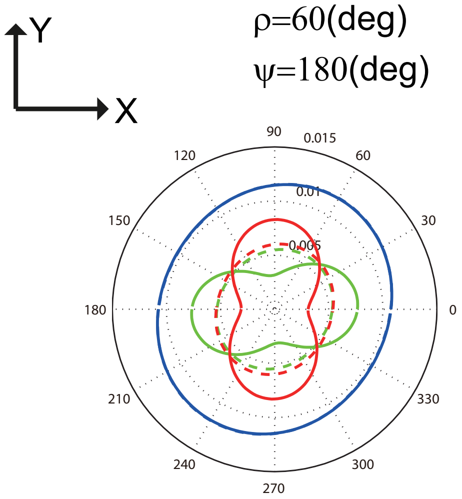

Figure A.3: The calculated fluorescence polarization responses for an isotropic sample ($\psi = 180°$), with assuming $\rho = 60°$ at transfer efficiencies $T = 1$. The red, green and blue solid lines respectively indicate the polarimetric responses I_X analyzed along X direction, I_Y analyzed along Y direction and the total response $I_X + I_Y$ without Homo-FRET. The dashed lines present the corresponding response with Homo-FRET.

$T = 1$ at X and Y polarization orientation are almost identical and circle shaped, and the differences between X and Y direction and a little ellipse shaped with orientation of ρ are caused by the sampling precision of in three microscopic-frames (Ω, Ω_1, Ω_2). Normally ρ is not defined for $\psi = 180°$ so the discussion is only about numerical errors.

A.2.2 Analysis for cones models distributed in membranes

In the calculations above, the vector $r(\Theta, \Phi)$ between the donor and the acceptor dipoles is oriented homogenously in all the directions. However for a very thin cell membrane composed of double lipids layer, as shown in Fig. A.4(a), the donor and acceptor dipoles are distributed on a surface with very small curvature inside the (X, Y) plane. So in the membrane case, the vector $r(\Theta, \Phi)$ is confined within an "anti-cone" like volume presented in Fig. A.4(b) with a "width" Ψ which depends on the membrane geometry (curvature, folds, etc.) inside the focal volume and a mean orientation representing the orientation of the membrane in the focal volume. This definitely affects the polarization response I_X and I_Y because the transfer rate κ^2 depends on the orientations of donor dipole, acceptor dipole and the vector r as presented in expression A.11.

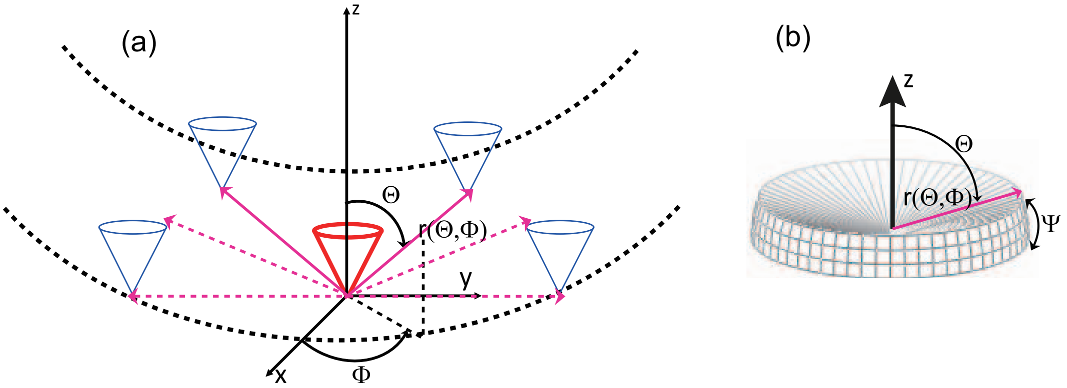

Figure A.4: (a) The relative position r for a couple of acceptor and donor in a cell membrane ((x, y, z) is the local microscope frame of the cell membrane). (b) Distribution in the membrane of the vector $r(\Theta, \Phi)$ between donor dipoles defined within the red cone and acceptor dipoles defined within the blue cones is like. The vector r is distributed within an "anti-cone" distribution of width Ψ.

In order to present the influences of the distribution of vector r in an anti-cone like volume, we investigated the dependence of transfer rate κ^2 on Θ which makes a distinction between whole volume and anti-cone like volume distributions. This factor also varies with the aperture of the cone of the donor and acceptor dipoles. Therefore for a given angle Θ distribution of r, the κ^2 is integrated over the local frames Ω_1 and Ω_2 of donor and acceptor dipoles inside the cone aperture ψ. Fig. A.5 presents dependencies of the integrated κ^2 for cones with different apertures on Θ ranging from 0° to 180° with $\Phi = 0°$. It is easy to see that the integrated transfer rate κ^2 gets the maximum value at $\Theta = 0°, 180°$ for cones with any aperture ψ, and its variation decreases with increasing cone aperture ψ until a complete independence on Θ at $\psi = 180°$, which is illustrated by a circle curve. This is expected since in this situation the dipoles take all orientations, therefore whatever the distribution of dipole, donors can find nearby an acceptor with a random orientation.

The influences of the distribution of r on the polarization responses is presented in Fig. A.6 where the polarization responses for a cone ($\rho = 60°$ and $\psi = 120°$) at $T = 1$ is compared between cases with different Θ distributions. Fig. A.6(a) presents the polarimetric response with Θ ranging from 0° to 180° which means r is orientated in all directions. Figs. A.6(b)(c)(d) respectively compare the polarization responses with Θ confined in different anti-cones with different width Ψ. We can see that only the responses with Θ confined in 0° to 20° differ a little (this is probably due to remaining

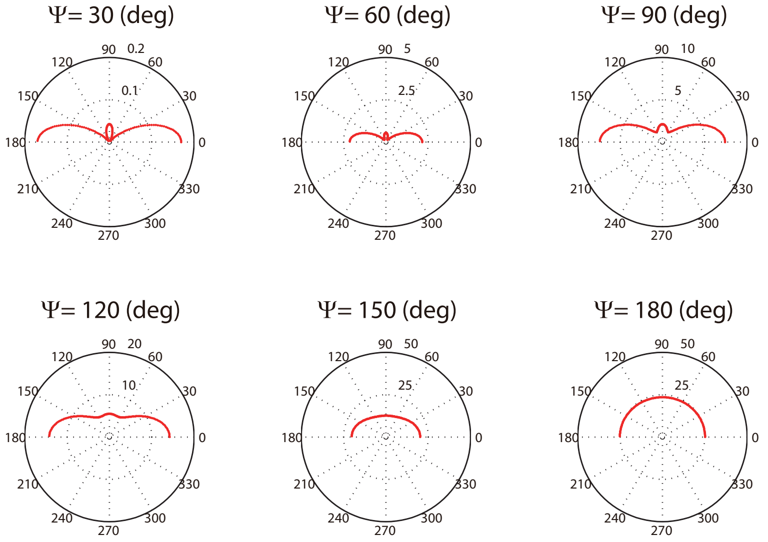

Figure A.5: The dependencies of integrated κ^2 on Θ (polar representation) for cones with different cone apertures ψ from 30° to 180° .

numerical sampling factors). The polarization responses for other membrane cases stay identical to the case of the whole volume distributed cones. This finally shows that the FRET depolarization effect is quite robust to the sample geometry, probably because κ^2 is essentially efficient for small of Θ values (Fig. A.5). We expect similar behavior for other values of T.

A.3 Brief analysis for FRET

The calculations above are made for homo-FRET which means that donors and acceptors are the same kind of dipoles distributed in a same cone. In this part we will describe the polarization responses influenced by FRET where the donor dipoles and acceptor dipoles are different and have different angular distributions. Fig. A.7 presents the polarization responses affected by FRET between donor dipoles distributed in cones (($\rho = 40°$, $\psi = 80°$) and ($\rho = 0°$, $\psi = 100°$)) and acceptor dipoles distributed in other type of cones ($\rho = 60°$, $\psi = 120°$) at different transfer efficiencies T. From this figure, we can conclude that the polarization responses I_X and I_Y are deformed and depolarized by FRET, but the total response $I_X + I_Y$ is immune to the FRET effect, similarly to homo-FRET. The total response is dependent only on the donor cone distribution but not on the acceptor distribution, which is expected.

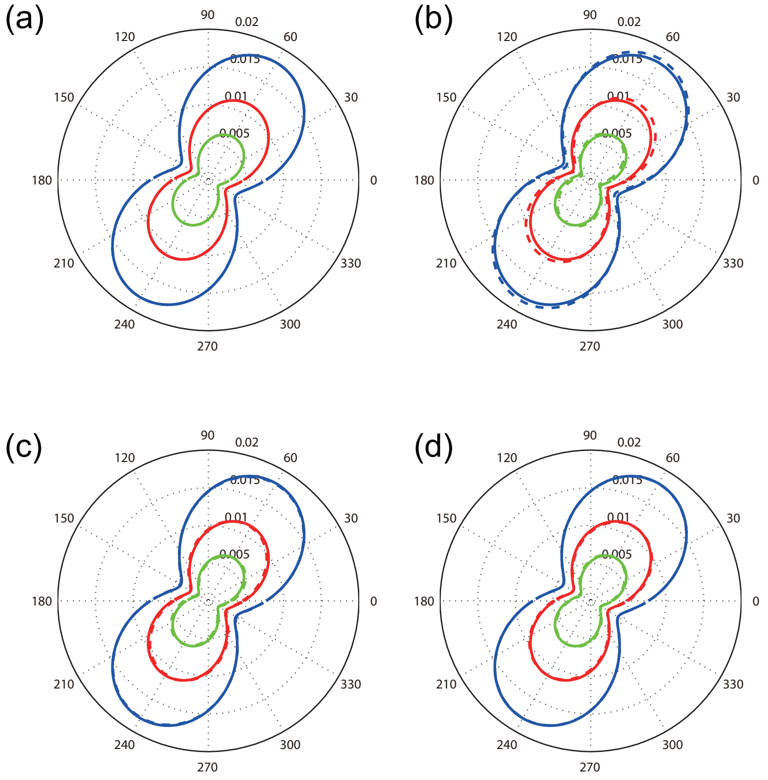

Figure A.6: The calculated polarimetric responses for cone ($\psi = 120°$, $\rho = 60°$) at transfer efficiencies $T = 1$ with Θ ranging (a) from 0° to 180° ($\Psi = 180°$), (b) 0° to 20° ($\Psi = 20°$, $\langle\Theta\rangle = 10°$), (c)30° to 50° ($\Psi = 20°$, $\langle\Theta\rangle = 40°$) and (d)70° to 90° ($\Psi = 20°$, $\langle\Theta\rangle = 80°$. The red, green and blue solid lines respectively indicate the polarization responses I_X, I_Y and total response $I_X + I_Y$ with Θ ranging from 0° to 180° . The dash lines present the corresponding response with Θ confined in an anti-cone.

Conclusion

In this part, we have analyzed the effect of Homo-FRET and FRET on the polarization resolved fluorescence signal that is measured. In agreement with the expected effect, we have confirmed that the total fluorescence intensity is not affected by energy transfer. More generally, these results show that, although Homo-FRET nose not affect linear dichroism, a polarization analysis of the emitted fluorescence provides a way to monitor it.

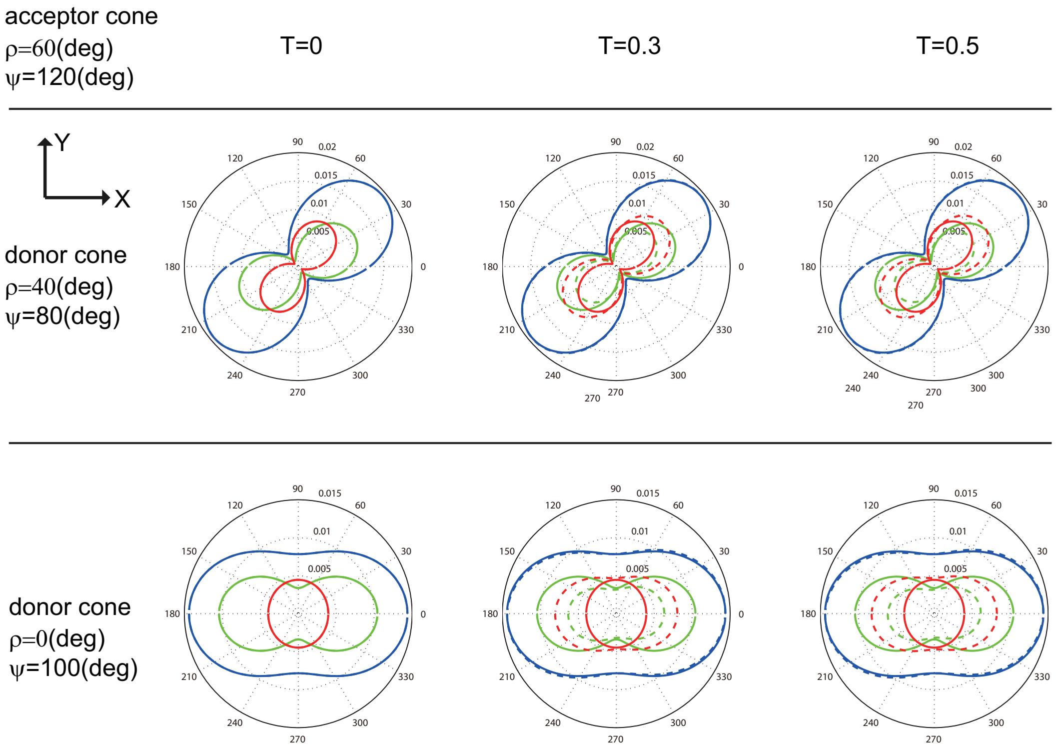

Figure A.7: Examples of calculated polarimetric response for FRET effect. One acceptor distribution and two different types of donor distributions with different transfer efficiencies T.

Appendix B

Measurement of a polarization state and analysis of polarization distortions

B.1 Measurement of a polarization state

B.1.1 Characterization of a polarization state

The polarization state is typically classified into linear, elliptic and circular polarization as presented in Fig. B.2(a). Actually linear and circular polarized light are special elliptic polarized light respectively with ellipticity of 0 and 1. Therefor, as shown in Fig. B.2(b), any arbitrary polarized light could be characterized by an elliptic polarized light with two parameters that are the orientation Θ of the long axis and the ellipticity $\tan\epsilon$.

B.1.2 The quarter waveplate method

To analyze systematically polarization states, a method called the quarter waveplate method is used based on analyzing the intensity of the light passing through a rotating quarter wave plate and a fixed polarizer [51], as schemed in Fig. B.2 (c). In the following, we employ the Jones formalism to detail the measurement of arbitrary polarization states.

Any polarized light with orientation Θ and ellipticity $\tan\epsilon$ could be written by the following Jones vector:

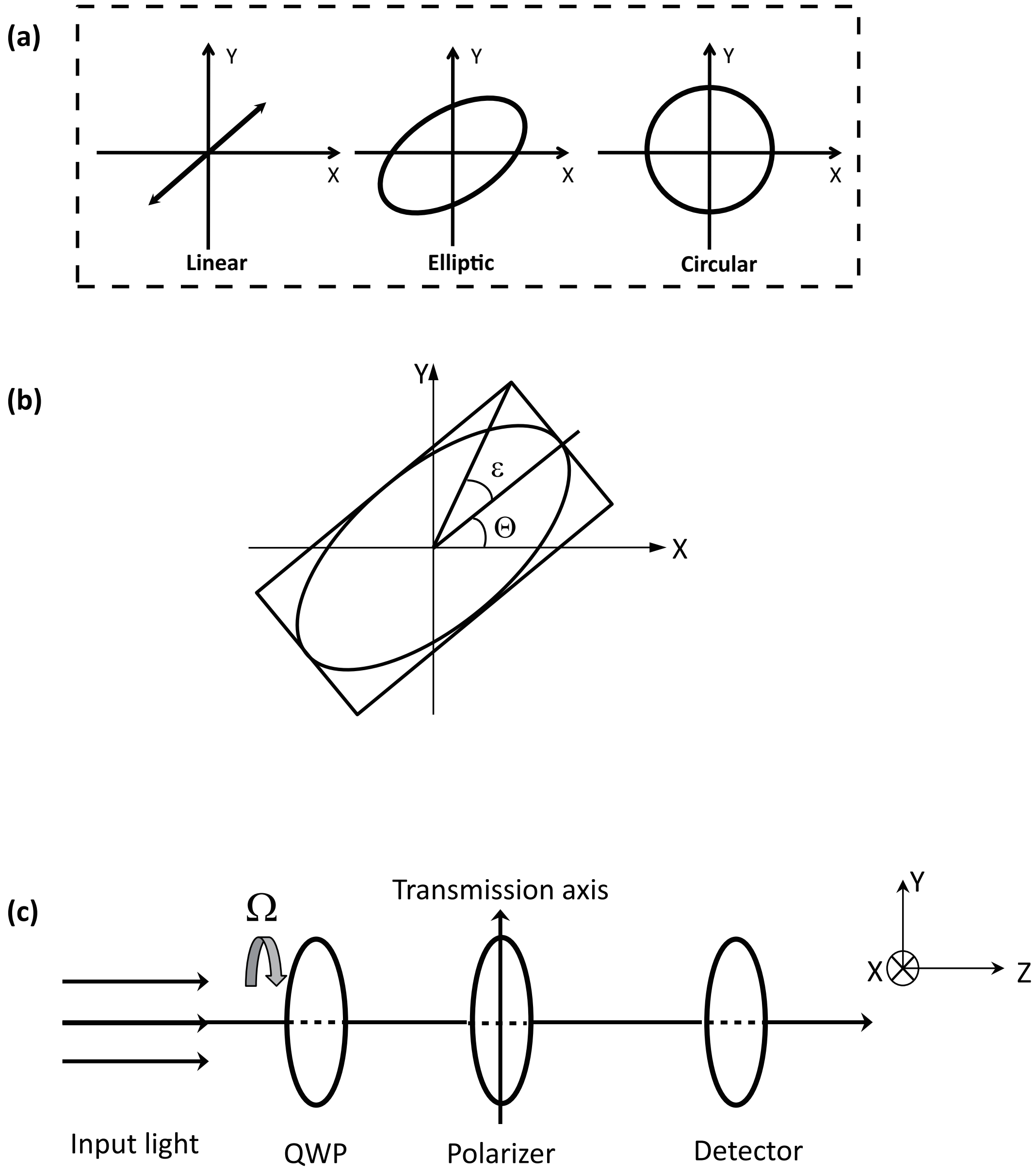

Figure B.1: (a) The typical polarization states: linear, elliptic and circular (b) Characterizing arbitrary polarization state with orientation Θ and ellipticity $\tan \epsilon$. (c) The setup to measure the polarization state of input light.

$$E_{input} = R(-\Theta) \times \begin{bmatrix} \cos\epsilon \\ i\sin\epsilon \end{bmatrix} = \begin{bmatrix} \cos\Theta & -\sin\Theta \\ \sin\Theta & \cos\Theta \end{bmatrix} \times \begin{bmatrix} \cos\epsilon \\ i\sin\epsilon \end{bmatrix} \tag{B.1}$$

$$= \begin{bmatrix} \cos\Theta\cos\epsilon - i\sin\Theta\sin\epsilon \\ \sin\Theta\cos\epsilon + i\cos\Theta\sin\epsilon \end{bmatrix} \tag{B.2}$$

where the $R(\Theta)$ is a rotation by an angle of Θ in the polarization plane (X, Y).

For a quarter wave plate with fast axis rotated by an angle of Ω respect to the X direction, the Jones matrix can be written as:

$$\begin{aligned} M_{QWP} &= R(-\Omega) \times \begin{bmatrix} 1 & 0 \\ 0 & i \end{bmatrix} \times R(\Omega) \\ &= \begin{bmatrix} \cos\Omega & -\sin\Omega \\ \sin\Omega & \cos\Omega \end{bmatrix} \times \begin{bmatrix} 1 & 0 \\ 0 & i \end{bmatrix} \times \begin{bmatrix} \cos\Omega & \sin\Omega \\ -\sin\Omega & \cos\Omega \end{bmatrix} \\ &= \begin{bmatrix} \cos^2\Omega + i\sin^2\Omega & (1-i)\cos\Omega\sin\Omega \\ (1-i)\cos\Omega\sin\Omega & i\cos^2\Omega + \sin^2\Omega \end{bmatrix} \end{aligned}$$

For a polarizer with transmission axis along Y direction, the Jones matrix can be written as:

$$M_{polarizer} = \begin{bmatrix} 0 & 0 \\ 0 & 1 \end{bmatrix}$$

So, the final field in the "quarter waveplate method" configuration is

$$\begin{aligned} E(\Omega) &= M_{polarizer} \times M_{QWP} \times E_{input} \\ &= \begin{bmatrix} 0 & 0 \\ 0 & 1 \end{bmatrix} \times \begin{bmatrix} \cos^2\Omega + i\sin^2\Omega & (1-i)\cos\Omega\sin\Omega \\ (1-i)\cos\Omega\sin\Omega & i\cos^2\Omega + \sin^2\Omega \end{bmatrix} \times \begin{bmatrix} \cos\Theta\cos\epsilon - i\sin\Theta\sin\epsilon \\ \sin\Theta\cos\epsilon + i\cos\Theta\sin\epsilon \end{bmatrix} \end{aligned}$$

After simplifying, the field can be written as:

$$E(\Omega) = \begin{bmatrix} 0 \\ \cos(\Omega-\Theta)\sin(\Omega-\epsilon) - i\sin(\Omega-\Theta)\cos(\Omega+\epsilon) \end{bmatrix}$$

The intensity $I(\Omega)$ measured by the detector is written as:

$$I(\Omega) = |E(\Omega)|^2 \tag{B.3}$$

$$\begin{aligned} I(\Omega) \;=\; & I_0 \left[\frac{1}{2} - \frac{1}{4}\cos 2\epsilon\, \cos 2\Theta - \frac{1}{2}\sin 2\epsilon\, \sin 2\Omega - \frac{1}{4}\cos 2\epsilon\, \cos 2\Theta \cos 4\Omega \right. \\ & \left. - \frac{1}{4}\cos 2\epsilon\, \sin 2\Theta \sin 4\Omega \right] \end{aligned} \tag{B.4}$$

The analysis of this intensity dependence as a function of Ω allows the retrieval of the unknown parameters ϵ and Θ.

B.1.3 Parameters retrieval

Equation B.4 can be written as a truncated Fourier series

$$I(\Omega) = \sum_{k=0}^{+\infty} \left[p_k \cos k\Omega + q_k \sin k\Omega \right],$$

the only non-zero coefficients being

$$\begin{aligned} p_0 &= \frac{I_0}{2} - \frac{I_0}{4}\cos 2\epsilon\, \cos 2\Theta = \frac{I_0}{2} + q_4, \\ q_2 &= -\frac{I_0}{2}\sin 2\epsilon, \\ p_4 &= -\frac{I_0}{4}\cos 2\epsilon\, \cos 2\Theta, \\ q_4 &= -\frac{I_0}{4}\cos 2\epsilon\, \sin 2\Theta. \end{aligned}$$

These coefficients can be easily extracted from the experimental values $I(\Omega)$ using basic Fourier algebra

$$\begin{aligned} p_k &= \frac{2}{N}\sum_{p=1}^{N} I(\Omega_p)\cos k\Omega_p \\ q_k &= \frac{2}{N}\sum_{p=1}^{N} I(\Omega_p)\sin k\Omega_p \end{aligned}$$

for $k = 2, 4$ and $p_0 = \frac{1}{N}\sum_{p=1}^{N} I(\Omega_p)$, where N is the number of measured angles. Then, one can show that

$$\Theta = \frac{1}{2}\arctan\left(\frac{q_4}{p_4}\right) + n\pi/2,$$

where n is an integer. Because $-\frac{\pi}{2} \leq \epsilon \leq \frac{\pi}{2}$, $\cos 2\epsilon \geq 0$, n is chosen so that both $\cos 2\Theta$ with p_4, and $\sin 2\Theta$ with p_4 are opposite in sign. Finally, ϵ is given by

$$\epsilon = \frac{1}{2} \arctan \left(\frac{q_2 \sin 2\Theta}{2q_4} \right).$$

B.2 Analysis of polarization distortions induced by an optical path

Optical component are known to distort polarization states. A way to remove the influences of the distortion is to model them, so that the distortion can be easily taken into consideration in the data processing. Here we propose that the polarization distortion are modeled equivalently by introducing virtual distorting optical elements characterized by their orientation, diattenuation and retardance. The angle θ is the orientation of the fast axis of one optical elements with respect to the horizontal axis X. The diattenuation $(1-\gamma)$ is the amplitude factor of the field along its slow axis. The retardance δ is the phase shift of the field introduced along its slow axis.

In simple cases one virtual distorting element could perfectly model the global distortion, however in complex cases one virtual distortion elements is not sufficient since the polarization is sequentially distorted by several optical elements with optical axes oriented differently.

To obtain the number and the parameters of the virtual distorting elements, we used a fitting method. Using the polarization diagnostic tool presented above, the polarization state of light (characterized by orientation Θ and ellipticity $\tan\epsilon$) was measured for different incident linearly polarized light with polarization angles α between 0° and 180°. By fitting the output polarization state responses (simultaneously Θ and $\tan\epsilon$) to the input polarization angle α, we can find the appropriate group of virtual distorting elements which has the equivalent distorting effects. The solution is not unique, but all the solutions can model the distortion induced by the optical path. Fig. B.2 presents an example of modeling the polarization distortion in the excitation path of the confocal setup. Fig. B.2(b) shows the measured output polarization states for different input polarization angle α varying from 0° to 180° with step of 10°, which are plotted in Fig. B.2(c) with white dots (including orientation Θ and ellipticity $\tan\epsilon$). In Fig. B.2(a) the parameters of virtual distorting elements were changed (up to 3 elements can be added) to make its corresponding output of the polarization state (red curve) match the measured results

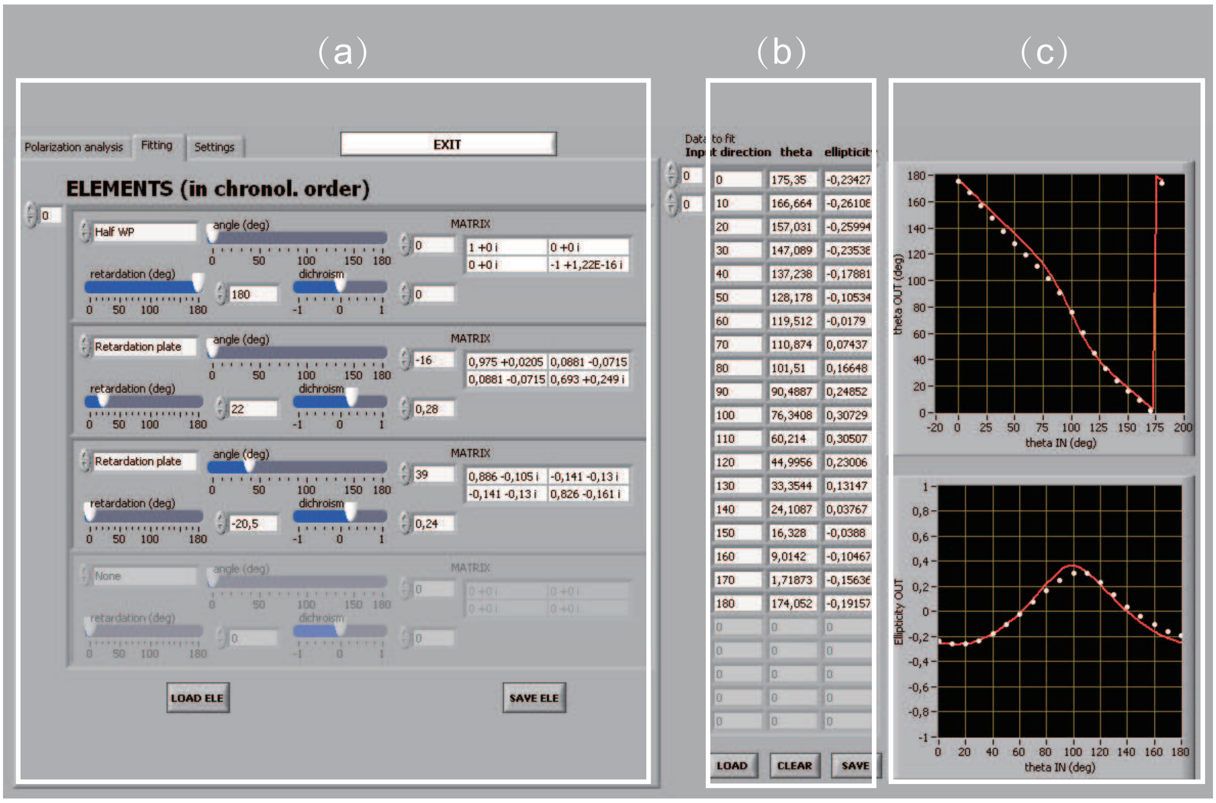

ELEMENTS (in chronol. order)

0

Half WP
angle (deg): 0
retardation (deg): 180
dichroism: 0

MATRIX

1 +0 i	0 +0 i
0 +0 i	-1 +1,22E-16 i

Retardation plate
angle (deg): -16
retardation (deg): 22
dichroism: 0,28

MATRIX

0,975 +0,0205	0,0881 -0,0715
0,0881 -0,0715	0,693 +0,249 i

Retardation plate
angle (deg): 39
retardation (deg): -20,5
dichroism: 0,24

MATRIX

0,886 -0,105 i	-0,141 -0,13 i
-0,141 -0,13 i	0,826 -0,161 i

None
angle (deg): 0
retardation (deg): 0
dichroism: 0

MATRIX

0 +0 i	0 +0 i
0 +0 i	0 +0 i

Dat to fit

0
0

Inp t direction	theta	ellipticit
0	175,35	-0,23427
10	166,664	-0,26108
20	157,031	-0,25994
30	147,089	-0,23538
40	137,238	-0,17881
50	128,178	-0,10534
60	119,512	-0,0179
70	110,874	0,07437
80	101,51	0,16648
90	90,4887	0,24852
100	76,3408	0,30729
110	60,214	0,30507
120	44,9956	0,23006
130	33,3544	0,13147
140	24,1087	0,03767
150	16,328	-0,0388
160	9,0142	-0,10467
170	1,71873	-0,15636
180	174,052	-0,19157
0	0	0
0	0	0
0	0	0
0	0	0
0	0	0

Figure B.2: Screenshot of the diagnostic tool developed to quantify polarization distortion. (a) The used virtual distorting elements and their parameters. (b) The measured output polarization states after passing the excitation path for different incident linearly polarized light. (c) The fitting results.

both in orientations Θ and ellipticity tan ϵ (white dots).

Appendix C

Preparation of samples

C.1 Preparation of Giant Unilamellar Vesicles (GUVs)

The giant unilamellar vesicles (GUVs) were prepared according to the electroformation method developed by Angelova and Dimitrov [37]. First, 2 μL of 0.5 mM dye(DiIC$_{18}$, ANEPPQ) solution was mixed with 98 μL of 1 mM DOPC (1,2-dioleoyl-sn-glycero-3-phosphocholine) solution which is prepared by dissolving the DOPC powder in mixture solution of chloroform and methanol(9 :1). Then the mixture solution of DOPC and dye is deposited on two glass slides covered with indium tin oxide. The chloroform elimination was completed by drying the slides under vacuum with room temperature for at least 2 hours. the two slides were then sealed together to make a chamber with the thickness of 5mm and solvent (240mM solution of sucrose in water) was added to the chamber. A 10 Hz, 25 mV peak to peak sinusoidal voltage was applied with increasing by 100mv every 5 minutes up to 1225 mV, which was maintained overnight. At the end, a 10 Hz, 1.2 V of square wave is applied for 30 minutes to detach the GUVs from the slides. Finally the GUVs solution was mixed with 280 mM glucose solution in water. With this approach, we have obtained GUVs with diameter ranging from 10 to 80 μm.

C.2 Preparation of cells

COS-7 cells (ATCC No. CRL-1657; American Type Culture Collection, Manassas, VA). COS-7 cells were grown in an incubator at 37°C in Lab-Tek chambers (Nunc, Rochester, NY) in DMEM medium (Gibco , Saint Aubin, France) completed by 10% FBS and 1%

sodium pyruvate. Cells were washed and kept in Hanks buffered salt solution containing 10 mM HEPES (HBSS/HEPES), pH 7.4, at 37°C, for the whole imaging process. Cells were labeled with DiIC18 directly before measurements and after the pharmacological treatments. For labelling, cells were washed and incubated in HBSS/HEPES with 1 μM DiIC18 (dissolved by absolute ethanol to 1 mM for preservation and usage) for 2 min at room temperature. After incubation, cells were washed again and kept in HBSS/HEPES at 37°C for the whole imaging process. The dyes' concentration used did not affect the cell shape over the whole duration of the measurements. For the pharmacological treatments altering cytoskeleton fibers, cells were washed in HBSS/HEPES and incubated at 37°C with 1 μM latrunculin A (5 min), 10 μM cytochalasin D (30 min) or 0.5 μM jasplakinolide (5 min). Cells were then washed with HBSS/HEPES and labeled and kept in HBSS/HEPES with 10 times diluted reagent during the whole imaging process.

Bibliography

[1] D. A. Cheresh, J. Leng, and R. L. Klemke. Regulation of cell contraction and membrane ruffling by distinct signals in migratory cells. *J. Cell Biol.*, 146(5):1107–1116, 1999.

[2] A. Anantharam, B. Onoa, R. H. Edwards, R. W. Holz, and D. Axelrod. Localized topological changes of the plasma membrane upon exocytosis visualized by polarized tirfm. *J. Cell Biol.*, 188(3):415–428, 2012.

[3] D. R. Fooksman, G. K. Gronvall, Q. Tang, and M. Edidin. Clustering class i mhc modulates sensitivity of t cell recognition. *J. Immunol*, 176(11):6673–6680, 2006.

[4] B. Valeur. *Molecular Fluorescence: Principles and Applications*. Wiley-VCH, 2001.

[5] D. Axelrod. Carbocyanine dye orientation in red-cell membrane studied by microscopic fluorescence polarization. *Biophys. J.*, 26(3):557–573, 1979.

[6] A. M. Vrabioiu and T. J. Mitchison. Structural insights into yeast septin organization from polarized fluorescence microscopy. *Nature*, 443(7110):466–469, 2006.

[7] R. K. P. Benninger, B. Onfelt, M. A. A. Neil, D. M. Davis, and P. M. W. French. Fluorescence imaging of two-photon linear dichroism: Cholesterol depletion disrupts molecular orientation in cell membranes. *Biophys. J.*, 88(1):609–622, 2005.

[8] G. Steinbach, I. Pomozi, O. Zsiros, L. Menczel, and G. Garab. Imaging anisotropy using differential polarization laser scanning confocal microscopy. *Acta. Histochem*, 111(4):317–326, 2009.

[9] G. Steinbach, I. Pomozi, D. P. Jánosa, J. Makovitzky, and G. Garab. Confocal fluorescence detected linear dichroism imaging of isolated human amyloid fibrils. role of supercoiling. *Biophys. J.*, 66(5):1319–1327, 1994.

[10] J. Borejdo and S. Burlacu. Orientation of actin filaments during motion in in vitro motility assay. *Biophys. J.*, 66(5):1319–1327, 1994.

[11] A. Gasecka, T. J. Han, C. Favard, B. R. Cho, and S. Brasselet. Quantitative imaging of molecular order in lipid membranes using two-photon fluorescence polarimetry. *Biophys. J.*, 97(10):2854–2862, 2009.

[12] A. Kress, P. Ferrand, H. Rigneault, T. Trombik, H. T. He, D. Marguet, and S. Brasselett. Probing orientational behavior of mhc class i protein and lipid probes in cell membranes by fluorescence polarization-resolved imaging. *Biophys. J.*, 101(2):468–476, 2011.

[13] A. Kress, X. Wang, H. Ranchon, J. Savatier, H. Rigneault, P. Ferrand, and S. Brasselet. Mapping the local organization of cell membranes using excitation polarization resolved confocal fluorescence microscopy. *Biophys. J.*, 105(1):127–138, 2013.

[14] J. F. W. Herschel. On a case of superficial colour prsented by a homogeneous liquid inernally colourless. *Philos. Trans. R. Soc. London*, 135:143, 1845.

[15] G. G. Stokes. On the change of rafrangibility of light. *Philos. Trans. R. Soc. London*, page 463, 1852.

[16] A. Gasecka. *Polarimetric multiphoton fluorescence microscopy in molecular and biological media.* PhD thesis, University Paul Cezanne, 2010.

[17] J. W. Lichtman and J. A. Conchello. Fluorescence microscopy. *Nat. Methods*, 2(12):910–919, 2005.

[18] A. Jablonske. Uber den mechanismus der photolumineszenz von farbstoffphosphoren. *Z. Phys.*, 94:38, 1935.

[19] J. R. Lakowicz. *Principles of Fluorescence Spectroscopy.* Kluwer Academic / Plenum Publishers, 1999.

[20] J. Franck and E. G. Dymond. Elementary processes of photochemical reactions. *Trans. Faraday Soc.*, 21:536, 1926.

[21] E. Condon. A theory of intensity distribution in band systems. *Phys. Rev.*, 28:1182, 1926.

[22] R. W. Boyd. *Principles of Fluorescence Spectroscopy.* Academic press, 2003.

[23] S. Bidault. *Manipulation optique de l'organisation de chromophores non-lineaires et luminescents.* PhD thesis, École normale supérieure de Cachan, 2004.

[24] G. Weber. Rotational brownian motion and polarization of the fluorescence of solutions. *Adv. Protein Chem.*, 8:415–459, 1953.

[25] C. Cantor and P. Schimmel. *Biophysical Chemistry.* W. H. Freeman and Company, 1980.

[26] T. Förster. Zwischenmolekulare energiewanderung und fluoreszenz. *Ann. Physik*, 437:55–75, 1948.

[27] K. Florinecasteel. Phospholipid order in gel-phase and fluid-phase cell-size liposomes measured by digitized video fluorescence polarization microscopy. *Biophys. J.*, 57(6):1199–1215, 1990.

[28] J. V. Rocheleau, M. Edidin, and D. W. Piston. Intrasequence gfp in class i mhc molecules, a rigid probe for fluorescence anisotropy measurements of the membrane environment. *Biophys. J.*, 84(6):4078–4086, 2003.

[29] J. E. Reeve, A. D. Corbett, I. Boczarow, T. Wilson, H. Bayley, and H. L. Anderson. Probing the orientational distribution of dyes in membranes through multiphoton microscopy. *Biophys. J.*, 103(5):907–917, 2012.

[30] J. Lazar, A. Bondar, S. Timr, and S. J. Firestein. Two-photon polarization microscopy reveals protein structure and function. *Nat. Methods*, 8(8):684–690, 2011.

[31] J. Borejdo and S. Burlacu. Measuring orientation of actin-filaments within a cell-orientation of actin in intestinal microvilli. *Biophys. J.*, 65(1):300–309, 1993.

[32] B. S. DeMay, N. Noda, A. S. Gladfelter, and R. Oldenbourg. Rapid and quantitative imaging of excitation polarized fluorescence reveals ordered septin dynamics in live yeast. *Biophys. J.*, 101(4):985–994, 2011.

[33] B. S. DeMay, X. Bai, L. Howard, P. Occhipinti, R. A. Meseroll, E. T. Spiliotis, R. Oldenbourg, and A. S. Gladfelter. Septin filaments exhibit a dynamic, paired organization that is conserved from yeast to mammals. *J. Cell Biol.*, 193(6):1065–1081, 2011.

[34] J. F. Lesoine, J. Y. Lee, J. R. Krogmeier, H. Kang, M. L. Clarke, R. Chang, D. L. Sackett, R. Nossal, and J. Hwang. Quantitative scheme for full-field polarization rotating fluorescence microscopy using a liquid crystal variable retarder. *Rev. Sci. Instrum.*, 83(5), 2012.

[35] S. Brasselet. Polarization-resolved nonlinear microscopy: application to structural molecular and biological imaging. *Advances in Optics and Photonics*, 3:205–271, 2011.

[36] J. R. Taylor. *An introduction to error analysis: the study of uncertainties in physical measurements*. University Science Books, 2nd edition, 1996.

[37] M. I. Angelova and D. S. Dimitrov. Liposome electroformation. *Faraday Discuss.*, 81:303+, 1986.

[38] K. Florinecasteel. Phospholipid order in gel-phase and fluid-phase cell-size liposomes measured by digitized video fluorescence polarization microscopy. *Biophys. J.*, 57(6):1199–1215, 1990.

[39] M. Minsky. Memoir on inventing the confocal scanning microscope. *Scanning*, 10(4):128–138, 1988.

[40] H. Hirukawa, H. Nakayama, Y. Tanibata, and Y. Kuwabara. *New techonologies for cus-x1 confocal scanner unit*, english edition, 2008.

[41] E. Wang, C. M. Babbey, and K. W. Dunn. Performance comparison between the high-speed yokogawa spinning disc confocal system and single-point scanning confocal systems. *Journal of Microscopy*, 218:148–159, 2005.

[42] M. Bohmer and J. Enderlein. Orientation imaging of single molecules by wide-field epifluorescence microscopy. *J. Opt. Soc. Am. B: Opt. Phys.*, 20(3):554–559, 2003.

[43] N. Sandeau, L. Le Xuan, D. Chauvat, C. Zhou, J.F. Roch, and S. Brasselet. Defocused imaging of second harmonic generation from a single nanocrystal. *Opt. Exp.*, 15(24):16051–16060, 2007.

[44] J. T. Fourkas. Rapid determination of the three-dimensional orientation of single molecules. *Opt. Lett.*, 26(4):211–213, 2001.

[45] M. R. Foreman, C. M. Romero, and P. Torok. Determination of the three-dimensional orientation of single molecules. *Opt. Lett.*, 33(9):1020–1022, 2008.

[46] J. Hohlbein and C. G. Huebner. Three-dimensional orientation determination of the emission dipoles of single molecules: The shot-noise limit. *J. Chem. Phys.*, 129(9), 2008.

[47] J. Hohlbein and C. G. Hubner. Simple scheme for rapid three-dimensional orientation determination of the emission dipole of single molecules. *Appl. Phys. Lett.*, 86(12), 2005.

[48] L. Novotny and B. Hecht. *Principles of Nano-Optics.* Cambridge University Press, 2011.

[49] J. Duboisset, P. Ferrand, W. He, X. Wang, H. Rigneault, and S. Brasselet. Thioflavine-t and congo red reveal the polymorphism of insulin amyloid fibrils when probed by polarization-resolved fluorescence microscopy. *J. Phys. Chem. B*, 117(3):784–788, 2013.

[50] G. Bautista, M. J. Huttunen, J. Makitalo, J. M. Kontio, J. Simonen, and M. Kauranen. Second-harmonic generation imaging of metal nano-objects with cylindrical vector beams. *Nano Lett.*, 12(6):3207–3212, 2012.

[51] E. Collett. *Polarized light: fundamentals and applications.* Marcel Dekker, 1993.